LAA/ LANGLEY

IN-39 P. 179

NAG1-215

CENTER FOR COMPUTER AIDED DESIGN

R-1566 CR

82563

College of Engineering
The University of Iowa
Iowa City, Iowa 52242

(NASA-CR-181099) SHAPE DESIGN SENSITIVITY ANALYSIS AND OPTIMIZATION OF THREE DIMENSIONAL ELASTIC SOLIDS USING GEOMETRIC MODELING AND AUTOMATIC REGRIDDING Ph.D. Thesis (Iowa Univ.) 179 p Avail: NTIS HC G3/39 N87-26371 Unclas 0082563

Technical Report 87-1

SHAPE DESIGN SENSITIVITY ANALYSIS AND OPTIMIZATION OF THREE DIMENSIONAL ELASTIC SOLIDS USING GEOMETRIC MODELING AND AUTOMATIC REGRIDDING

by

Tse-Min Yao and Kyung K. Choi

Center for Computer Aided Design

College of Engineering
The University of Iowa
Iowa City, Iowa 52242

Research supported by National Aeronautics
and Space Administration Grant number NAG-1-215
and National Science Foundation Grant number MSM-83-19871.
Contents of this report served as the thesis in partial
fulfillment of the requirements for the Ph.D. degree
in Mechanical Engineering, The University of Iowa.

January 1987

ABSTRACT

An automatic regridding method and a three dimensional shape design parameterization technique are constructed and integrated into a unified theory of shape design sensitivity analysis. An algorithm is developed for general shape design sensitivity analysis of three dimensional elastic solids. Numerical implementation of this shape design sensitivity analysis method is carried out using the finite element code ANSYS.

The unified theory of shape design sensitivity analysis uses the material derivative of continuum mechanics with a design velocity field that represents shape change effects over the structural domain. To satisfy the requirement that the design velocity field be at least as regular as the displacement field, displacement shape functions are used to represent the design velocity field. This procedure provides an isoparametric mapping. Automatic regridding methods are developed by generating a domain velocity field with the boundary displacement method. The boundary displacement method treats a perturbation of shape as an external load to obtain the corresponding interior movements through use of the governing structural equations. Automatic regridding obtained in this manner preserves grid orthogonality and consequently the accuracy of analysis and shape design sensitivity analysis. Shape

design sensitivity of pointwise stress is obtained from domain averaged stress sensitivity, by taking a limit. The boundary layer method, coupled with the boundary displacement method, is shown to be an efficient procedure for shape design sensitivity analysis.

Shape design parameterization for three dimensional surface design problems is illustrated using a Bezier surface with boundary perturbations that depend linearly on the perturbation of design parameters. A linearization method of optimization, LINRM, is used to obtain optimum shapes. Three examples from different engineering disciplines are investigated to demonstrate the accuracy and versatility of this shape design sensitivity analysis method. An engine bearing cap and a doubly-curvatured arch dam are analyzed and optimized. A total hip joint reconstruction is studied for shape design sensitivity analysis.

TABLE OF CONTENTS

Page

LIST OF TABLES.....vi

LIST OF FIGURES.....viii

LIST OF SYMBOLS.....xi

CHAPTER

1 INTRODUCTION.....1
1.1 Introductory Comments and Literature Review.....1
1.2 Objectives and Scope.....5

2 DOMAIN METHOD OF SHAPE DESIGN SENSITIVITY ANALYSIS.....8
2.1 Three Dimensional Linear Elasticity.....9
2.2 Shape Design Sensitivity Analysis.....12
2.2.1 Design Velocity Field.....12
2.2.2 Material Derivative of General Functional.....14
2.2.3 Material Derivative of Displacement.....18
2.2.4 Material Derivative of General Stress Functional.....21
2.2.5 Material Derivative of Pointwise Stress Functional.....24

3 DESIGN PARAMETRIZATION.....28
3.1 Boundary Shape Design Parametrization and Boundary Velocity.....30
3.2 Bezier Curves and Surfaces.....33
3.2.1 Bezier Curves.....33
3.2.2 Bezier Surfaces.....42
3.2.3 Design Parametrization with Bezier Curves and Surfaces.....45

4 AUTOMATIC REGRIDDING AND DESIGN VELOCITY FIELD.....47
4.1 Computation of Design Velocity Field and Automatic Regridding.....48
4.1.1 Mesh Generation Method.....49
4.1.2 Boundary Displacement Method.....50
4.2 Boundary Layer.....56
4.3 Computational Algorithm for Efficient Shape Design Sensitivity Analysis.....58
4.4 Shape Design Sensitivity Computational Algorithm.....60

Page

5 SHAPE DESIGN SENSITIVITY ANALYSIS.....63
5.1 Engine Bearing Cap.....64
5.1.1 Stress Design Sensitivity Analysis.....70
5.1.2 Results and Discussion.....70
5.2 Doubly-Curvatured Arch Dam.....72
5.2.1 Material Derivative of Load Linear Form of Body Force.....78
5.2.2 Material Derivative of Load Linear Form of Surface Traction.....80
5.2.3 Results and Discussion.....81
5.3 Total Hip Joint Reconstruction.....82
5.3.1 Shape Design Sensitivity Analysis.....88
5.3.2 Results and Discussion.....95

6 SHAPE DESIGN OPTIMIZATION.....126
6.1 Engine Bearing Cap.....126
6.1.1 Optimization Procedure.....129
6.1.2 Results and Discussion.....131
6.2 Doubly-Curvatured Arch Dam.....142
6.2.1 Optimization Procedure.....144
6.2.2 Results and Discussion.....147

7 CONCLUSIONS.....156

REFERENCES.....158

LIST OF TABLES

Table		Page
5.1	SDSA result of cap ($\delta b_1 = 0.01\ b_1$)	97
5.2	SDSA result of cap ($\delta b_2 = 0.01\ b_2$)	98
5.3	SDSA result of cap ($\delta b_3 = 0.01\ b_3$)	99
5.4	SDSA result of cap ($\delta b_4 = 0.01\ b_4$)	100
5.5	SDSA result of cap ($\delta b_5 = 0.01\ b_5$)	101
5.6	SDSA result of cap ($\delta b_6 = 0.01\ b_6$)	102
5.7	Grading system for accuracy of SDSA results	103
5.8	Accuracy of cap SDSA results	103
5.9	SDSA result of dam ($\delta b_1 = 1$)	104
5.10	SDSA result of dam ($\delta b_6 = 1$)	105
5.11	SDSA result of dam ($\delta b_8 = 1$)	106
5.12	SDSA result of dam ($\delta b_{13} = 1$)	107
5.13	SDSA result of dam ($\delta b_{17} = 1$)	108
5.14	SDSA result of dam ($\delta b_{23} = 1$)	109
5.15	SDSA result of dam ($\delta b_{29} = 1$)	110
5.16	SDSA result of dam ($\delta b_{32} = 1$)	111
5.17	Accuracy of dam SDSA results	112
5.18	SDSA result of stem principal stress at stem-cement interface ($\delta b_1 = 0.05\ b_1$)	113
5.19	SDSA result of stem principal stress at stem-cement interface ($\delta b_5 = 0.05\ b_5$)	114

Table | Page

5.20 SDSA result of stem principal stress at stem-cement interface ($\delta b_8 = 0.05\ b_8$) 115

5.21 SDSA result of cement strain energy density at stem-cement interface ($\delta b_1 = 0.05\ b_1$) 116

5.22 SDSA result of cement strain energy density at stem-cement interface ($\delta b_5 = 0.05\ b_5$) 117

5.23 SDSA result of cement strain energy density at stem-cement interface ($\delta b_8 = 0.05\ b_8$) 118

5.24 SDSA result of cement strain energy density at bone-cement interface ($\delta b_9 = 0.05\ b_9$) 119

5.25 SDSA result of cement strain energy density at bone-cement interface ($\delta b_{13} = 0.05\ b_{13}$) 120

5.26 SDSA result of cement strain energy density at bone-cement interface ($\delta b_{16} = 0.05\ b_{16}$) 121

5.27 SDSA result of bone principal stress at bone-cement interface ($\delta b_9 = 0.05\ b_9$) 122

5.28 SDSA result of bone principal stress at bone-cement interface ($\delta b_{13} = 0.05\ b_{13}$) 123

5.29 SDSA result of bone principal stress at stem-cement interface ($\delta b_{16} = 0.05\ b_{16}$) 124

5.30 Accuracy of hip joint SDSA results.....125

6.1 Shape design parameters of cap design 1.....135

6.2 Optimization history of cap design 1.....135

6.3 Shape design parameters of cap design 2.....138

6.4 Optimization history of cap design 2.....138

6.5 Comparison of 8-node and 20-node models (Wassermann's optimal design).....143

6.6 Shape design parameters of arch dam.....143

6.7 Optimization history of arch dam.....150

LIST OF FIGURES

Figure		Page
2.1	Three dimensional elastic solid	11
2.2	Deformation process	11
3.1	Parametric representation of shape	32
3.2	Quadratic polynomial	32
3.3	Bernstein basis	35
3.4	Bezier curve	35
3.5	Bezier curve in the x_1-x_2 plane	37
3.6	Perturbation of a Bezier curve	37
3.7	Closed Bezier curve	40
3.8	Zero-order continuity of Bezier curve	40
3.9	First-order continuity of Bezier curve	40
3.10	4x4 Bezier surface	43
4.1	Mesh generation method for fillet	53
4.2	Boundary deformation method for fillet	53
4.3	Boundary deformation method with incremental deformations	54
4.4	A boundary layer	57
4.5	Fillet boundary layer	57
5.1	Engine bearing cap	65
5.2	20 node isoparametric solid finite element	66
5.3	Finite element model of engine bearing cap	68
5.4	Definition of cap design parameters	68

Figure Page

5.5 Boundary layer for design parameter 5.....69

5.6 Boundary layer for design parameter 6.....69

5.7 Doubly-curvatured arch dam.....73

5.8 Contour plan and crown cross section of an arch dam.....73

5.9 Parametric representation of a dam.....76

5.10 Finite element model of dam.....77

5.11 A profile of water pressure.....77

5.12 A profile of approximated water pressure.....77

5.13 Total hip joint reconstruction.....84

5.14 Finite element model of hip joint reconstruction.....90

5.15 Finite element model of stem.....91

5.16 Finite element model of cement.....92

5.17 Finite element model of bone.....93

5.18 Shape design parameters of hip joint.....94

6.1 Engine bearing cap finite element model.....127

6.2 Bearing cap pressure profile.....128

6.3 Shape design parameter of bearing cap.....128

6.4 Boundary layer for design parameter 4.....130

6.5 Boundary layer for design parameter 5.....130

6.6 Cap deformation due to bolt load only (initial design).....133

6.7 Cap deformation due to bolt load and oil film pressure (initial design).....133

6.8 Design shape of a local minimum.....134

6.9 Initial shape of modified cap.....136

6.10 An optimum shape of cap (symmetric design).....137

Figure Page

6.11 An optimum shape of cap (non-symmetric design).....141

6.12 Initial shape of arch dam.....145

6.13 Optimal shape of arch dam.....149

6.14 Optimum arch dam element layer 1.....151

6.15 Optimum arch dam element layer 2.....151

6.16 Optimum arch dam element layer 3.....152

6.17 Optimum arch dam element layer 4.....152

6.18 Optimum arch dam element layer 5.....153

6.19 Optimum arch dam element layer 6.....153

6.20 Arch dam optimization cost-constraint history.....154

LIST OF SYMBOLS

A	Differential operator
a	Energy bilinear form
$B_{n,N}$	Bernstein basis function
[BMTX]	Bezier matrix
b	Shape design parameters
C	Elastic modulus tensor
C^k	The collection of k-times continuously differentiable functions
C_n, C_{mn}	Control point
Div	Divergence operator
F	Body force function
$F(n,N)$	Binomial factorial
f, g, h	Function or functional
H	Curvature
$[H(\Omega)]$	Sobelev space
z	Displacement function
Γ	Boundary of an elastic solid
δ	Variation
$\hat{\delta}$	Dirac measure
δ_{ij}	Kronecker delta
ℓ	Load linear form
λ	Adjoint variable

ν	Poisson's ratio
σ	Stress tensor
ε	Strain tensor
ψ	Constraint functional
Ω	Domain of an elastic solid
∇	Gradient operator
m_p	Characteristic function
n	Outward normal vector
τ	Pseudo time parameter
$p(x)$	Pressure function
$P(v)$	Bezier curve
$P_n x_i$	x_i-coordinate of node P_n
S_n	Shape function
SDSA	Shape design sensitivity analysis
T	Traction vector
v	Normalized parameter
V	Design velocity field
$\hat{x}$	Isolated point
Z	Kinematically admissible displacement field
$\overline{Z}, \overline{\lambda}$	Virtual displacement
$(\dot{\ })$	Material derivative of ( )
$(\ )^T$	Transpose of ( )
$(\ )^{-1}$	Inverse of ( )
$\|\ \|$	Vector norm

CHAPTER 1

INTRODUCTION

1.1 Introductory Comments and Literature Review

The first two decades of structural optimization were almost totally focused on sizing design variables, such as cross-sectional area and thickness. There is another important class of structural design problems in which the structural geometric configuration or layout is to be determined. In the last ten years, this class of problems has drawn broad attention among researchers in academy and industry. The demand for a general algorithm to perform shape optimization of structural systems has grown, along with the development of CAD/CAM (computer aided design/manufacturing). Several numerical methods have been developed for shape design sensitivity analysis and optimization. One of the first treatments in the general problem of selecting the shape of a structure as the design variable was presented by Zienkiewicz and Campbell [1]. They formulated the shape optimal design problem using the finite element method, with the location of nodal joints of the finite element model as design variables. They evaluated derivatives of stiffness and load matrices with respect to design parameters to obtain derivatives of structural response measures (displacement or stress criteria) and employed sequential linear programming for numerical solution. Since then, many shape optimal design problems have been

solved by the finite element formulation. Ramachrishnan and Francavilla [2] used a penalty function method for numerical optimization of a clamped circular plate, a pressure vessel and closure, and a simplified gravity dam. Francavilla, Ramakrishnan, and Zienkiewicz [3] minimized stress concentration for a fillet problem. Schnack [4] and Oda [5] iteratively modified the contour of a notch to minimize the peak stress. Imam [6] optimized an engine bearing cap with generic modeling and a design component concept. Wassermann [7] optimized a three-dimensional arch dam with prescribed shape functions. Braibant and Fluery [8] optimized a beam in bending, a fillet, and a hole in a plate using B-splines. Wang, Sun, and Gallagher [9] presented sensitivity analysis in shape optimization of continuum structures by treating locations of nodal points of the finite element model as design parameters.

A more basic approach for surface contouring to minimize stress concentration were initiated by Tvergaard in selecting the optimum shape of a fillet [10]. He employed a stress field model of the fillet, with a finite dimensional family of perturbations allowed in the boundary shape, which is defined in terms of coordinate parameters. He employed a variational analysis of the stress field equations to obtain derivatives of stress with respect to his design parameters and used sequential linear programming to iteratively construct an optimum design. Kristensen and Madsen [11] formulated a class of shape optimal design problems for planar solids, which generalizes the approach of Tvergaard [10]. Bhavikatti and Ramakrishnan [12] presented a refinement

of the formulations of Ref. 1 for optimum design of fillets in flat and round tension bars.

Methods of optimality criteria have been used only for selected classes of shape optimal design problems. Kunar and Chan [13] used a fully stressed criteria and selected geometrical variables to minimize weight. Dems and Mroz [14] presented a general approach for shape optimization. They used a boundary perturbation analysis to derive optimality criteria and a finite element numerical method to determine the optimum boundary. Dems [15] used this method to formulate and numerically solve a variety of shape optimization problems to find optimum shape of shaft cross-section for tortional stiffness. Seguchi and Tada [16] applied the inverse variational principle to the potential energy functional which is adjoined by the total volume constraint with a Largrange multiplier to determine optimal shape of structures. Oda and Yamazaki [16] used the optimum distribution of material properties to obtain fully stressed shapes.

Dems and Mroz [18,19] applied the variational approach for sturctural optimization and shape design sensitivity analysis by means of adjoint systems. They also present first and second order sensitivity analysis of elastic structures, using a variational approach. A function space gradient projection method of shape optimal design of two-dimensional elastic bodies was presented by Chun and Haug [20,21], using design sensitivity analysis methods similar to those presented by Rousselet and Haug [22] and a gradient projection method of the kind presented in Ref. 23. Cea, Zolesio, and Rousselet

[24,25,26,27,28] presented techniques and applications from fields other than structural optimization, for selecting optimum domain. They have shown potential for optimality criteria and direct numerical methods for shape optimization of structures.

The method of Ref. 22 has been extensively expanded, both in theory and numerical implementations to cover much larger class of structural problems. Yoo, Haug, and Choi [29,30] applied this method to several plane elasticity problems of considerable size, such as a gravity dam and a connecting rod, by using the sparse matrix techniques [31]. Hou and Benedict [32] used this method to a torsion problem with shape constraints. Choi and Haug [33] developed shape design sensitivity formulas for five different prototype problems of elastic structures. Choi [34] studied shape design sensitivity analysis of displacement and stress constraint functionals, with emphasis on the effect of point and element movement within the domain, due to domain perturbation. Haug, Choi, and Komkov [35] have developed a unified variational form of structural design sensitivity analysis with a rigorous mathematical foundation. Lee, Choi, and Haug [36] applied the method to build-up structures with constraints on design variables, von-Mises yield stress, nodal displacement, and natural frequency.

Yang and Choi [37,38] improved the accuracy of shape design sensitivity for stress constraints by improving accuracy of boundary information, using higher order finite element with more sophisticated function evaluation schemes and smooth boundary representations. Yang and Botkin [39] used this method to perform three dimensional solid

shape optimization. Choi and Seong [40] further improved shape design sensitivity accuracy by using domain information. They also introduced a boundary layer idea to achieve efficient computation [41]. Choi, Santos, and Frederick [42] implemented design sensitivity analysis of a distributed design parameter system using ANSYS finite element code. Dopker and Choi [43] applied the method to both shallow and deep arch shape design sensitivity analysis. Also, build-up structures that include arches are investigated.

For more information relating to shape optimization literature, a review was given by Haug [44] and a survey was presented by Haftka [45].

1.2 Objectives and Scope

In all the literature cited, only Refs. 6, 7, 9 and 39 are involved with three dimensional shape problems. Most three-dimensional design problems have been simplified to convert them to two-dimensional problems. The main difficulties in general three dimensional shape optimization lie in the high computational cost and complicated surface shape design parametrization. Selection of design parametrization is a crucial step for successful shape optimization. It has been observed by several researchers [8,38] that an inappropriate scheme will lead to undesirable designs. To perform shape design sensitivity analysis by taking direct variation of finite element equation [9] is quite expensive.

It is proposed in this work to use the unified theory of shape design sensitivity analysis developed in Refs. 33-41, coupled with the

finite element method and parametric design representation using Bezier curves and surfaces to construct an accurate and efficient algorithm to perform general three dimensional shape design sensitivity analysis. In order to demonstrate the generality of this method, numerical implementations are constructed in a modulized fashion using a FORTRAN 77 programming language to interface with the ANSYS finite element analysis code.

The unified theory of shape design sensitivity analysis of Refs. 33-41 is introduced in Chapter 2. This theory, based on the material derivative of a continuum, defines a shape change as a design velocity field. Material derivatives of displacement, domain averaged stress, and pointwise stress are discussed. In Chapter 3, design parametrization of the boundary is presented using Bezier curves and surfaces.

In Chapter 4, numerical implementation of design velocity fields is discussed. The design velocity field provides the relationship between boundary perturbation and interior domain movement. To obtain this relationship, the governing equations of linear elastic structural systems can be used as the design velocity generator. The design velocity field generated can be used for automatic regridding, or even for grid generation. The boundary layer method [41] is also studied for computational efficiency. An algorithm for efficient design sensitivity computation is presented. In Chapter 5, shape design sensitivity analysis is carried out for three numerical examples: an engine bearing cap, a doubly-curved arch dam and the total hip joint replacement.

Shape optimization of an engine bearing cap and an arch dam are presented in Chapter 6. Discussions and conclusions are contained in Chapter 7.

CHAPTER 2

DOMAIN METHOD OF SHAPE DESIGN SENSITIVITY ANALYSIS

The fundamental concepts of the shape design sensitivity analysis developed in the text by Haug, Choi, and Komkov [35] are discussed briefly here. Details of rigorous mathematical derivation can be found in Refs. 22, 26, 33, 35, and 40.

A brief introduction to three dimensional linear elasticity is given in Section 2.1, as a convenient reference. Design velocity fields are discussed in Section 2.2.1, while the material derivative for different constraint functionals and the associated adjoint variable method are discussed in Sections 2.2.2 to 2.2.5. The first variation of the pointwise stress functional discussed in Section 2.2.5 is obtained directly by taking a limit of the material derivative of domain averaged stress functionals.

It was pointed out by Choi and Seong [40] that the domain integral form of shape design sensitivity expressions will yield excellent numerical result when results of finite element analysis are used to evaluate shape design sensitivity expressions. Therefore, the domain method of shape design sensitivity analysis of Ref. 40 is used here. The boundary integral form will be used only when it is necessary to account for boundary effects, such as the surface traction.

2.1 Three Dimensional Linear Elasticity

Consider the three dimensional linear elasticity problem for a body of arbitrary shape in the Cartesian coordinate system shown in Fig. 2.1. The displacement at each point of the elastic body, due to external loads, can be defined by the displacement vector $z = [z^1, z^2, z^3]^T$. The domain of this body is denoted by Ω, while its boundary is denoted by Γ.

The strain tensor is defined here as [46]

$$\varepsilon^{ij}(z) = (z^i_j + z^j_i)/2, \tag{2.1.1}$$

where the subscript i denotes derivative with respect x_i, while the superscript i indicates i-th component of the displacement vector. The stress-strain relation (the generalized Hook's law) is given as [46].

$$\sigma^{ij}(z) = \sum_{k,\ell=1}^{3} C^{ijk\ell}\varepsilon^{k\ell}(z), \qquad i,j,k,\ell = 1,2,3 \tag{2.1.2}$$

where $C^{ijk\ell}$ is the elastic modulus tensor, satisfying symmetry relations $C^{ijk\ell} = C^{jik\ell}$, $C^{ijk\ell} = C^{ij\ell k}$, and $C^{ijk\ell} = C^{k\ell ij}$, $i,j,k,\ell = 1,2,3$. The equilibrium equations are [46]

$$\sum_{j=1}^{3} \sigma^{ij}_j (z) + f^i = 0, \qquad i = 1,2,3, \qquad x \in \Omega \tag{2.1.3}$$

with the boundary conditions

$$z^i = 0, \qquad i = 1,2,3, \qquad x \in \Gamma^0 \tag{2.1.4}$$

and

$$T^{ni}(z) \equiv \sum_{j=1}^{3} \sigma^{ij}(z)n_j = T^i, \qquad i = 1,2,3, \qquad x \in \Gamma^2 \tag{2.1.5}$$

and

$$T^{ni}(z) = 0, \qquad i = 1,2,3, \qquad x \in \Gamma^1 \tag{2.1.6}$$

where $f = [f^1, f^2, f^3]^T \in [C^1(\overline{\Omega})]^3$ is the body force, vector n_j is the j-th component of the outward unit normal vector, and $T = [T^1, T^2, T^3]^T \in [C^1(\Gamma^2)]^3$ is the boundary traction vector.

The equilibrium equations of Eq. 2.1.3 can be reduced to a variational identity by multiplying both sides of Eq. 2.1.3 by an arbitrary displacement vector $\overline{z} = [\overline{z}^1, \overline{z}^2, \overline{z}^3]^T \in [H^1(\Omega)]^3$ and integrating by parts to obtain

$$\iiint_\Omega \Big[\sum_{i,j=1}^{3} \sigma^{ij}(z)\varepsilon^{ij}(\overline{z})\Big]d\Omega = \iiint_\Omega \Big[\sum_{i=1}^{3} f^i\overline{z}^i\Big]d\Omega$$

$$+ \iint_\Gamma \Big[\sum_{i,j=1}^{3} \sigma^{ij}(z)n_j\overline{z}^i\Big]d\Gamma, \qquad \text{for all } \overline{z}\in[H^1(\Omega)]^3 \tag{2.1.7}$$

Imposing the boundary conditions, the variational identity becomes a variational equation,

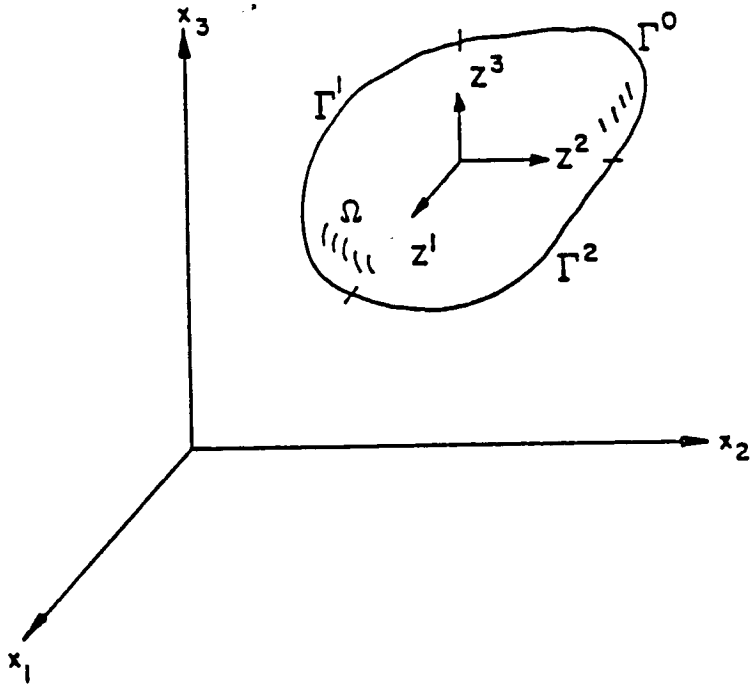

Figure 2.1 Three dimensional elastic solid

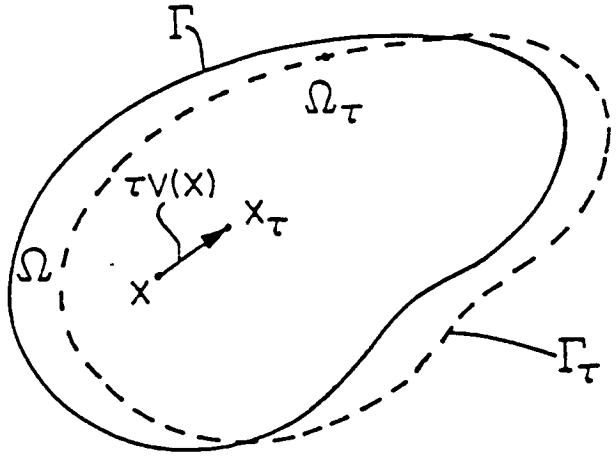

Figure 2.2 Deformation process

$$a_\Omega(z,\bar{z}) \equiv \iiint_\Omega \sum_{i,j=1}^{3} \sigma^{ij}(z)\varepsilon^{ij}(\bar{z})d\Omega$$

$$= \iiint_\Omega [\sum_{i=1}^{3} f^i\bar{z}^i]d\Omega + \iint_\Gamma [\sum_{i=1}^{3} T^i\bar{z}^i]d\Gamma$$

$$\equiv \ell_\Omega(\bar{z}), \qquad \text{for all } \bar{z} \in Z \tag{2.1.8}$$

where Z is the space of kinematically admissible displacements;

$$Z = \{z \in [H^1(\Omega)]^3: \ z^i = 0, \qquad i = 1,2,3, \qquad x \in \Gamma^0\} \tag{2.1.9}$$

In Eq. 2.1.8, $a_\Omega(z,\bar{z})$ and $\ell_\Omega(\bar{z})$ are denoted as the energy bilinear and load linear forms, respectively.

2.2 Shape Design Sensitivity Analysis

In shape design sensitivity analysis, the varying shape of a domain is treated as the design variable. The relationship between shape variation of a continuous domain and the related variations in some performance functionals can be naturally described by the material derivative. Before the concept of material derivative is presented, the design velocity field will be discussed first.

2.2.1 Design Velocity Field

The deformation process of a material domain Ω can be obtained by a mapping T: $x \to x_\tau(x)$, $x \in \Omega$, with a pseudo time parameter τ, by

$$x_\tau \equiv T(x,\tau),$$

$$\Omega_\tau \equiv T(\Omega,\tau), \text{ and} \tag{2.2.1}$$

$$\Gamma_\tau \equiv T(\Gamma,\tau).$$

The deformation process of Ω to Ω_τ by the mapping T may be viewed as a dynamic process of deforming a continuum, with τ playing the role of time. At the initial time $\tau = 0$, the domain is Ω. The initial point x moves to $x_\tau = T(x,\tau)$, see Fig. 2.2. A design velocity can be defined as [35]

$$V(x_\tau,\tau) \equiv \frac{dx_\tau}{d\tau} = \frac{dT(x,\tau)}{d\tau} = \frac{\partial T(x,\tau)}{\partial \tau} \tag{2.2.2}$$

Assuming T^{-1} exists, design velocity can be written as

$$V(x_\tau,\tau) = \frac{dx_\tau}{d\tau} = \frac{\partial T}{\partial \tau}\left[T^{-1}(x_\tau,\tau),\tau\right] \tag{2.2.3}$$

In the neighborhood of $\tau = 0$, with certain regularity hypothesis, T can be expanded using Taylor's series,

$$T(x,\tau) = T(x,0) + \tau \frac{\partial T}{\partial t}(x,0) + \cdots$$

Ignoring higher order terms,

$$T(x,\tau) = x + \tau\, V(x,0)$$

$$= x + \tau\, V(x), \tag{2.2.4}$$

where

$$x = T(x,0) \text{ and } V(x) = V(x,0).$$

2.2.2 Material Derivative of a General Functional

In the deformed domain Ω_τ, the solution $x_\tau(x_\tau)$ of the formal operator equation

$$A\, z_\tau = f, \qquad x \in \Omega_\tau, \tag{2.2.5}$$

defines $z_\tau = 0$, $x \in \Gamma_\tau$ a mapping on Ω,

$$z_\tau(x_\tau) \equiv z_\tau(x + \tau V(x)). \tag{2.2.6}$$

The pointwise material derivative of z at $x \in \Omega$ (if it exists) is defined as [35]

$$\dot{z} = \frac{d}{d\tau}\, z_\tau[x + \tau V(x)]\Big|_{\tau=0}$$

$$= \lim_{\tau\to 0} \left[\frac{z_\tau[x + \tau\, V(x)] - z(x)}{\tau}\right], \tag{2.2.7}$$

If z_τ has a regular extension to a neighborhood U_τ of $\overline{\Omega}_\tau$, denoted again as z_τ, then

$$\dot{z} = z'(x) + \nabla z^T V \tag{2.2.8}$$

where

$$z'(x) = \lim_{\tau \to 0} \left[\frac{z_\tau(x) - z(x)}{\tau}\right] \tag{2.2.9}$$

is the partial derivative with respect to τ and

$$\nabla z = [z_1, z_2, z_3]^T$$

Consider now a functional defined as an integral over Ω_τ,

$$\psi_1 = \iiint_{\Omega_\tau} f_\tau(x_\tau)\, d\Omega_\tau$$

$$= \iiint_{\Omega} f[x + \tau V(x)]\, |J|\, d\Omega \tag{2.2.10}$$

where f_τ is a regular functional defined in Ω_τ and J is the Jacobian matrix of the mapping T. The material derivative of ψ_1 at Ω is [35]

$$\psi_1' = \frac{d}{d\tau} \iiint_{\Omega} f[x + \tau V(x)]\, |J|\, d\Omega \Big|_{\tau=0}$$

$$= \iiint_{\Omega} [f' + \nabla f^T V + f(\text{div } V)]\, d\Omega \tag{2.2.11}$$

For a regular functional g defined as an integration over Γ_τ [35],

$$\psi_2 = \iint_{\Gamma_\tau} g_\tau(x_\tau)d\Gamma = \iint_{\Gamma} g_\tau(x+\tau V(x))\ |J|\ \|J^{-T}n\|\ d\Gamma \tag{2.2.12}$$

the material derivative is [35]

$$\psi_2' \equiv \frac{d}{d\tau} \iint_{\Gamma} g_\tau(x + \tau V(x))\ |J|\ \|J^{-T}n\|\ d\Gamma\Big|_{\tau=0}$$

$$= \iint_{\Gamma} [g'(x) + (\nabla g^T n + Hg(x))\ (V^T n)]\ d\Gamma \tag{2.2.13}$$

For a special case of Eq. 2.2.12 [35], where

$$g_\tau(x_\tau) = h_\tau(x_\tau)^T n_\tau, \tag{2.2.14}$$

the material derivative is

$$\psi_3' = \iint_{\Gamma} [h'(x)^T n + \text{div}\ h(V^T n)]\ d\Gamma \tag{2.2.15}$$

For kinematically admissible virtual displacement $\overline{z}$, it is shown in Ref. 35 that

$$\dot{\overline{z}} = \overline{z}' + \nabla\overline{z}^T V = 0. \tag{2.2.16}$$

Taking the material derivative of both side of Eq. 2.1.8,

$$[a(z,\overline{z})]' \equiv a'(z,\overline{z}) + a(\dot{z},\overline{z}) = \ell(\overline{z}), \qquad \text{for all } \overline{z} \in Z \tag{2.2.17}$$

Applying Eq. 2.2.11 to the energy bilinear form of Eq. 2.1.8 and expressing the result in terms of displacement and design velocity field,

$$a(\dot{z},\bar{z}) = \iiint_{\Omega} \sum_{i,j=1}^{3} [\sigma^{ij}(\dot{z})\varepsilon^{ij}(\bar{z})]\, d\Omega \tag{2.2.18}$$

$$a'(z,\bar{z}) = \iiint_{\Omega} \sum_{i,j=1}^{3} [- \sigma^{ij}(z)\ (\nabla\bar{z}^{iT}V_j) - \sigma^{ij}(\bar{z})(\nabla z^{iT}V_j)$$

$$+ \sigma^{ij}(z)\varepsilon^{ij}(\bar{z})\ (\text{div } V)]\, d\Omega \tag{2.2.19}$$

Applying Eqs. 2.2.11 and 2.2.13 to the load linear form of Eq. 2.1.8, the material derivative of the load linear form is

$$\ell'(\bar{z}) = \iiint_{\Omega} \sum_{i=1}^{3} [\bar{z}^{i}(\nabla f^{iT}V) + f^{i}\bar{z}^{i}\ (\text{div } V)]\, d\Omega$$

$$+ \iint_{\Gamma} \{ - \sum_{i=1}^{3} T^{i}(\nabla\bar{z}^{iT}V) + (\nabla[\sum_{i=1}^{3} T^{i}\bar{z}^{i}]n$$

$$+ H[\sum_{i=1}^{3} T^{i}\bar{z}^{i}])\ (V^{T}n)\}\, d\Gamma \tag{2.2.20}$$

The symbol H in the last term of right side of Eq. 2.2.20 denotes the curvature of the boundary Γ. Complete details of this derivation contained in the text by Haug, Choi, and Komkov [35].

Equation 2.2.17 is recasted to obtain the result

$$a(\dot{z},\bar{z}) = \ell'(\bar{z}) - a'(z,\bar{z})$$

$$= \iiint_{\Omega} \sum_{i,j=1}^{3} [\sigma^{ij}(z)\ (\nabla\bar{z}^{iT}V_j) + \sigma^{ij}(\bar{z})\ (\nabla z^{iT}V_j)$$

$$- \sigma^{ij}(z)\varepsilon^{ij}(\bar{z})\ (\text{div } V)]\ d\Omega$$

$$+ \iiint_{\Omega} \sum_{i=1}^{3} [\bar{z}^{i}(\nabla f^{iT}V) + f^{i}\bar{z}^{i}\ (\text{div } V)]\ d\Omega$$

$$+ \iint_{\Gamma} \{- \sum_{i=1}^{3} T^{i}(\nabla\bar{z}^{iT}V) + (\nabla[\sum_{i=1}^{3} T^{i}\bar{z}^{i}]n$$

$$+ H[\sum_{i=1}^{3} T^{i}\bar{z}^{i}])\ (V^{T}n)\}\ d\Gamma \qquad (2.2.21)$$

In the right hand side of Eq. 2.2.21, the first three terms are obtained from the expansion of $a'(z,\bar{z})$, while the fourth and fifth terms are from the material derivative of the load linear form of body force, and the sixth and seventh terms are from the material derivative of the load linear form of surface traction.

2.2.3 Material Derivative of Displacement

Consider the pointwise displacement constraint at a point $\hat{x}$,

$$\psi_1 = z^k(\hat{x}) = \iiint_{\Omega} \hat{\delta}(x-\hat{x})\ z^k(x)\ d\Omega, \qquad x \in \Omega \qquad (2.2.22)$$

where $\hat{\delta}(x)$ is the dirac measure at the origin. The material derivative of ψ_1 is

$$\psi_1' = \iiint_\Omega \hat{\delta}(x-\hat{x})\ \dot{z}^k(x)\ d\Omega, \qquad x \in \Omega \tag{2.2.23}$$

To express ψ_1' explicitly in terms of design velocity $V(x)$, an adjoint equation is defined as [35],

$$a(\lambda,\overline{\lambda}) = \iiint_\Omega \hat{\delta}(x-\hat{x})\ \overline{\lambda}^k\ d\Omega, \qquad \text{for all } \overline{\lambda} \in Z \tag{2.2.24}$$

With smoothness assumptions, Eq. 2.2.24 is equivalent to the formal operator equation

$$-\sum_{j=1}^{3} \sigma_j^{ij}(\lambda) = \hat{\delta}(x-\hat{x})\ \delta_{ki}, \qquad x \in \Omega \tag{2.2.25}$$

where δ_{ki} is the Kronecker delta. With the following boundary conditions:

$$\lambda^i = 0, \qquad i = 1,2,3, \qquad x \in \Gamma^0, \text{ and}$$

$$\sum_{j=1}^{3} \sigma^{ij}(\lambda)n_j = 0, \qquad i = 1,2,3, \qquad x \in \Gamma^1 \cup \Gamma^2. \tag{2.2.26}$$

Equations 2.2.24, 2.2.25, and 2.2.26 imply that the adjoint variable λ can be evaluated by solving Eq. 2.2.24 with a unit force applied at point $\hat{x}$, in the direction k. Equation 2.2.24 can be evaluated at $\overline{\lambda} = \dot{z}$, since $\dot{z} \in Z$,

$$a(\lambda,\dot{z}) = \iiint_\Omega \hat{\delta}(x-\hat{x})\ \dot{z}^k\ d\Omega \tag{2.2.27}$$

The identity of Eq. 2.2.21 can be evaluated at $\overline{z} = \lambda$, since both $\overline{z}$ and $\lambda \in Z$, to obtain

$$a(\dot{z},\lambda) = \ell'(\lambda) - a'(z,\lambda) \tag{2.2.28}$$

Based on Betti's reciprocal theorem, the energy bilinear form is symmetric with respect to its arguments. Therefore, the left sides of Eqs. 2.2.27 and 2.2.28 are equal, thus yielding

$$a(\lambda,\dot{z}) = a(\dot{z},\lambda) \tag{2.2.29}$$

That is,

$$\psi_1' = \iiint_\Omega \hat{\delta}(x-\hat{x})\ \dot{z}^k\ d\Omega = \ell'(\lambda) - a'(z,\lambda) \tag{2.2.30}$$

To evaluate ψ_1' in Eqs. 2.2.30, Eq. 2.1.8 and 2.2.24 must be solved to obtain z and λ, respectively. Then,

$$\begin{aligned}\psi_1' = \iiint_\Omega \sum_{i,j=1}^{3} & [\sigma^{ij}(z)\ (\nabla\lambda^{iT}V_j) + \sigma^{ij}(\lambda)\ (\nabla z^{iT}V_j) \\ & - \sigma^{ij}(z)\varepsilon^{ij}(\lambda)\ (\text{div } V)]\ d\Omega \\ + \iiint_\Omega \sum_{i=1}^{3} & [\lambda^i(\nabla f^{iT}V) + f^i\lambda^i\ (\text{div } V)]\ d\Omega \\ + \iint_\Gamma \{-\sum_{i=1}^{3} & T^i(\nabla\lambda^{iT}V) + (\nabla[\sum_{i=1}^{3} T^i\lambda^i]n \\ & + H[\sum_{i=1}^{3} T^i\lambda^i])\ (V^Tn)\}\ d\Gamma\end{aligned} \tag{2.2.31}$$

2.2.4 Material Derivative of General Stress Functional

Let $g(\sigma(z))$ be a function of stress, such as principal stress, octahedral, or von-Mises equivalent stress. Then the averaged stress functional over a small region $\Omega_p \in \Omega$ is

$$\psi_2 = \iiint_{\Omega} g(\sigma(z))m_p \, d\Omega$$

$$= \iiint_{\Omega} g(\sigma(z)) \, d\Omega / \iiint_{\Omega_p} d\Omega \tag{2.2.32}$$

where m_p is a characteristic function [35], defined as

$$m_p \begin{cases} = 1/\iiint_{\Omega_p} d\Omega, & x \in \Omega_p \\ = 0 \quad , & x \in \Omega/\Omega_p \end{cases} \tag{2.2.33}$$

The material derivative of ψ_2 is

$$\psi_2' = \iiint_{\Omega} (g' + \nabla g^T V + g(\text{div } V))m_p \, d\Omega$$

$$- \iiint_{\Omega} g m_p d\Omega \iiint_{\Omega} (\text{div } V) m_p d\Omega \tag{2.2.34}$$

which can be rewritten as [35]

$$\psi_2' = \iiint_{\Omega} \sum_{i,j=1}^{3} g_{\sigma^{ij}}(z) \, [\sigma^{ij}(\dot{z}) - \sigma^{ij}(\nabla z^T V)] m_p \, d\Omega$$

$$+ \iiint_{\Omega} \sum_{k=1}^{3} [\sum_{i,j=1}^{3} g_{\sigma^{ij}}(z) \, \sigma_k^{ij}(z) V^k] m_p \, d\Omega$$

$$+ \iiint_{\Omega} g(\text{div } V) m_p \, d\Omega - \iiint_{\Omega} g \, m_p d_{\Omega} \iiint_{\Omega} (\text{div } V) m_p \, d\Omega \tag{2.2.35}$$

Using the relations [40]

$$\sigma^{ij}(\nabla z^T V) = \sum_{k,\ell=1}^{3} C^{ijk\ell}(\nabla z_\ell^{k^T} V + \nabla z^{k^T} V_\ell), \text{ and}$$

$$\sum_{k=1}^{3} \sigma_k^{ij}(z)V^k = \sum_{k,\ell=1}^{3} C^{ijk\ell}(\nabla z_\ell^{k^T} V) \tag{2.2.36}$$

Eq. 2.2.35 can be reduced to

$$\begin{aligned}\psi_2' = &\iiint_\Omega \Big[\sum_{i,j=1}^{3} g_{\sigma^{ij}}(z)\sigma^{ij}(\dot{z})\Big]m_p \, d\Omega \\ &- \iiint_\Omega \sum_{i,j=1}^{3} [g_{\sigma^{ij}}(z)C^{ijk\ell}(\nabla z^{k^T} V_\ell)m_p \, d\Omega \\ &+ \iiint_\Omega g(\text{div } V)m_p \, d\Omega - \iiint_\Omega g \, m_p \, d\Omega \iiint_\Omega (\text{Div } V)m_p \, d\Omega\end{aligned} \tag{2.2.37}$$

The adjoint equation in this case is

$$a(\lambda,\overline{\lambda}) = \iiint_\Omega \sum_{i,j=1}^{3} g_{\sigma^{ij}}(z)\sigma^{ij}(\overline{\lambda})m_p \, d\Omega, \qquad \text{for all } \overline{\lambda} \in Z \tag{2.2.38}$$

which corresponds to the formal operator equation

$$-\sum_{j=1}^{3} \sigma_j^{ij}(\lambda) = -\sum_{j=1}^{3} \Big(\sum_{k,\ell=1}^{3} g_{\sigma^{k\ell}}(z)C^{k\ell ij}m_p\Big)_j, \qquad i = 1,2,3, \qquad x \in \Omega \tag{2.2.39}$$

with the same boundary conditions as in Eq. 2.2.26. Evaluating Eq. 2.2.38 at $\overline{\lambda} = \dot{z}$, since $\dot{z} \in Z$,

$$a(\lambda,\dot{z}) = \iiint_{\Omega} \sum_{i,j=1}^{3} g_{\sigma^{ij}}(z)\sigma^{ij}(\dot{z})m_p \, d\Omega \tag{2.2.40}$$

Also, Eq. 2.2.21 can be evaluated at $\bar{z} = \lambda$, since both $\bar{z}$ and $\lambda \in Z$,

$$a(\dot{z},\lambda) = \ell'(\lambda) - a'(z,\lambda) \tag{2.2.41}$$

Due to symmetry of the energy bilinear form, Eqs. 2.2.40 and 2.2.41 are equal, and the first term on the right side of Eq. 2.2.37 can be replaced by Eq. 2.2.41. Therefore, ψ_2' becomes

$$\begin{aligned}
\psi_2' = {} & \iiint_{\Omega} \sum_{i,j=1}^{3} [\sigma^{ij}(z)\,(\nabla\lambda^{iT}V_j) + \sigma^{ij}(\lambda)\,(\nabla z^{iT}V_j) \\
& \qquad - \sigma^{ij}(z)\varepsilon^{ij}(\lambda)\,(\operatorname{div} V)]\, d\Omega \\
& + \iiint_{\Omega} \sum_{i=1}^{3} [\lambda^i(\nabla f^{iT}V) + f^i\lambda^i\,(\operatorname{div} V)]\, d\Omega \\
& + \iint_{\Gamma} \{-\sum_{i=1}^{3} T^i(\nabla\lambda^{iT}V) + (\nabla[\sum_{i=1}^{3} T^i\lambda^i]n \\
& \qquad + H[\sum_{i=1}^{3} T^i\lambda^i])\,(V^Tn)\}\, d\Gamma \\
& - \iiint_{\Omega} \sum_{i,j=1}^{3} [\sum_{k,\ell=1}^{3} g_{\sigma^{ij}}(z)C^{ijk\ell}(\nabla z^{k^T}V_\ell)m_p \, d\Omega \\
& + \iiint_{\Omega} g(\operatorname{div} V)m_p \, d\Omega - \iiint_{\Omega} gm_p \, d\Omega \iiint_{\Omega} (\operatorname{div} V)m_p \, d\Omega
\end{aligned} \tag{2.2.42}$$

Note that the last three terms of Eq. 2.2.42 are nonzero only on the small test region Ω_p.

For a very smooth stress state, the domain averaged constraint functional is sufficient and economical in representing structural performance measures, since the entire domain can be covered by a finite number of constraints. For example, each finite element may be considered as a test region. For large stress variations, a very small test region should be considered for domain averaged stress, in order to obtain meaningful performance measures of the structure for shape design problems. For example, stress at a nodal point may be considered as a performance measure [7,8,9,39]. However, it is well known that most finite element approximations do not provide continuous stress at a nodal point. To alleviate this difficulty, a Gaussian point can be considered to measure stresses. For continuous stress, design sensitivity of the pointwise stress can be obtained as a special case of the domain averaged form. That is, it can be derived directly from domain averaged form by taking the limit as the test region shrinks to a point. Since Gaussian points are the optimal locations to sample stresses, it is recommended that the test region to be shrunk to a Gaussian point. Furthermore, stress is continuous at the Gaussian point in finite element approximations.

2.2.5 Material Derivative of Pointwise Stress Functional

For smooth domain and data, stress will be continuous. In this case, a pointwise stress functional can be considered for design sensitivity analysis. Define the pointwise stress functional ψ_3 as

$$\psi_3 = \iiint_\Omega \hat{\delta}(x-\hat{x})\, g(\sigma(z))\, d\Omega \tag{2.2.43}$$

where $\hat{x}$ is the Gaussian point at which stress sensitivity is to be evaluated. Equation 2.2.43 can also be obtained from Eq. 2.2.32 by taking a limit. That is, if the test region Ω_p shrinks to the point $\hat{x} \in \Omega_p$, the characteristic function m_p will become a Dirac measure. An adjoint equation for this case can be obtained by taking the limit of Eq. 2.2.38 as Ω_p shrinks to the point $\hat{x}$,

$$a(\lambda,\overline{\lambda}) = \iiint_\Omega \delta(x-\hat{x}) \sum_{i,j=1}^{3} g_{\sigma^{ij}}(z)\sigma^{ij}(\overline{\lambda})\, d\Omega \tag{2.2.44}$$

For the design sensitivity expression, taking the limit of Eq. 2.2.42 as Ω_p shrinks to $\hat{x}$,

$$\begin{aligned}
\psi_3' = \iiint_\Omega \sum_{i,j=1}^{3} & [\sigma^{ij}(z)\,(\nabla\lambda^{iT}V_j) + \sigma^{ij}(\lambda)\,(\nabla z^{iT}V_j) \\
& - \sigma^{ij}(z)\varepsilon^{ij}(\lambda)\,(\mathrm{div}\ V)]\, d\Omega \\
& + \iiint_\Omega \sum_{i=1}^{3} [\lambda^i(\nabla f^{iT}V) + f^i\lambda^i\,(\mathrm{div}\ V)]\, d\Omega \\
& + \iint_\Gamma \{-\sum_{i=1}^{3} T^i(\nabla\lambda^{iT}V) + (\nabla[\sum_{i=1}^{3} T^i\lambda^i]n \\
& \quad + H[\sum_{i=1}^{3} T^i\lambda^i])\,(V^Tn)\}\, d\Gamma \\
& - \iiint_\Omega \delta(x-\hat{x}) \sum_{i,j=1}^{3} [\sum_{k,\ell=1}^{3} g_{\sigma^{ij}}(z)C^{ijk\ell}(\nabla z^{k^T}V_\ell)]\, d\Omega
\end{aligned} \tag{2.2.45}$$

The last two terms of Eq. 2.2.42 disappear as Ω_p shrinks to point $\hat{x}$. This can be seen easily, since the characteristic function m_p becomes a Dirac measure, and the last two terms of Eq. 2.2.42 cancel each other.

It has been shown in Ref. 40 that a C^1 regular velocity field is sufficient for shape design sensitivity analysis of elastic solid problems. However, in observing Eqs. 2.2.31, 2.2.42, and 2.2.45, this regularity condition can be relaxed. Since the highest order derivative of the velocity field is one, a C^0 regular velocity field may be used with an integrable first derivative [40]. Therefore, regularity of the velocity field must be at least at the level of the displacement field of the structural component treated.

Notice also that design velocity is involved in each term of all shape design sensitivity expressions given in Eqs. 2.2.30, 2.2.42, and 2.2.45. An abstract form of the material derivative of displacement and stress functional may be presented as

$$\psi = \iiint_{\Omega} f_0(z,\lambda,V)d\Omega + \iint_{\Gamma} g_0(z,\lambda,V)\, d\Gamma \tag{2.2.46}$$

Hence, it is necessary to define design velocity field both on the domain and the boundary. The boundary velocity can be obtained directly from the boundary shape perturbation, but the interior domain velocity must be constructed in certain manner to reflect the influence of the boundary perturbation upon the entire domain. When the finite element method is used to perform shape design sensitivity analysis and optimization, computation of design velocity field is of great

importance to the success of shape optimization, especially when a very large shape change is involved, since the original finite element grid may be subjected to severe distortion during deformation of shape and result in numerical difficulties, as observed in Ref. 38. There are, however, infinitely many ways to define the design velocity field for a given boundary perturbation. Two methods of defining domain velocity fields are considered here. First, the relation between the boundary perturbation and domain perturbation may be considered as a purely geometric problem and solved it by geometric rules. In the second method, the relationship can be obtained from a physical problem, and solved using the associated governing equations. The geometric approach is straight forward and cheaper to use. However, when it is necessary to preserve regularity of the finite element grid, the second approach is favorable, since a regular design velocity field (finite element grid) can be obtained.

CHAPTER 3

DESIGN PARAMETERIZATION

In structural shape design optimization, the varying boundary is treated as the design variable. Therefore, it is necessary to perform boundary shape design parametrization. The result of shape optimization is naturally limited by the design parametrization used. To reach a better optimal shape design, the design parametrization must be general and flexible enough to represent a large class of structural shapes.

In the literature, Francavilla et al. [3] applied quadratic and fifth degree polynomials for a fillet and a connecting rod, respectively. Reinschmidt and Narayanan [47] used a hyperbolic curve in optimizing the shape of a cooling tower. Bhavikatti and Ramakrishnan [48] used a third order polynomial in optimizing the cross section of a pressure vessel and nozzle junction. They also used a general third degree function in the coordinates of x and y axis to optimize the shape of shoulder fillets in tension bars and T-heads [12]. Queau and Trompette [49] used straight lines and circles to describe a boundary. Tai et al. [50] optimized the shape of an airfoil, using a combination of three baseline shapes. More recently, Wassermann [7] defined position and tangent vectors as design variables to optimize a three dimensional arch dam. Braibant and Fluery [8] adopted B-spline and Bezier curves to optimize the shapes of a bending beam, a fillet, and

a hole in a plate. Choi and Seong [41] used B-splines and velocity elements to optimize a fillet. Iman [6] categorized the shape parametrization scheme as independent node movement, design element, super curves, and superposition of shapes.

Among techniques developed in the field of computer aided geometric design [51,52], it is not clear which method fits the purpose of parametric shape representation best. Several factors, such as efficiency in application, smoothness, fairness and continuity of the curves generated, flexibility, generality, and controlability in global or local senses must be considered. Global control means that the effect of design perturbation will spread everywhere in the varying boundary, while local control means the effect of design perturbation will be limited in a local region along the varying boundary. It is also desirable to have a variation diminishing property, so that the perturbed shape will retain the level of smoothness of the original shape.

In the spline family, B-splines are most widely used in shape modeling, since B-splines have most of the desirable characteristics mentioned above. B-splines has been applied in shape optimization in Refs. 8 and 40. Low order B-splines provide local control only. One possible drawback of local control is that an unrealistic design may occur, when a large shape perturbation is induced by a small perturbation in the structural response. This has been observed in Ref. 8. To solve this problem, either higher order B-splines are used or some optimization constraints, such as the boundary regularity constraints [53], can be introduced to achieve global control.

The Bezier curve is a special case of the B-spline that can be generated in a simpler fashion. It has been applied in car body design by engineers of Renault automobiles for nearly two decades. For simplicity, Bezier curves and surfaces are selected here to demonstrate the process of boundary shape design parametrization. In the following discussions, several properties of Bezier curves and surfaces will be reviewed and used to develop the boundary parametrization.

3.1 Boundary Shape Design Parametrization and Boundary Velocity

Boundary shape design parametrization may be considered as a linear mapping X from a design parameter $b = [b_1, b_2, \ldots \ldots b_N]$ to the x_i-coordinate of the varying boundary, denoted by a position vector $x_i(b)$ (Fig 3.1). That is X: $b \dashrightarrow x_i(b)$, where

$$x_i(b) = S_1 b_1 + S_2 b_2 + \ldots\ldots + S_N b_N, \tag{3.1.1}$$

with S_n as shape functions determined by the mapping used. To cover a broad class of structural shapes, S_n can be defined as polynomials, spline functions, or base shapes.

Perturbation of the boundary, denoted by $\delta x_i(b)$, due to perturbation (δb) of design parameters is determined by taking the variation of both sides of Eq. 3.1.1. That is

$$\delta x_i(b) = \sum_{n=1}^{N} S_n \, \delta b_n, \tag{3.1.2}$$

On the varying boundary segment, the boundary perturbation is interpreted as the boundary velocity.

Let the i-th component of the boundary velocity, due to perturbation of design parameters be denoted as $V_i(b)$,

$$V_i(b) \equiv \delta x_i(b) = \sum_{n=1}^{N} S_n \delta b_n \tag{3.1.3}$$

For example, let a second degree polynomial $f(x_1)$ be used to describe the x_2-coordinate of a segment of a curved boundary spanned by three nodes, as shown in Fig. 3.2.;

$$x_2(b) = f(x_1) = b_1 x_1^2 + b_2 x_1 + b_3 \tag{3.1.4}$$

or

$$x_2(b) = f(x_1) = [x_1^2 \quad x_1 \quad 1] \begin{bmatrix} b_1 \\ b_2 \\ b_3 \end{bmatrix} \tag{3.1.5}$$

Let design variable b be perturbed by δb. Then the perturbation on this curve is

$$\delta x_2(b) = \delta f(x_1) = [x_1^2 \quad x_1 \quad 1] \begin{bmatrix} \delta b_1 \\ \delta b_2 \\ \delta b_3 \end{bmatrix} \tag{3.1.6}$$

which is the boundary velocity $V_2(b)$, according to Eq. 3.1.3.

Design parameters b_1, b_2, and b_3 for a given curve can be determined in the following manner. Let P_1x_1, P_2x_1, and P_3x_1 be x_1-coordinate of three different nodes on the curve, and let the design parametrization mapping be expressed in matrix form in terms of nodal coordinates; i.e.,

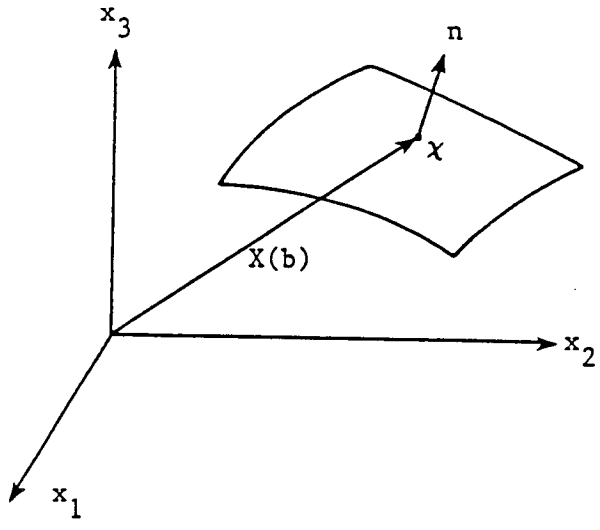

Figure 3.1 Parametric representation of shape

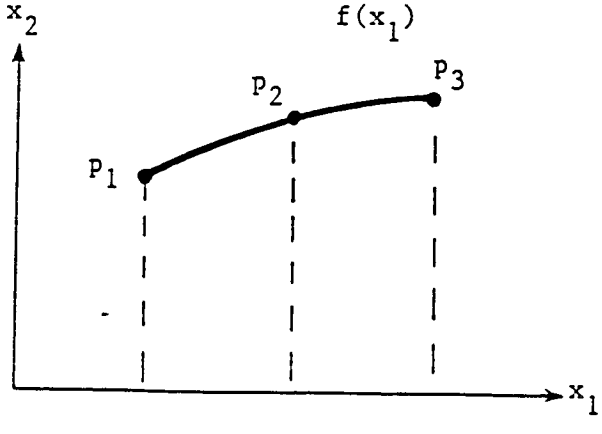

Figure 3.2 Quadratic polynomial

$$\begin{bmatrix} P_1x_2 \\ P_2x_2 \\ P_3x_2 \end{bmatrix} = \begin{bmatrix} P_1x_1^2 & P_1x_1 & 1 \\ P_2x_1^2 & P_2x_1 & 1 \\ P_3x_1^2 & P_3x_1 & 1 \end{bmatrix} \cdot \begin{bmatrix} b_1 \\ b_2 \\ b_3 \end{bmatrix} \tag{3.1.7}$$

With given nodal coordinates, b_1, b_2, and b_3 can be obtained by solving Eq. 3.1.7.

3.2 Bezier Curves and Surfaces

3.2.1 Bezier Curves

The Bezier curve [54] P(v) is constructed by taking a linear combination of a Bernstein basis with certain weights. The Bernstein basis functions $B_{n,N}(v)$ are generated from a binomial factorial F(N,n) as

$$B_{n,N}(v) = F(N,n)\ v^n\ (1-v)^{N-n} \tag{3.2.1}$$

where $F(N,n) = N!/(n!)[(N-n)!]$, $0 < v < 1$, N is the degree of the basis, and n denotes the particular weight in the ordered set (n = 0, 1, 2, ..., N).

Taking a linear combination of $B_{n,N}(v)$ with different weight coefficients C_n, n = 0, 1, 2, ... N, different Bezier curves P(v) can be obtained as

$$P(v) = \sum_{n=0}^{N} C_n B_{n,N}(v) \tag{3.2.2}$$

For example, a set of 6 blending functions are shown in Fig. 3.3, where $N = 5$ and $n = 0, 1, 2, 3, 4, 5$. For simplicity in indexing, $B_n(v)$ is used to denote $B_{n,N}(v)$.

The weights C_n can be interpreted as vertical positions of control points, as shown in Fig. 3.4. The control points form a series of convex hulls, and the related Bezier curve will always lie within these convex hulls. For example, let a Bezier curve be defined as

$$P(v) = \sum_{n=0}^{3} C_n B_n(v), \qquad n = 0,1,2,3 \tag{3.2.3}$$

$$= C_0B_0(v) + C_1B_1(v) + C_2B_2(v) + C_3B_3(v)$$

In Fig. 3.2.2, note that at the first node, $v = 0$, $P(0) = C_0$ (since $B_0(0) = 1$), and $B_1(0) = B_2(0) = B_3(0) = 0$. Similarly, at the fourth node, $v = 1$, $P(1) = C_3$, (since $B_3(1) = 1$), and $B_0(1) = B_1(1) = B_2(1) = 0$. That is, the starting and end node of the Bezier curve coincide with the first and last control points, respectively. The middle two nodes are linear combinations of four nonzero components, so no direct relationship can be identified.

A plane curve $Px_i(v)$ in the Cartesian x_1-x_2 plane can be written in Bezier blending form. For clarity, a matrix form can be used to represent a Bezier curve with N+1 control points as

$$Px_i(v) = [B_0B_1 \cdots B_N] \begin{bmatrix} C_0x_i \\ C_1x_i \\ \vdots \\ C_Nx_i \end{bmatrix}, \qquad i = 1,2 \tag{3.2.4}$$

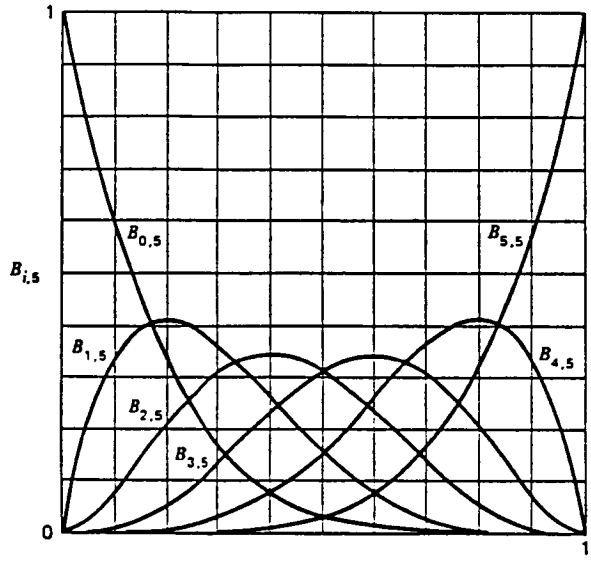

Figure 3.3 Bernstein basis

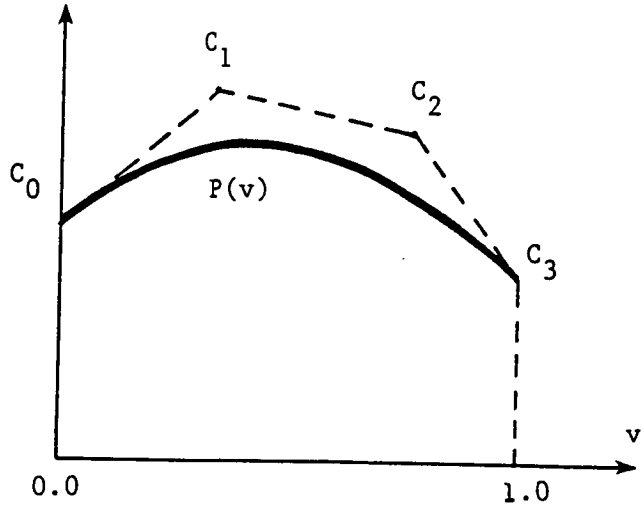

Figure 3.4 Bezier curve

where $C_n x_i$ is the x_i-coordinate of the n-th control point. For a curve in space, simply add the x_3 component in Eq. 3.2.4. An example of a plane curve $Px_i(v)$ is given in Fig. 3.5.

Perturbation of the Bezier curve, due to a perturbed control point, can be easily obtained. For example, let the x_i-coordinate of control point C_n, $n = 0,1,..,N$, be perturbed by $\delta C_n x_i$. Then the perturbation of the Bezier curve can be obtained from Eq. 3.2.4 as

$$\delta Px_i(v) = [B_0 B_1 \cdots B_N] \begin{bmatrix} \delta C_0 x_i \\ \delta C_1 x_i \\ \vdots \\ \delta C_N x_i \end{bmatrix}, \qquad i = 1,2 \tag{3.2.5}$$

In Eq. 3.2.5, $\delta Px_i(v)$ is the perturbation of a Bezier curve, due to perturbation on the position of control point $C_n x_i$, $n = 0,1,\ldots,N$. Equation 3.2.5 shows that perturbation of the curve $Px_i(v)$ due to perturbation of the x_i coordinate of the control point C_n is the Bernstein basis multiplied by the perturbation $\delta C_n x_i$ (Fig. 3.6).

Bezier curves have several characteristics that are very important in geometric parametrization. These properties are as follows [55]:

1. Control Points. Although not all control points lie on the Bezier curve, it is not difficult to predict the locations of control points relating to the curve, since each control point exerts a 'pulling' effect on the curve near it. The Bezier curve does pass through the two endpoints, and the curve is tangent at the endpoints to the related edge of the polygon of control points.

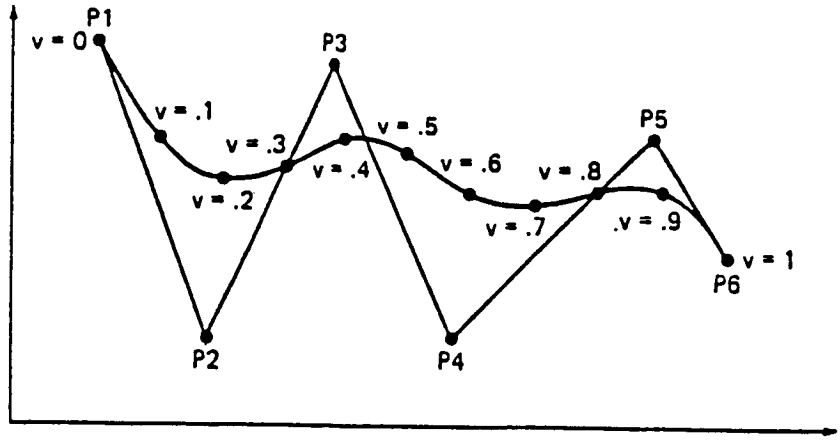

Figure 3.5 Bezier curve in the x_1-x_2 plane

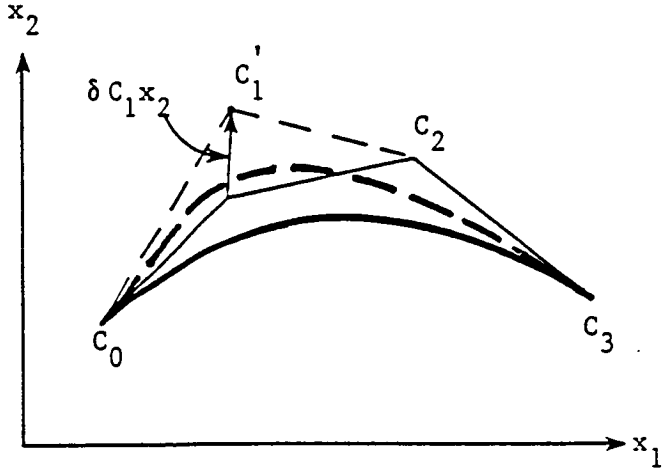

Figure 3.6 Perturbation of a Bezier curve

2. Multiple values. The parametric formulation of the Bezier curve allows it to represent multiple-valued shapes. In fact, if the first and last control points coincide, the curve is closed. This is demonstrated in Fig. 3.7.
3. Axis independence. The Bezier curve is independent of the coordinate system used to locate control points.
4. Global control. Global control can be seen from Eq. 3.2.2. All basis functions are nonzero almost everywhere (except at the two ends $v = 0$ and $v = 1$). Consequently, the location of a control point will influence the curve shape almost everywhere.
5. Variation-diminishing property. Bezier curves are variation-diminishing. Further, a curve is guaranteed to lie within the convex hull of the control points that define it [56]. This can be seen in Fig. 3.5. Thus the Bezier curve never oscillates wildly away from its defining control points.
6. Versatility. The versatility of Bezier curves is governed by the control points assigned. In the example of Fig. 3.5, six control points are used ($N=5$) to determine two parametric fifth order polynomial functions that specify x_1 and x_2 values. More control points can always be used to represent more complex shapes, but the high-order polynomial equations become difficult to use because of the lack of localized control. To solve this problem, several low-order Bezier curves may be pieced together, with certain continuity conditions, to describe a more complex curve.

7. Order of continuity. Pieced Bezier curves can have different orders of continuity at joints. To achieve zero-order continuity at a joint, it is necessary only to make the end control points of two curves coincide (Fig. 3.8). To achieve first order continuity, the edges of two polygons adjacent to the common endpoints must lie in a line (Fig. 3.9). Thus it is rather easy to locate control points to achieve first-order continuity. Higher-order continuity can be ensured by geometric constraints on control points, but beyond first-order continuity the construction becomes complicated.

8. If $C_1 = C_2 = \ldots\ldots = C_N = C_0$, then Eq. 3.2.2 becomes

$$P(v) = C_0 \sum_{n=0}^{N} B_n(v) = C_0 \tag{3.2.6}$$

that is

$$\sum_{n=0}^{N} B_n(v) = 1 \tag{3.2.7}$$

This means that when the control points are located on a straight line, the associated Bezier curve will also lie on the same straight line.

For a curved shape, it is necessary to perform the following procedure to determine positions of the control points corresponding to a given boundary. The process is outlined by the following four steps:

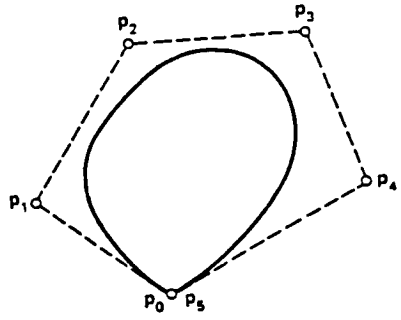

Figure 3.7 Closed Bezier curve

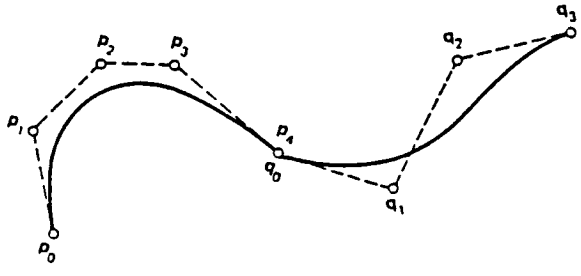

Figure 3.8 Zero-order continuity of Bezier curve

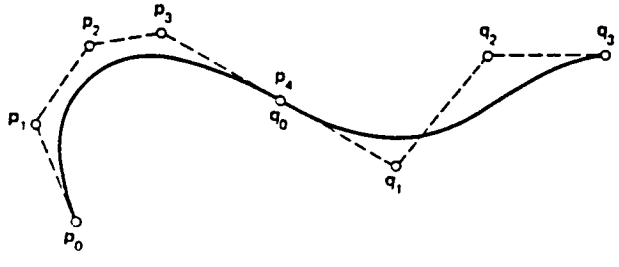

Figure 3.9 First-order continuity of Bezier curve

STEP 1

Select a set of points P_m, m = 1, 2, ..., M, on the curve. Normalize the x_i-coordinates of all nodes. That is, let the x_i-coordinate of node P_m be denoted by $P_m x_i$ and the normalized x_i-coordinate of node P_m be denoted by v_m,

$$v_m = (P_m x_i - P_1 x_i)/|P_M x_i - P_1 x_i|, \tag{3.2.8}$$

STEP 2

With the x_i-coordinates of M nodes normalized, the position of M nodes in each of the M Bernstein basis can be found by using the normalized x_i-coordinates in Eq. 3.2.1 as v. This step will result in an M x M matrix [BMTX]. The components of this matrix are,

$$\begin{matrix} B_0(v_1) & B_1(v_1) & - - - & B_N(v_1) \\ B_0(v_2) & B_1(v_2) & - - - & B_N(v_2) \\ - & - & - - - & - \\ B_0(v_M) & B_1(v_M) & - - - & B_N(v_M) \end{matrix} \tag{3.2.9}$$

where N = M-1 and $B_n(v_m)$ denotes the n-th Bezier basis evaluated at v_m, the normalized x_i-coordinate of the m-th node in the given curve.

STEP 3

Equation 3.2.4 can be converted to a matrix form by replacing the Bezier basis with the matrix of Eq. 3.2.9. That is,

$$\{P_m x_i\} = [BMTX]\ \{C_m x_i\}, \qquad i = 1,2 \tag{3.2.10}$$

In Eq. 3.2.10, $\{P_m x_i\}$ is a vector with M components denoting x_i-coordinate of selected nodes and $\{C_m x_i\}$ is a vector with M components denoting x_i-coordinates of the unknown control points, while [BMTX] is an MxM matrix constructed in Eq. 3.2.9. The matrix [BMTX] is invertible [57]. Therefore, Eq. 3.2.10 can be solved to obtain $\{C_m x_i\}$, for a given $\{P_m x_i\}$.

3.2.2 Bezier Surfaces

The construction of a Bezier surface is similar to that of a Bezier curve. The Bezier surface generating equations are given by [54]

$$Px_i(v,w) = \sum_{m=0}^{M} \sum_{n=0}^{N} C_{mn} x_i \; B_{m,M}(v) \; D_{n,N}(w) \tag{3.2.11}$$

where $B_{m,M}(v)$ and $D_{n,N}(w)$ are two sets of Bezier curve blending functions, given in Eq. 3.2.1, and $C_{mn} x_i$ denotes the x_i-coordinate of control point C_{mn}, i = 1,2,3. For example, a 4x4 Bezier surface is illustrated by solid lines in Fig. 3.10, while the polygons formed by the control points are shown as dashed lines.

The procedure of obtaining the positions of control points for a given surface is very similar to that for a curve. This procedure is the same for all x_1, x_2, and x_3-coordinates:

<u>STEP 1</u>

Define an M-row and N-column matrix of x_i-coordinates of the nodes on a given surface, and perform discretization on parameter v for row

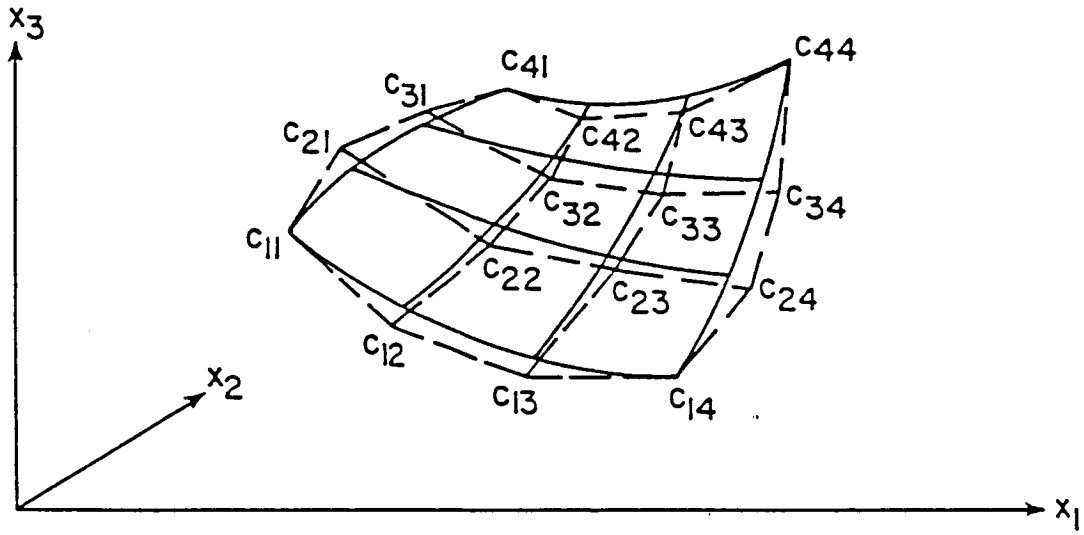

$$P_{x_i}(v,w) = \sum_{m=0}^{M} \sum_{n=0}^{N} c_{mnx_i} B_{m,M}(v) D_{n,N}(w), \quad i = 1,2,3$$

Figure 3.10 4x4 Bezier surface

and column directions, in the same way as that was discussed in step 1 of Section 3.2.1.

STEP 2

Form two Bezier matrices [BMTX] and [DMTX], in the same manner as that was shown in Eq. 3.2.9. Here [BMTX] is an MxM matrix and [DMTX] is an NxN matrix.

STEP 3

Similar to the case of a Bezier curve, Eq. 3.2.11 can be converted to matrix form by replacing the two Bezier basis $B_{m,M}(v)$ and $D_{n,N}(v)$ with the two matrices [BMTX] and [DMTX],

$$\underset{MxN}{[P_{mn}x_i]} = \underset{MxM}{[BMTX]}\ \underset{MxN}{[C_{mn}x_i]}\ \underset{NxN}{[DMTX]} \tag{3.2.12}$$

where $[P_{mn}x_i]$ is a matrix denoting the MxN x_i-coordinates of the nodes selected. Since both matrices [BMTX] and [DMTX] are non-singular [57], their inverses exist. The matrix $[C_{mn}x_i]$ contains the x_i-coordinates of control points C_{mn} and can be obtained from

$$\underset{MxN}{[C_{mn}x_i]} = \underset{MxM}{[BMTX]^{-1}}\ \underset{MxN}{[P_{mn}x_i]}\ \underset{NxN}{[DMTX]^{-1}} \tag{3.2.13}$$

Perturbation of a Bezier surface can be determined in a manner similar to that of a Bezier curve. Let δPx_i denote a perturbation of the x_i-coordinate of a Bezier surface, due to a perturbation the x_i-coordinate of the control point C_{mn}, m = 0, 1, .., M, n = 0, 1, .., N. Then, δPx_i can be expressed as

$$\delta Px_i(v,w) = [B_0 B_1 \cdots B_N] \begin{bmatrix} \delta C_{00}x_i & \delta C_{01}x_i & \cdots & \delta C_{0M}x_i \\ \delta C_{10}x_i & \delta C_{11}x_i & \cdots & \delta C_{1M}x_i \\ \vdots & \vdots & \vdots & \vdots \\ \delta C_{N0}x_i & \delta C_{N1}x_i & \cdots & \delta C_{NM}x_i \end{bmatrix} \begin{bmatrix} D_0 \\ D_1 \\ \vdots \\ D_M \end{bmatrix} \tag{3.2.14}$$

For example, when a 4x4 Bezier surface is perturbed by perturbing the x_i position of control point C_{12}, the matrix form can be written as

$$\delta Px_i = [B_0 B_1 B_2 B_3] \begin{bmatrix} 0 & 0 & 0 & 0 \\ 0 & 0 & \delta C_{12}x_i & 0 \\ 0 & 0 & 0 & 0 \\ 0 & 0 & 0 & 0 \end{bmatrix} \begin{bmatrix} D_0 \\ D_1 \\ D_2 \\ D_3 \end{bmatrix} \tag{3.2.15}$$

3.2.3 Design Parametrization with Bezier Curves and Surfaces

It is interesting to note that perturbation of Bezier curves and surfaces in Eq. 3.2.5 and Eq. 3.2.14 are linearly depending upon the perturbation of position of the control points. This suggests that the positions of control points can be used as shape design parameters.

If the x_i position of control point $C_n x_i$ or $C_{mn} x_i$ is considered as design parameter b_n or b_{mn}, then a perturbation of the Bezier curve or

surface corresponding to this control point can be interpreted as a boundary velocity. For a Bezier curve, Eq. 3.2.8 yields

$$V_i(b) = \delta P x_i(v) = [B_0 B_1 \cdots B_N] \begin{bmatrix} \delta C_0 x_i \\ \delta C_1 x_i \\ \vdots \\ \delta C_N x_i \end{bmatrix}, \; i = 1,2 \tag{3.2.16}$$

For a Bezier surface, Eq. 3.2.14 yields

$$V_i(b) = \delta P x_i(v,w) = [B_0 B_1 \cdots B_N] \begin{bmatrix} \delta C_{00} x_i & \delta C_{01} x_i & \cdots & \delta C_{0M} x_i \\ \delta C_{10} x_i & \delta C_{11} x_i & \cdots & \delta C_{1M} x_i \\ \vdots & \vdots & \vdots & \vdots \\ \delta C_{N0} x_i & \delta C_{N1} x_i & \cdot & \delta C_{NM} x_i \end{bmatrix} \begin{bmatrix} D_0 \\ D_1 \\ \vdots \\ D_M \end{bmatrix} \tag{3.2.17}$$

In Chapter 2, it was noted that shape design sensitivity analysis requires a domain velocity field. If N design parameters are defined, it is necessary to determine N sets of domain design velocity fields. This can be done by perturbing each design parameter, to obtain the corresponding boundary velocity, and using either the geometric approach or the boundary displacement approach to determine the associated domain velocity field.

CHAPTER 4

AUTOMATIC REGRIDDING AND DESIGN VELOCITY FIELD

Numerical analysis of a structure, using a finite element or finite difference method, requires discretizing the entire structure into a finite grid. Accuracy of analysis results is greatly influenced by the size and aspect ratio (squareness) of the grid. The art of generating a grid to achieve accurate analysis has been studied by many researchers. Zienkiewicz and Phillips [58] developed an automatic mesh generation scheme for plane and curved surfaces, using 'isoparametric' coordinates. Buell and Bush [59] presented a survey on mesh generation, covering many nodal generation and element generation schemes; straight line interpolation, sides-and-parts, simplified finite difference, electro- mechanical hardware, and equipotential methods. Thacker [60] presented a brief review of techniques for generating irregular computational grids.

Haber et al. [61] created a general two-dimensional, graphical finite element preprocessor, utilizing discrete transfinite mappings for automatic mesh generation. Thompson, Warsi, and Mastin [62] went through a comprehensive review of methods of numerically generating curvilinear coordinate systems with coordinate lines coincident with all boundary segments. More recently, Cavendish et al. [63] developed an

approach for automatic three-dimensional finite element mesh generation.

It has been observed in Ref. 63 that the most powerful mesh generators developed to date are referred to interpolators or interpolation mesh generators. These generators require some initial form of gross partitioning of the structure into simpler sub-regions. A sub-region is then modeled by first approximating its bounding edges by parametric space curves [52], usually low-order polynomials or piecewice polynomial interpolants. Space curves are then combined to form contour curves or surfaces (for example, Bezier curve or Bezier surface) and the curves or surfaces are then combined to define an approximation region. The entire process is equivalent to the construction of a vector-valued mapping from a canonical domain (for example, a square or a cube) onto a sub-region. The mapping may interpolate the sub-region at a finite [57] number of points. The mapping produces an explicit mathematical description of the sub-region and can be used to induce a natural coordinate upon it (usually rectangular).

4.1 Computation of Design Velocity Field and Automatic Regridding

Two methods for design velocity field generation are considered here. The first uses geometric rules that can be found in most mesh generators. The second approach uses finite element analysis results, by treating the boundary perturbation as an external load, which results in interior domain movement.

4.1.1 Mesh Generation Method

In order to take the advantage of the existing automatic mesh generation methods, the design velocity field may be considered as the difference between the original mesh and the mesh corresponding to a perturbed design. In the finite element modeling process, there are usually some nodes to be selected as key points in describing the contour of the model. Interior nodes can be generated automatically by certain kinds of interpolation; e.g. linear interpolation. Let the position of some of the key points be related to geometric design parameters. Then, for each perturbation of a design parameter, there will be a set of key points perturbed accordingly. The new positions of key points will lead to a new mesh, through automatic mesh generation. Let the position vector of the nodal point of the original mesh be denoted by Gox_i, and the position vector of the new mesh corresponding to perturbation of the n-th design parameter be denoted by Gnx_i. The associated design velocity field Vn_i can then be expressed as

$$Vn_i = Gnx_i - Gox_i \tag{4.1.1}$$

where x_i indicates the x_i-coordinate. As was pointed out in Section 2.2.5, the design velocity field for linear elasticity is required to be at least C^0-regular, with an integrable first derivative. It was observed in Ref.41 that violation on this regularity condition will lead to errors. Fortunately, this regularity condition can be satisfied by linear interpolation schemes that are used in mesh generation methods.

The advantage of this method lies in its simplicity and efficiency. However, there are also some major drawbacks that raise great concern. First, grid orthogonality, one of the most important characteristics of a good mesh may be destroyed during the mesh regenerating process. This can be seen in Fig. 4.1a, where a rectangular membrane is divided into smaller rectangles, using the ANSYS mesh generator. This rectangular membrane is then deformed and remeshed to make a fillet shape, as shown in Fig. 4.1b. Note that there are several distorted rectangles in the transition region. Kikuchi et al. [64] pointed out that excessive distortion of finite elements may lead to significant approximation errors, and consequently, loss of accuracy in shape design sensitivity analysis. Thus, the mesh generation method is not suitable for regridding in shape design sensitivity. Certainly it is possible to manipulate the mesh generator to find a reasonable remeshing, but it will not be a systematic approach. Therefore, another method must be developed to resolve this problem.

4.1.2 Boundary Displacement Method

The regularity condition on design velocity fields suggests that displacement shape functions may be used to systematically define the velocity field in the domain. Moreover, a velocity field that obeys the governing equation of the structure can be selected. That is, the perturbation of the boundary can be considered as a displacement at the boundary. With no additional external forces, but only a given displacement at the boundary The same finite element code used for

analysis can be used to find the displacement (domain velocity) field that satisfies the required regularity conditions. That is,

$$[K]\ \{V\} = \{f\} \tag{4.1.2}$$

where [K] is the reduced stiffness matrix, {V} is the velocity vector of the nodes in the varying domain, and {f} is the unknown fictitious boundary force that produces the perturbation of the boundary. In segmented form, Eq. 4.1.2 becomes

$$\begin{bmatrix} K_{bb} & K_{bd} \\ K_{db} & K_{dd} \end{bmatrix} \begin{bmatrix} V_b \\ V_d \end{bmatrix} = \begin{bmatrix} f_b \\ 0 \end{bmatrix} \tag{4.1.3}$$

where $\{V_b\}$ is the given perturbation of nodes on the boundary, $\{V_d\}$ is the nodal velocity vector in the interior of the domain, and $\{f_b\}$ is the fictitious boundary force acting on the varying boundary. An equation for the unknown interior nodal velocity vector can be obtained from Eq. 4.1.3 as

$$[K_{dd}]\ \{V_d\} = -[K_{db}]\{V_b\} \tag{4.1.4}$$

which defines a linear relation between the boundary and domain design velocity fields.

The boundary displacement method is applied to the fillet example considered in Section 4.1.1. It is interesting to observe that this method has the tendency to preserve grid orthogonality and that grid

distortion near the transition area that was shown in Fig. 4.1b is smoothly absorbed by the entire domain in Fig. 4.2. Thus, the boundary displacement method of automatic regridding does not deteriorate the accuracy of analysis, provided that the initial mesh is optimized. The one-step deformation, process shown in Fig. 4.2 is broken down to four steps, using the updated stiffness matrix of Eq. 4.1.3 at each step, as shown in Fig. 4.3. The final meshes obtained from the two different processes are slightly different, with the difference between nodal locations less than 3 % in this case. The largest difference came from the region around the corner of transition, where curvature change is the largest. Also, both cases render similar grid distortion patterns.

The orthogonality-preserving and nearly path-independent merits of this method, together with linear dependence of the design velocity field on design parameters suggest that structural shape optimization using this automatic regridding method can be carried out without intermediate mesh regeneration, for several design iterations. That is, there may be no need to solve Eq. 4.1.3 for each updated shape. Due to its simplicity and generality, this automatic regridding method is quite general. In applying this method, computational efficiency can be obtained by suppressing a large number of degrees-of-freedom, for a fixed shape contour and specified degrees-of-freedom, for only varying portions of the boundary, to set up Eq. 4.1.3. For this purpose, a substructuring technique, or a smaller model, may be used to define the varying region for design velocity field computation.

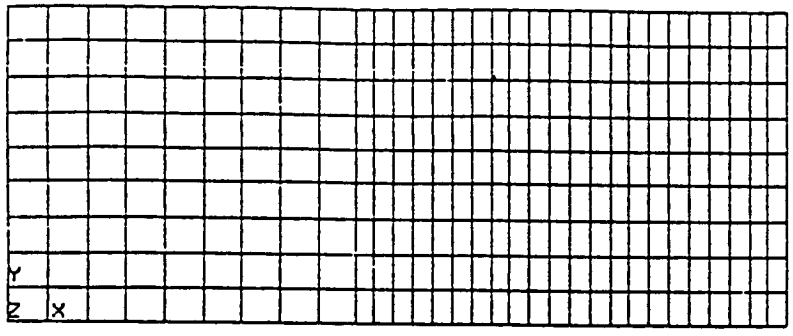

(a) Original grid

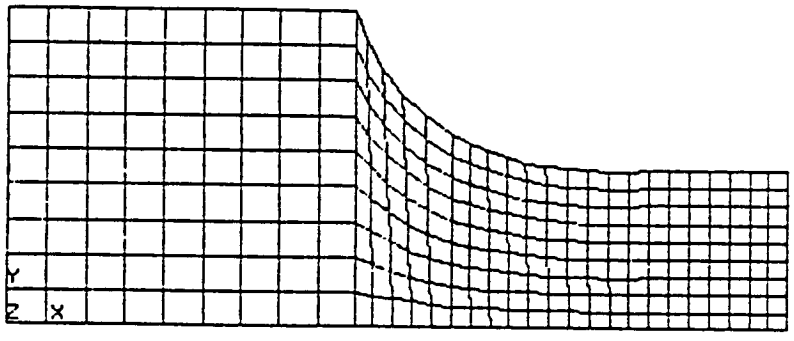

(b) Remeshed grid

Figure 4.1 Mesh generation method for fillet

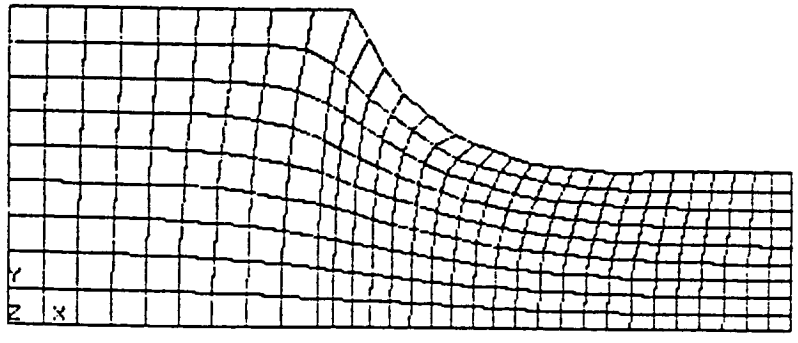

Figure 4.2 Boundary deformation method for fillet

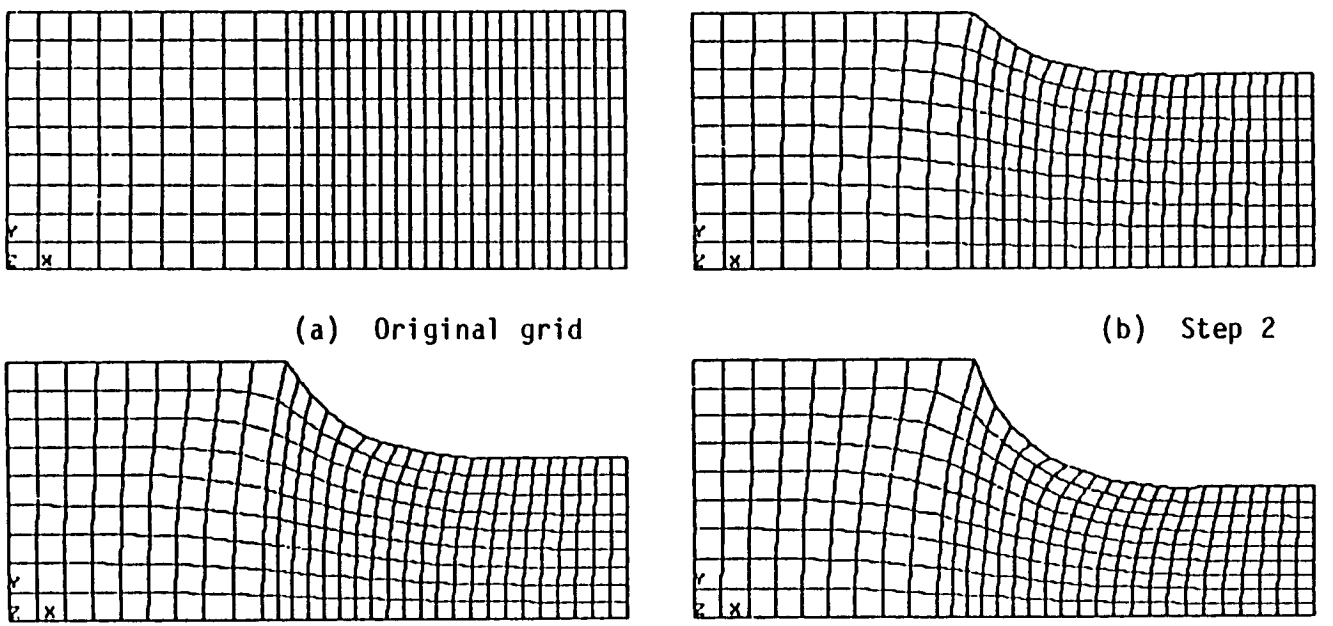

(a) Original grid

(b) Step 2

(c) Step 3

(d) Step 4

Figure 4.3 Boundary deformation method with incremental deformations

This regridding method can also be utilized as a mesh generator. The procedure is similar to the fillet example demonstrated. That is, starting with a regular shape with a regular mesh, a mesh can be generated using Eq. 4.1.3, while deforming the regular shape to a desired shape. When this regridding method is used as a mesh generator, Eq. 4.1.3 need be solved only once. In a region where stress concentration is predicted, intensity of the mesh may be increased to obtain a finer mesh. This procedure is similar to the procedure used in boundary fitted curvilinear coordinate systems, except that the mapping equations are different. In boundary-fitted coordinate systems, the mapping equations can be chosen from the family of elliptic equations. The original shape is first mapped to a regular (rectangular) shape. The locations of interior nodes are then obtained by solving the selected elliptic equation, iteratively, with boundary nodal locations as the boundary conditions. This method is more expensive than the boundary displacement method, especially when there are several design velocity fields to be defined. In the boundary displacement method, the stiffness matrix of Eq. 4.1.3 needs to be decomposed only once for the first set of design velocity fields., Other sets of design velocity fields can be obtained by forward and backward substitution.

From the above discussions, it can be seen that treating the boundary-domain velocity mapping with the system governing equation will yield efficient automatic regridding, with mesh orthogonality being preserved.

4.2 Boundary Layer

The domain integral form of design sensitivity analysis requires substantial computation effort, since it is necessary to integrate shape sensitivity expressions over the varying domain. To achieve computational efficiency, it is desirable to reduce this integration work. Braibant and fleury [8] observed that a few design elements are generally sufficient to fully describe the region that is modified during optimization, but did not provide the rationale of their observation.

Choi and Seong [41] presented the idea of a 'boundary layer coordinate system', with mathematical reasoning and geometric construction scheme, with a velocity element to define design the velocity field in the boundary layer. A boundary layer is illustrated in Fig. 4.4, it is a region specified to cover the varying domain. They used the boundary layer in two dimensional fillet and interface problems [41]. Excellent sensitivity results were reported, with significant saving in computational time. They also suggested use of the strain energy density distribution as a criteria to systematically quantify the boundary layer direction, size, and location.

To avoid numerical errors due to grid distortion, a boundary layer must be large enough. A coarse model of the fillet shown in Fig. 4.5 is used to visualize grid distortion due to automatic regridding, using the boundary displacement method, with dashed lines showing the original grid and solid lines showing the deformed grid. It can be seen in Fig.

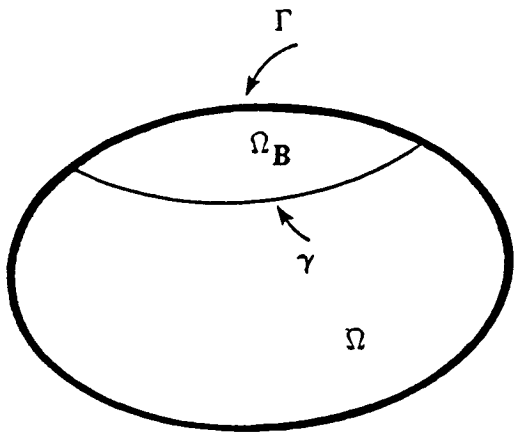

Figure 4.4 A boundary layer

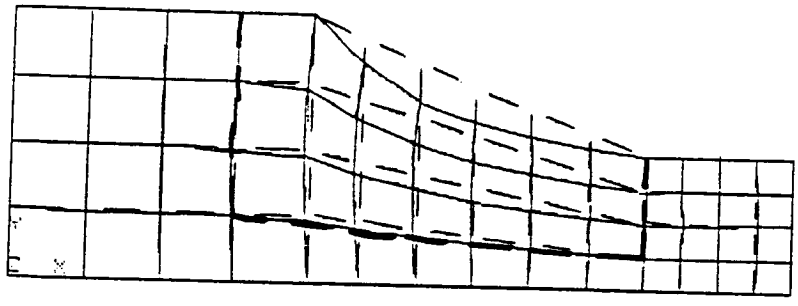

Figure 4.5 Fillet boundary layer

4.5 that significant grid distortion appears mainly in the middle portion of the fillet. A possible boundary layer for this case is framed by heavy dashed lines. This suggested boundary layer is similar to the one used in Ref. 41, where strain energy density is used as the criteria to determine the boundary layer. Numerical experiments show that the boundary layer can be very small [41]. However, in order to avoid excessive grid distortion, it is necessary to either define a sufficiently large boundary layer, to accommodate large shape change, or define a small boundary layer and regenerate the grid after a few design iterations.

4.3 Computational Algorithm for Efficient Shape Design Sensitivity Analysis

To evaluate shape design sensitivity expressions, the finite element method is used. The finite element code ANSYS is used to perform structural stress analysis and an interface program provided by the Swanson Analysis Systems, Inc. is applied to retrieve analysis results from ANSYS data files. There are two approaches to retrieving data from ANSYS. The first is to acquire and store all data in the beginning of sensitivity analysis. The second approach is to retrieve only necessary data at one time for local computation. The first approach requires much larger initial data storage than the second. However, it has been experienced that when an interface program is used for data transfer, it will increase the INPUT/OUTPUT time and detract from computational efficiency, especially in a super computer.

Therefore, the preferable approach is to store all necessary information at one time, rather than to retrieve local data so often.

A computational algorithm is usually written in modular form, for clarity and simplicity. However, modular the form increases INPUT/OUTPUT time. To achieve computational efficiency, the number of modules in a program should be kept to a minimum. The major part of shape design sensitivity computational effort is used in computing and integrating derivatives of displacements, adjoint displacements, and velocity fields. The computational procedure must be carried out in a systematic manner, to avoid repetition.

The general procedure for shape design sensitivity analysis is described in the following steps:

STEP 1

Define a finite element model of the physical problem, and select shape design parameters, in the manner discussed in Chapter 3.

STEP 2

Carry out finite element stress analysis.

STEP 3

Construct a design velocity field, using either mesh-generation or boundary displacement methods.

STEP 4

Compute adjoint load sets for active constraints.

STEP 5

Carry out adjoint analysis.

STEP 6

Evaluate shape design sensitivity, based on the algorithm that follows.

4.4 Shape Design Sensitivity Computational Algorithm

The displacement sensitivity expression of Eq. 2.2.31 is used as an example, to demonstrate the proposed computational algorithm. The algorithm starts with data management. Information on the displacement field z, adjoint displacement field λ, design velocity field V, and constraint definition indices are stored in a data file. After the data file is established, proceed to compute design sensitivity in three levels.

Level 1. Domain integration.

In this level, nodal locations and element connectivity and material properties are retrieved from ANSYS data files, following the element numbering sequence. Design sensitivity analysis is then carried out, element by element.

Level 2. Element integration (Gaussian point integration).

For each element, shape design sensitivity expressions are evaluated using Gaussian integration. That is, the shape design

sensitivity value for each element is represented by the summation of the value of all Gaussian points (27 in this case). To obtain shape design sensitivity, it is necessary to evaluate z^i_j, the first derivatives of the displacement field. In the finite element method, z^i_j is obtained by multiplying the first derivatives of shape functions with the displacement vector. Strain $\varepsilon^{ij}(z)$ and stress $\sigma^{ij}(z)$ tensors are obtained from z^i_j.

The algorithm then moves into the innermost level, where sensitivity expressions for each constraint (the adjoint variable) and each design parameter are evaluated.

Level 3. Adjoint variable and design parameter.

Sensitivity evaluation requires the values of the first derivatives of the adjoint displacement field λ^i_j and design velocity field V^i_j. These terms can be obtained in a similar manner as that for z^i_j. The adjoint strain $\varepsilon^{ij}(\lambda)$ and stress $\sigma^{ij}(\lambda)$ tensors are also constructed and stored.

Displacement sensitivity at each Gaussian point, for each constraint and design parameter, is then evaluated. Element sensitivity is obtained by summing the sensitivity value at each Gaussian point. The algorithm then moves to the next element, to repeat the computation of levels 2 and 3, until all elements are exhausted. Domain sensitivity is obtained by summing element sensitivities.

The surface traction variational effect must be evaluated along the traction boundary. This can be accomplished by boundary integration. The procedure is exactly the same as the procedure from level 1, 2, and 3, except that Gaussian points are now located at the traction surface.

CHAPTER 5

SHAPE DESIGN SENSITIVITY ANALYSIS

To demonstrate the feasibility of shape design sensitivity analysis using geometric modeling and automatic regridding, three different types of 3-D solid structures are tested numerically and discussed in this chapter. The first example tested is an engine bearing cap, a mechanical part that is used to secure engine crank shaft to the engine body. The cap is required not to deform more than a tolerable clearance to provide adequate lubrication. This problem was investigated first by Imam [6], and later by Yang and Botkin [39].

The second example is a three dimensional arch dam, that was optimized first by Wassermann [7]. The main concern of the 3-D arch dam lies in prediction of the effect of variation in self-weight and water pressure due to shape change. Another concern is design parametrization. Since the arch dam forms a three dimensional closed surface (or an envelope), it is necessary to parametrize two surfaces (upstream and downstream sides).

The third example tested is the total hip joint reconstruction [65] in orthopedic surgery. Total hip arthroplasty has been performed by surgeons for over one hundred fifty years. As the medical and biological environments are improving, problems of prothesis service life span is now mostly closely to mechanical performances. In this

problem, prothesis strength and geometry, cement strength and thickness, and bone strength must be dealt with simultaneously.

5.1 Engine Bearing Cap

Shape design sensitivity analysis is carried out for the engine bearing cap of Fig. 5.1 [6]. Since it is intended to demonstrate feasibility of the proposed method of shape design sensitivity analysis, the structure and loading condition of the cap will be reasonably simplified and yet general enough to demonstrate feasibility of the method. The cap is modeled as a three dimensional linear elasticity problem, in which the cap is subjected to 5000 psi uniform oil film pressure transmitted from the engine shaft bearing and bolt clamping force of 14,775 lb. on the top of cap. The cap structure is assumed to be symmetric with respect to the center line, so that only half of the finite element model is used for analysis and sensitivity analysis. The cap finite element model consists of 82 20-node isoparametric solid elements (ANSYS STIF95, Fig. 5.2), with 768 nodes and 2304 degrees-of-freedom. The model is shown in Fig. 5.3. For a ductile steel cap, Young's modulus is 30. Mpsi and Poison's ratio is 0.3.

The boundary conditions used in Ref. 6 are adopted here. It was confirmed by finite element analyses that the flat bottom surfaces of a cap remain in firm contact with the journal, even under the highest oil film pressure load. Therefore fixed boundary conditions for nodes on the flat bottom surfaces of the cap are justified. All other nodes are free to move in any direction, except nodes on the plane of symmetry are

ORIGINAL PAGE IS
OF POOR QUALITY

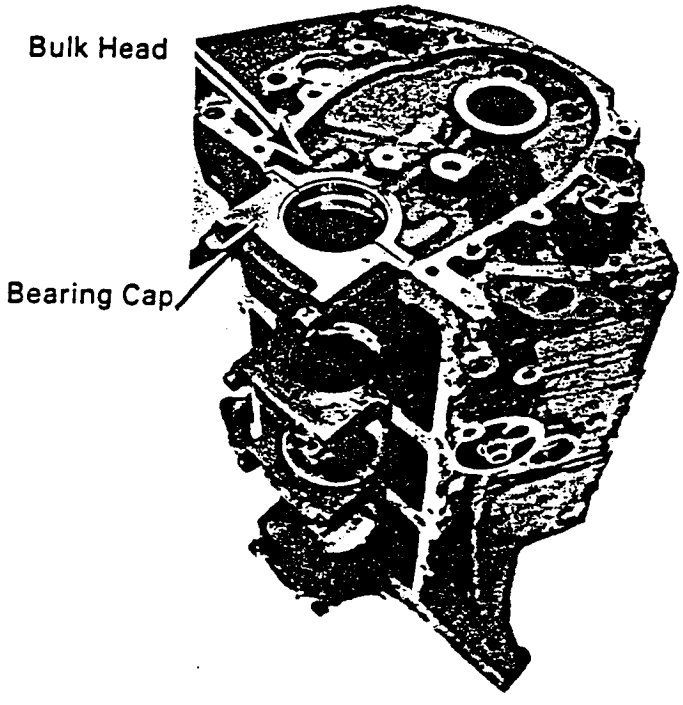

Figure 5.1 Engine bearing cap

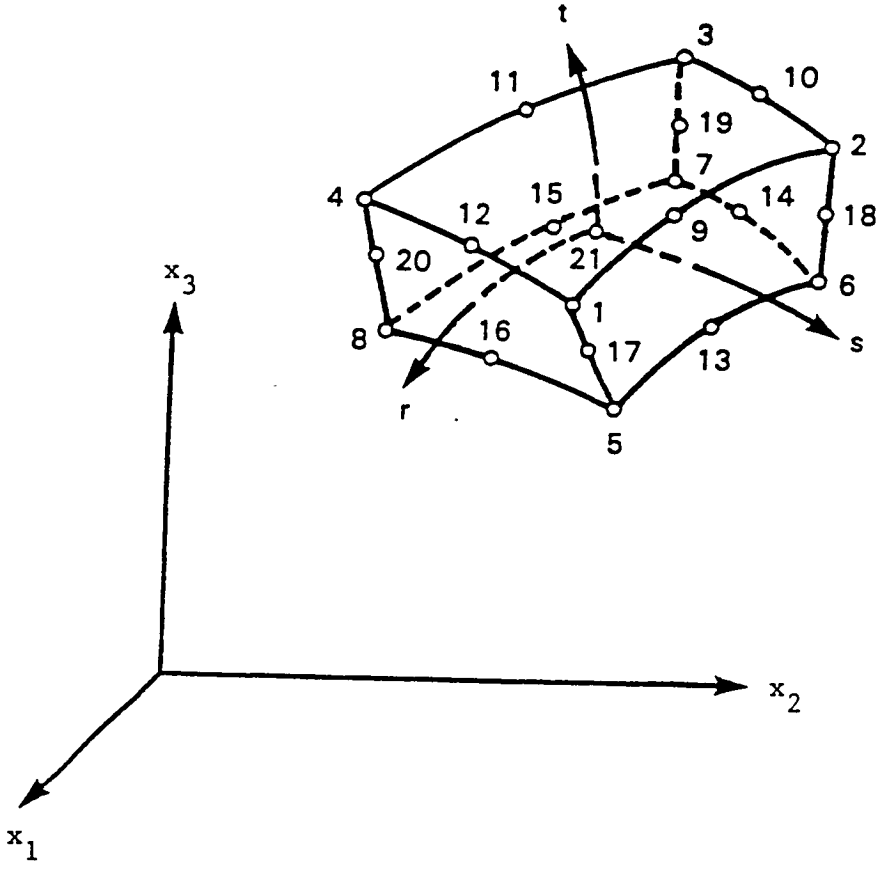

Figure 5.2 20 node isoparametric solid finite element

constrained in the x_1-direction, due to the structural symmetry assumption.

The top of bearing cap is parameterized by a Bezier surface with 4 control points, as shown in Fig. 5.4. The Bezier surface is assumed to have curvature in the x_1-direction only. The x_2-coordinates of these control points are selected as the first four design parameters. The distance of the center line of clamping bolt from the center line of cap is chosen as the fifth design parameter, while the distance of the cap edge from the center line of cap is defined as the sixth design parameter.

The boundary displacement method is used to generate six sets of design velocity fields, corresponding to six design parameters. For the first four sets of design velocity fields, the boundary velocities are determined by perturbing the x_2-coordinate of each control point a unit magnitude, using Eq. 3.2.17. The associated domain velocity fields are obtained by solving Eq. 4.1.3.

In order to achieve computational efficiency, the boundary layer idea is used to generate design velocity fields corresponding to design parameter 5 and 6. For design parameter 5, the boundary layer consists of 25 (out of 82) elements, as shown in Fig. 5.5, while only 15 (out of 82) elements along the cap edge are used to define the boundary layer for design parameter 6, as shown in Fig. 5.1.6.

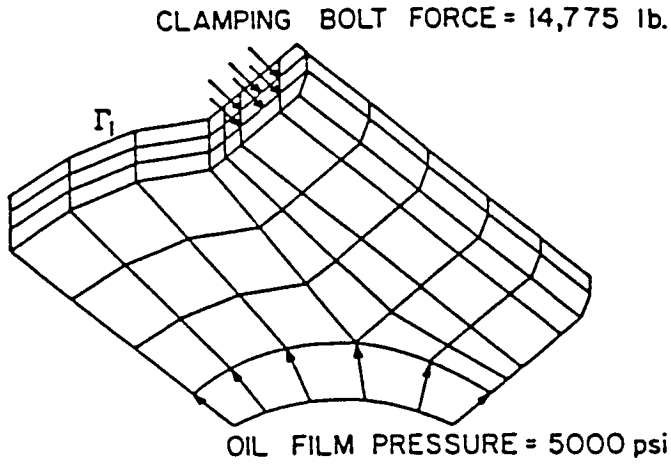

Figure 5.3 Finite element model of engine bearing cap

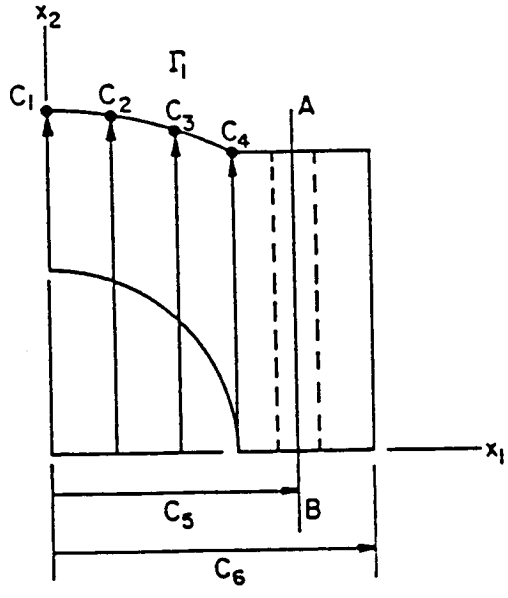

Figure 5.4 Definition of cap design parameters

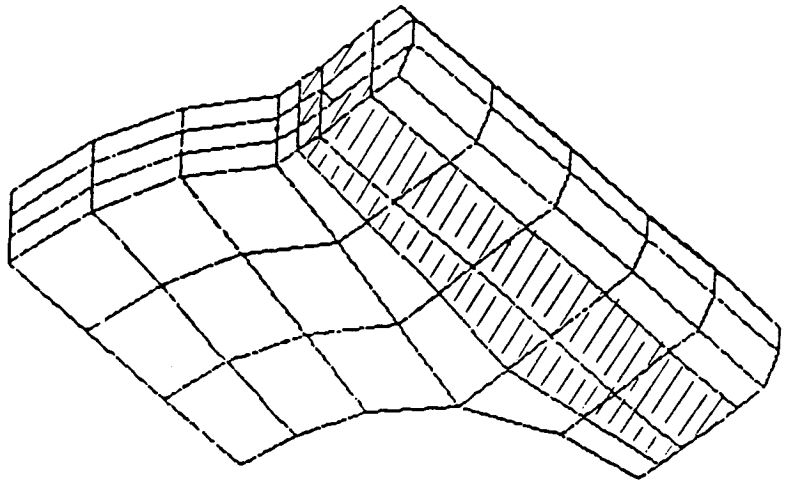

Figure 5.5 Boundary layer for design parameter 5

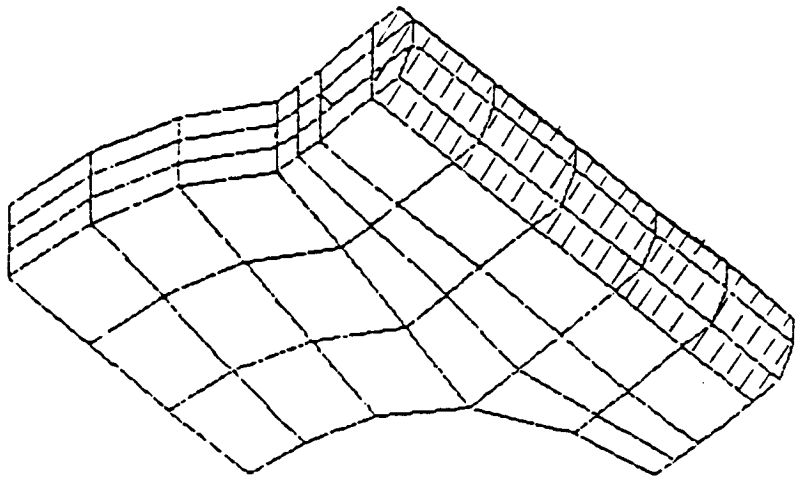

Figure 5.6 Boundary layer for design parameter 6

5.1.1 Stress Design Sensitivity Analysis

Element averaged von-Mises stress [66] is used as the stress constraint for this problem. Since no load variation is involved, Eq. 2.2.42 reduces to

$$\psi' = \iiint_{\Omega} \sum_{i,j=1}^{3} [\sigma^{ij}(z)(\nabla\lambda^{i^T} V_j) + \sigma^{ij}(\lambda)(\nabla z^{i^T} V_j) - \sigma^{ij}(z)\varepsilon^{ij}(\lambda)\ (\text{div } V)]\ d\Omega$$

$$- \iiint_{\Omega} \sum_{i,j=1}^{3} [\sum_{k,\ell=1}^{3} g_{\sigma^{ij}}(z) C^{ijk\ell}(\nabla z^{k^T} V_\ell)] m_p\ d\Omega$$

$$+ \iiint_{\Omega} g(\text{div } V) m_p\ d\Omega - \psi \cdot \iiint_{\Omega} (\text{div } V) m_p\ d\Omega \qquad (5.1.1)$$

Due to symmetry of the structure, only 53 (out of 82) elements need to be tested to verify accuracy of von-Mises stress sensitivity analysis.

5.1.2 Results and Discussion

Shape design sensitivity analysis is performed for each parameter and is checked with a 1% perturbation. Results of shape design sensitivity are given in Tables 5.1-5.6.

In each table, the first column indicates the element number, the second column is the element averaged von-Mises stress ψ^1 for the initial design, the third column is the von-Mises stress ψ^2 for the perturbed design, the fourth column is the finite difference $\Delta\psi = \psi^2 - \psi^1$, and the fifth column is the predicted stress change ψ'. The

sixth column shows the comparison between finite difference $\Delta\psi$ and predicted change ψ', with 100 as complete agreement. That is, any measure lower than 100 means under predicting and any measure higher than 100 means over predicting. To analyze sensitivity accuracy systematically, a grading system is adopted. The grade system is listed in Table 5.7. The grade system is used to examine the general performance of the design sensitivity analysis results of Tables 5.1-5.6. A summary of this analysis is presented in Table 5.8.

It is important to note that accuracy of sensitivity analysis depends on the accuracy of finite element analysis. On the one hand, the sensitivity ψ' may deviate from $\Delta\psi$ if the design perturbation δb is so large that nonlinearity becomes significant. On the other hand, $\Delta\psi$ may be too small and results in errors because of losing significant digits if δb is too small. Furthermore, in the ANSYS data entry stage, only a limited number of digits can be used, this will cause minor numerical errors in computing the finite difference result $\Delta\psi$. Numerical experiments show that sensitivity analysis generally agrees well when $\Delta\psi$ is between 1% to 5% of ψ^1. Therefore, this accuracy comparison is used to measure global performance of the shape design sensitivity analysis method presented.

The last row of Table 5.8 shows the overall averaged percentage of each grade. On average, 87.33% (46 out of 53) of the predictions ψ' are between 95% to 105% agreement with the analysis difference $\Delta\psi$ and 94.61% (50 out of 53) of the predictions are between 90% to 110% agreement with $\Delta\psi$. This agreement is considered satisfactory while the

sensitivity obtained from the material derivative is compared with that obtained from forward finite difference. Agreement can be further improved by using the central finite difference [43]. Choi and Twu [67] observed that the sensitivity obtained from central finite difference converges to that obtained from material derivative.

Sensitivity analysis results show that the von-Mises stress criteria is less sensitive with respect to design parameters 1, 2, and 3, since the varying region due to perturbations of these parameters are relatively remote from the stress concentration area surrounding the clamping bolt hole. It is observed that all poor or failed predictions correspond to very small $\Delta\psi$. This includes element 75 in Table 5.2, elements 69 and 80 in Table 5.3, element 62 in Table 5.4, and elements 33, 47, and 48 in Table 5.5.

5.2 Doubly-Curvature Arch Dam

A double-curvature arch dam similar to that studied by Wassermann [7], is treated here using higher order finite element approximation and continuum shape design sensitivity analysis discussed in Chapter 2. A picture of an actual arch dam is shown in Fig. 5.7 [68]. Conventionally, an arch dam design is defined by its contour plan and crown cross section, as shown in Fig. 5.8 [68].

substantial literature deals with shape optimization of gravity dams [2,5,16,30,38,69]. For a three dimensional arch dam, Rajan [70] optimized dam shape using membrane shell theory. Mohr [71] used the same approach. Sharp [72] used thin shell theory to optimize a double

ORIGINAL PAGE IS
OF POOR QUALITY

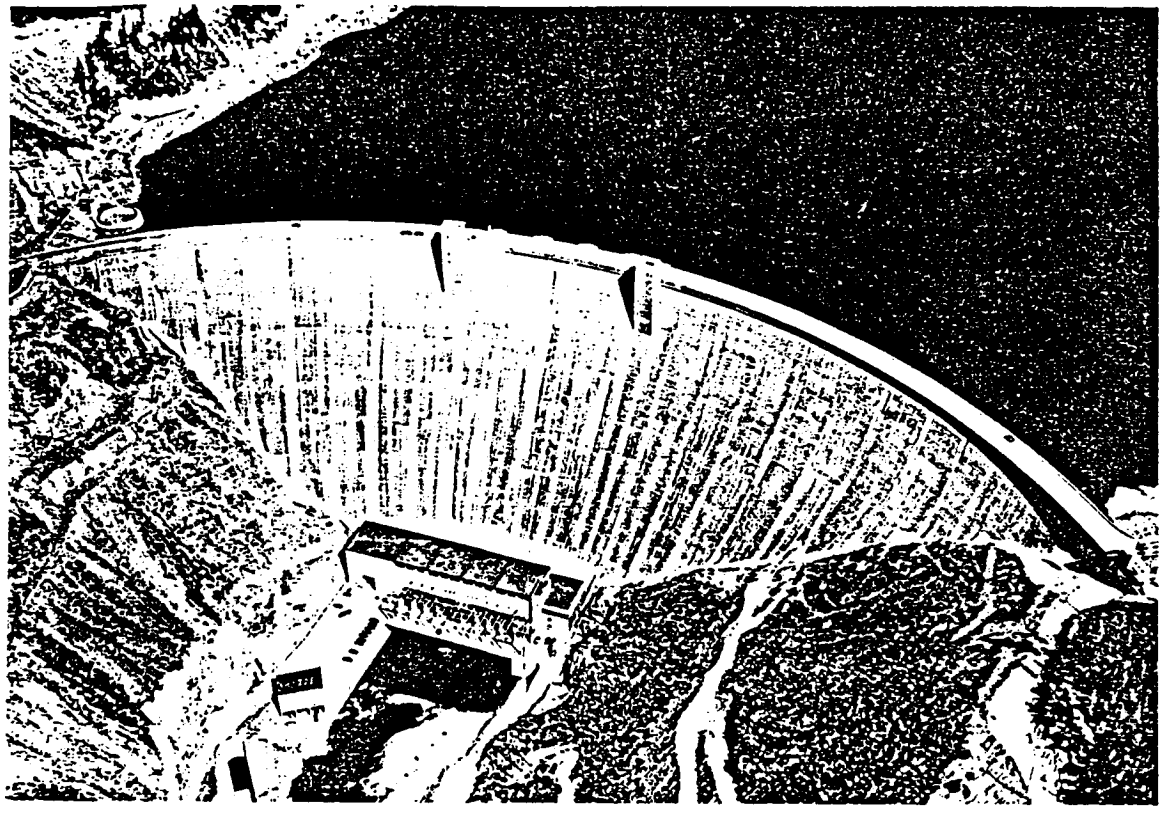

Figure 5.7 Doubly-curvatured arch dam

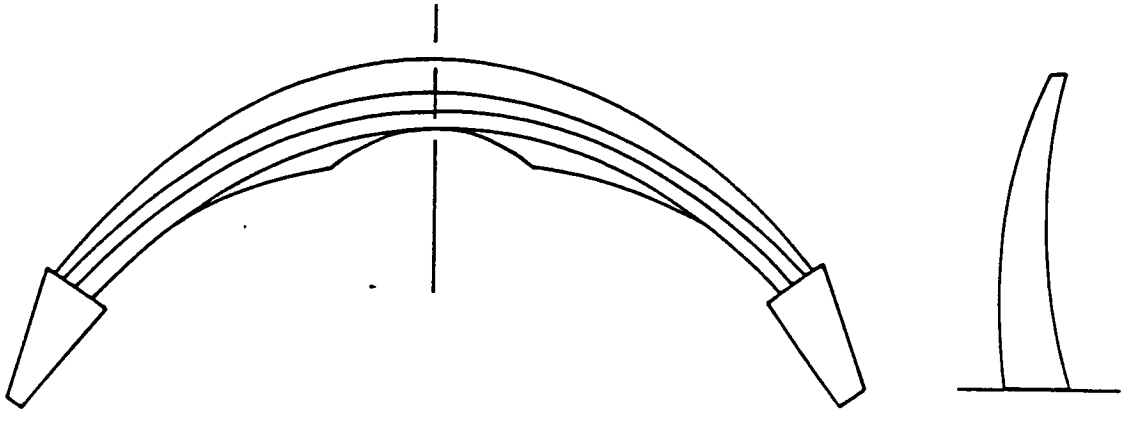

(a) Contour (b) Crown cross-section

Figure 5.8 Contour plan and crown cross section of an arch dam

curvature arch dam, but experienced difficulties in completely satisfying tension limits within the structure. Wassermann [7] used 8 node solid finite elements to optimize a double-curvature arch dam, with position and tangent vectors as design variables, and solved the optimization problem by sequential linear programming. Foundation interaction was considered in Ref. 7. Wang, Sun, and Gallager [9] presented shape design sensitivity analysis and optimal design, based on finite element method, with the position of a limited number of master nodes that characterize the surfaces of a set of isoparametric finite element as design parameters.

To simplify the study, without loss of generality, the following assumptions are made in this problem:

1. The structure and loading conditions are assumed to be symmetric with respect to the crown cross section. Thus, only half the span of the arch dam is analyzed.
2. Dam-foundation interaction is not considered. That is, the foundation is assumed to be rigid.
3. Temperature effects are not considered.
4. Gravel concrete is assumed to be homogeneous and behave elastically.

The physical properties involved are gravity acceleration (10. m/sec/sec), water weight density (10. KN/m^3), gravel concrete weight (25. KN/m^3), the concrete elastic modulus(21. GPa), and concrete Poinson's ratio (0.2).

Bezier surfaces are used to parametrize two surfaces of an arch dam (upstream and downstream side). Each side is defined by 16 control points. In this study, the initial shape of an arch dam is assumed to be a gravity dam. A parametric representation of this gravity dam is shown in Fig. 5.9. A series of shape design sensitivity analyses is carried out for this gravity dam. In the optimization phase to be presented in Chapter 6, shape design sensitivity accuracy is tested for a curved arch dam.

The x_2-coordinates of 32 control points are selected as design parameters. The dam finite element model is uniformly divided by 6x6 meshes in the x_1-x_3 plane, while there is only one layer in the x_2 direction. It contains a total of 36 20-node isoparametric solid elements and 315 nodes with 726 active degrees-of-freedom (Fig. 5.10).

Due to simplicity of the finite element model and design parameters selected, it is unnecessary to apply the boundary displacement method to generate domain velocity fields. The entire structure is a boundary layer, since there is only one layer of elements defined in the x_2-direction. The global control nature of Bezier surfaces force all elements to move in response to any control point perturbation. Boundary velocity fields can be determined by surface perturbations, while domain velocity fields can be obtained by using displacement shape functions.

In the ANSYS finite element code, the linear water pressure profile is treated as a ramped profile (see Figs. 5.11 and 5.12). Also, continuous self weight of the concrete dam is treated as discretized

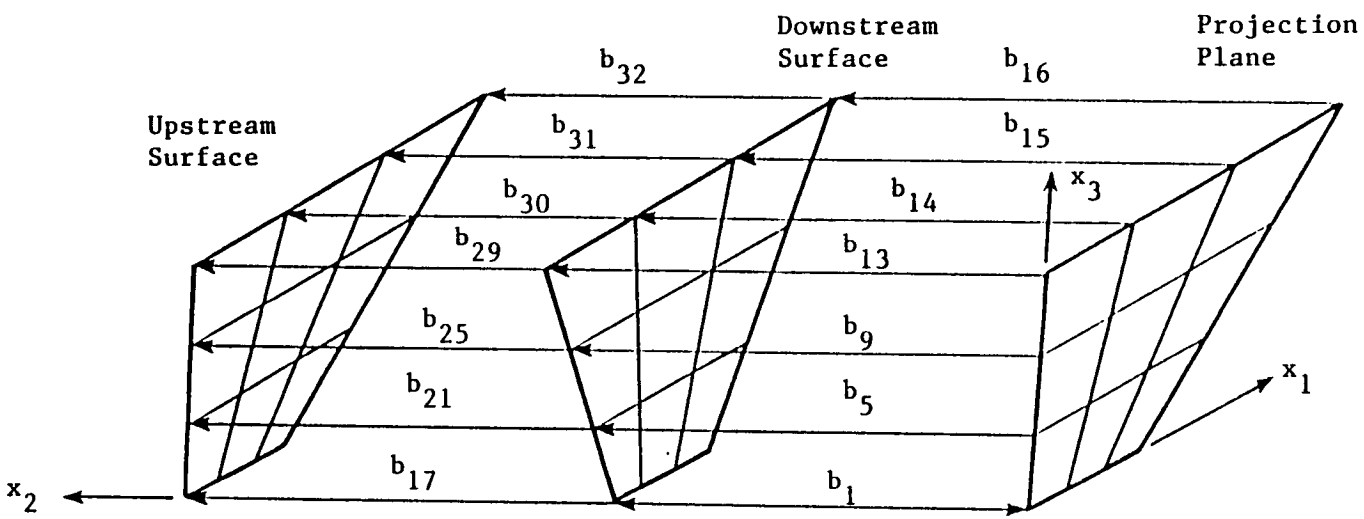

Figure 5.9 Parametric representation of a dam

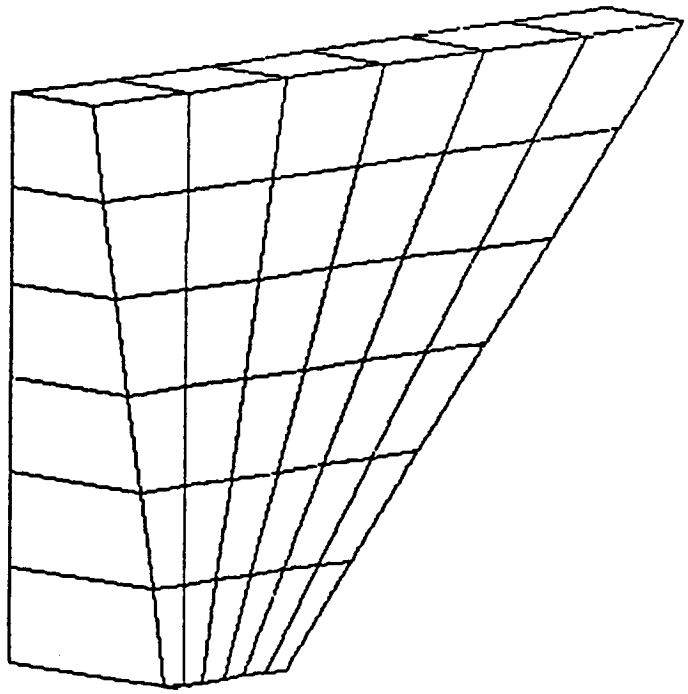

Figure 5.10 Finite element model of dam

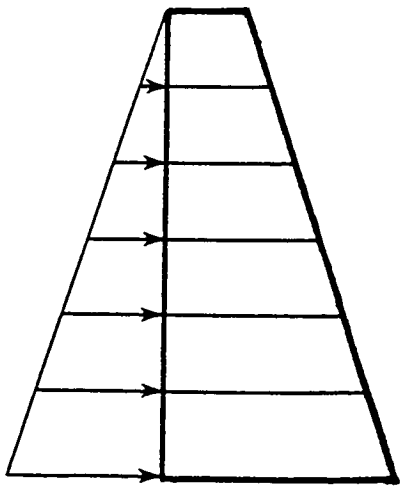

Figure 5.11 A profile of water pressure

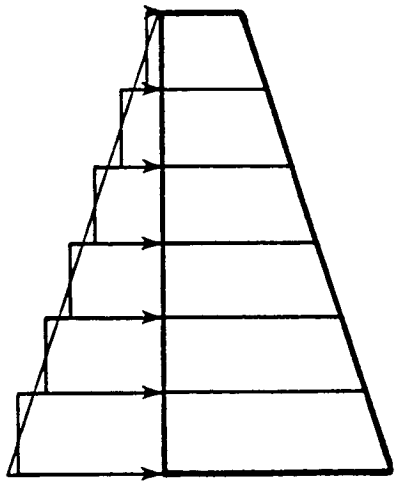

Figure 5.12 A profile of approximated water pressure

nodal forces. Numerical tests involving these two approximations are discussed in the next two sections.

5.2.1 Material Derivative of Load Linear Form of Body Force

In Eq. 2.2.20, the material derivative of the load linear form for body force is given by the first and second terms on the right. For self-weight body force, these two terms reduce to just one term. That is, if $f^i = rg^i$, where r is mass density. g^i is the i-th component of the gravitational acceleration vector. Since both r and g are assumed constant, the first term on the right of Eq. 2.2.20 vanishes. Thus, the only term left is

$$\ell'(\lambda) = \iiint_{\Omega} \sum_{i=1}^{3} f^i \lambda^i (\text{div } V)\, d\Omega \tag{5.2.1}$$

Numerical evaluation of Eq. 5.2.1 is simple, since f is constant.

Self-weight must be converted to equivalent nodal forces in finite element analysis. Usually this is done by forming a mass matrix to determine equivalent nodal forces. In the ANSYS finite element code, a simple lumped mass matrix is adopted, instead of a consistent mass matrix. The lumped mass matrix is used to construct the nodal gravity force. The lumped mass matrix derived from certain shape functions [73,74,75] was originally introduced for eigenvalue analysis. Clough [76] proved that this type of mass lumping method will lead to solution convergence. In the ANSYS finite element code, lumped masser for a three dimensional elastic solid are constructed in such a manner that

all corner nodes assume 1/40 of the total mass of the element, while each edge node assumes 1/15 of the total mass [77]. In discretized form, the nodal gravity force is

$$F_n^i = rg^i \, Vol/C_n \equiv rg^i \iiint_{\Omega_e} d\Omega/C_n \tag{5.2.2}$$

where Vol and C_n denote the volume of element Ω_e and the mass distribution coefficient, respectively.

The load linear form variation, due to body force variation, can be written in discrete form as

$$[\sum_{n=1}^{N} (\sum_{i=1}^{3} F^i \bar{z}_n^i)]' = \sum_{n=1}^{N} \sum_{i=1}^{3} (\dot{F}_n^i \bar{z}_n^i + F_n^i \dot{\bar{z}}_n^i) \tag{5.2.3}$$

where F_n^i denotes the i-th component of the nodal force of node n, $\bar{z}_n^i$ is the i-th component of virtual displacement of node n, and N is the number of total nodes in each element. Using the fact that $\dot{\bar{z}} = 0$, the second term on right side of Eq. 5.2.3 vanishes. When evaluated at $\bar{z} = \lambda$, the right side Eq. 5.2.3 becomes (see Eqs. 2.2.28 and 2.2.41)

$$\ell'(\lambda) = \sum_{n=1}^{N} \sum_{i=1}^{3} \dot{F}_n^i \lambda_n^i \tag{5.2.4}$$

The variation of nodal body force is linearly proportional to the volume change of an element. That is, from Eq. 5.2.2,

$$\dot{F}_n^i = rg^i \iiint_{\Omega_e} (\text{div } V) \, d\Omega/C_n \tag{5.2.5}$$

Therefore, the material derivative of the load linear form for self-weight can be evaluated either in continuum form or in discrete form. Numerical experiments show that results obtained from both approaches are very close to each other (within 4% error). This observation confirms the validity of the mass lumping method.

5.2.2 Material Derivative of Load Linear Form of Surface Traction

For surface traction due to hydrostatic water pressure, the material derivative of the load linear form can be derived in the following manner. Let

$$T^i = p(x)\ n^i(x) \tag{5.2.6}$$

where T^i is the i-th component of traction force, $n^i(x)$ is the external unit normal vector on the boundary, and $p(x)$ is the pressure distribution. Using Eq. 2.2.20, the material derivative of the load linear form, due to water pressure, can be obtained as

$$\ell'(\lambda) = \iint_\Gamma \left[(\nabla p^T V)(n^T\lambda) + p(n^T\lambda)(\text{div } V) - p\lambda^T(DV^T n)\right] d\Gamma \tag{5.2.7}$$

A numerical experiment is carried out to compare sensitivity computations based on linear and ramped water pressure. It is observed that sensitivity results obtained for two pressure loadings agree with each other to within 3%. This observation confirms that the ramped water pressure assumption is valid. The design sensitivity expression

for pointwise principal stress is obtained by substituting Eqs. 5.2.1 and 5.2.7 into Eq. 2.2.45.

5.2.3 Results and Discussion

Shape design sensitivity computation of the principal stress at Gaussian points on both upstream and downstream faces is carried out in this section. Derivation of three dimensional principal stress can be found in Ref. 66. Since the main purpose here is to demonstrate feasibility of method proposed, only the first principal stress at one Gaussian point on the upstream surface of each finite element is investigated and reported. Results are given in Tables 5.9-5.16. Eight out of 32 design parameters are perturbed by one meter each. These are parameter 1, 6, 8, and 13 on the downstream surface and 17, 23, 29, and 32 on the upstream surface defined in Fig. 5.11.

The grading scheme of Table 5.7 is also used here to assist in accuracy analysis. Results are listed in Table 5.17. The last row of Table 5.17 shows that, over eight cases studied, 90.63% (33 out of 36) of predictions ψ' are within 5% of $\Delta\psi$, and 94.1% (34 out of 36) are within 10% of $\Delta\psi$. The prediction failure rate is slightly higher than that for the engine bearing cap. Most of the predictions graded below c are associated with small $\Delta\psi$. This includes elements 13 and 14 in Table 5.9, elements 25 and 27 in Table 5.11, elements 29, 32, and 34 in Table 5.12, elements 12 and 22 in Table 5.14, and element 36 in Table 5.16. The finite difference $\Delta\psi$ for element 27 in Table 5.11 is 3% of ψ^1, which is not small. This peculiar case seems to occur in a region of stress

transition. It is possible that the finite element model is not fine enough to reflect this stress state. The body force and water pressure approximations may play certain roles in this inaccuracy problem. However, the overall performance of the shape design sensitivity analysis method is consistently good. It is also noteworthy to see the accuracy achieved in this case, even when approximation methods such as lumped mass and ramped pressure are used. To achieve better comparisons, the central difference scheme can be applied to compute finite differences.

5.3 Total Hip Joint Reconstruction

In a recent publication, Vichnin and Batterman [78] pointed out that "the number of total number of hip replacements implanted in humans has reached over 100,000 per year, which demonstrates the need for optimum design of these devices to maximize their service life, and design of prothesis implants can be greatly enhanced by applying sophisticated structural engineering techniques to the pertinent biomechanics problems." Conventry [79] reviewed and presented a historic perspective and the present status of total hip arthroplasty. His study revealed developments in the state-of-the-art of orthopedic surgery. The earliest surgery was done by Barton [80] in 1826. In the past are hundred fifty years, hip surgery has relied on human imagination and trial-and-error, with most cases failind. In accounting for difficulties regarding human joint replacement, Smyth [81] said it best in his statement; "the complete solution to the problem of

arthroplasty will be found only when we can provide our patients with new hips either made of, or be able to unite with living bone." However, before the complete solution is reached, the structural behavior of hip joints should be fully understood. A schematic figure of a total hip joint reconstruction is given in Fig. 5.13.

Finite element stress analysis was first introduced in orthopedic literature by Brekelmans et al. in 1972 [82]. Since then, many works have contributed to analyzing bone and implant structures, using finite element analysis. These works lead to deeper physical insight to structural performance of human skeletal parts and implant interactions. Huiskes and Chao [83] conducted a survey of applications of finite element analysis in orthopedic biomechanics. Gallager et al. [84] contributed a textbook, Finite Elements In Biomechanics.

Other than biological factors, the complexity of total hip joint reconstruction is aggravated by bone/cement/implant interactions. The problem of total hip design optimization is not limited in implant strength and geometry, or to cement properties and thickness. The ultimate goal is to 'reconstruct' a living hip. The structural performance (stress state) of a hip joint and bone must be reinstated as closely as possible to the real hip joint, in order to resume normal life duties. In attempting to construct a hip joint with an implant and cement, it is very important to establish a pertinent design criteria.

Crowningshield et al. [85] observed that clinical experience with total hip reconstruction has been characterized by a variety of mechanical problems, dislocation, wear, component fracture, and

ORIGINAL PAGE IS
OF POOR QUALITY

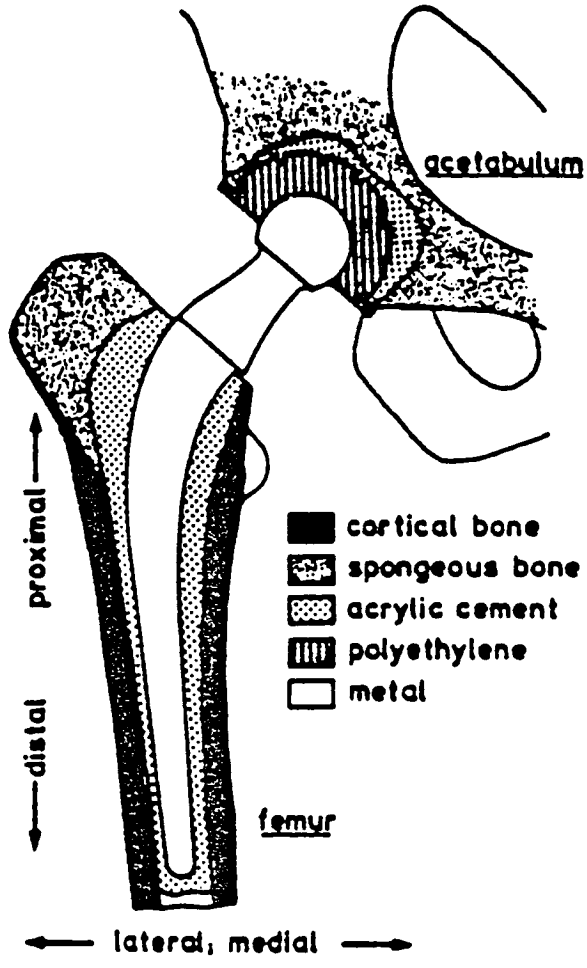

Figure 5.13 Total hip joint reconstruction

component loosening [85]. The long-term success of total hip arthroplasty is presently more limited by mechanical failures than by biological problems. Most of the failure modes cited can be related to cement thickness and strength (Young's modulus).

Considering cement as the media that is interfaced between the metal implant and bone, from the point view of the material interface problem investigated by Sih et al. [86], the cement will perform much better if its properties can be designed as a compromise between implant and bone. Unfortunately, current technology can only produce cement with Young's modulus almost ten times lower than that of bone, and one hundred times lower than that of a metal implant. Facing this reality, Kwak et al. [87] investigated the effect of cement thickness on the stress state of the cement and metal implant by a two dimensional finite element analysis. Crowningshield et al. [85] studied the effect of femoral stem cross-sectional geometry on cement stresses in total hip reconstruction in a three dimensional finite element analysis. Crowningshield et al. [88] studied the function of an implant collar, use of Titanium in femoral protheses, and design analysis of bone cements [89].

The current limitation on the cement material strength suggests that it might be a better strategy to design an implant with material properties closer to a real bone, in order to create better interface stress condition. However, without a systematic design sensitivity analysis, design optimization of total hip joint reconstruction is far from reality. The first systematic analysis of cement property design

C-2

sensitivity analysis for implant design, based on a strain energy density failure criteria, in Refs. 90 and 91 was presented by Yang et al. [92].

The major engineering problems relating to total hip joint optimal design may be summarized as follows:

1. Design failure criteria for implant, cement, and bone: For the implant, possible failure criteria can be von-Mises equivalent stress octahedral shearing stress, as was pointed out in Ref. 93. Since most stems are built by ductile material, failure will most likely occur due to shear stresses. However, for fatigue failure, principal stress is considered as a failure criteria. In this work, principal stress will be considered as the failure criteria for the stem. For cement, a relatively brittle material, failure is most likely related to dilatation stresses; i.e., principal stresses. However, for cement cracks due to manufacturing defects or implanting errors, strain energy density [91] is considered as the fracture criteria. Therefore, strain energy density is considered here as the failure criteria for cement. Sih et al. [90] pointed out that in most cases of loosening, the cement-bone interface was involved more often than the cement-implant interface. Failure was attributed mostly to the gross differences in modulus of the bone and cement, over a very short distance, resulting in sharp stress gradients. This is generally thought to be the cause of bone resorption and consequent loosening. For the bone, Lindahl and Lindgren [94,95] studied the tensile and compressive rupture

strength of human cortical bone. Vichnin and Batterman [78] used the failure criteria for anisotropic material established by Tsai and Wu [96] in stress analysis and failure prediction in the proximal femur, before and after total hip replacement. The principal stress is considered as the failure criteria for bone in this work.

2. Geometric modeling: Construction of a finite element model of the proximal femur is an instrumental but very expensive step. Crowningshield and Wilson [89] used cat scan images to generate a finite element model of a cadaver femur with an implanted trial HD-2 prothesis. It is necessary to generate such a geometric model, case by case, to study individual hip joint performance. The geometry of the prothesis and the cement thickness are design parameters to be considered.
3. Reinstate stress state of original hip joint in the totally reconstructed hip joint: Once the real hip joint is injured, it is almost impossible to determine the original stress state in the bone. However, an artificial stress state can be obtained from the finite element model, with loading conditions determined through biomechanical study [97,98]. In the optimization process, this stress state may be imposed as a side constraint, to simulate the structural behavior of real bone. In addition to this complicated process, different loadings must also be considered. Without this consideration, the reconstructed hip joint may be too stiff in one region, but too soft in an other region [65]. Failure will occur

most likely in those regions of abrupt discontinuity of flexural rigidity.

From this study, it is clear that design optimization for total hip joint reconstruction can be achieved only through a systematic approach. Due to current limitations in cement properties, a true optimal design may not exist. However, a near-optimum can still be obtained, through geometry arrangement of the implant and cement thickness.

5.3.1 Shape Design Sensitivity Analysis

To tackle such a complicated problem, a feasibility study is conducted here, based on the shape design sensitivity analysis method discussed in Chapter 2 and related numerical methods, to investigate the geometric influence of implant and cement thickness on stress distribution in bone, cement, and stem. The principal stress is used as a design failure criteria for the metal stem and bone, while strain energy density is considered as a design failure criteria for cement. The material properties of all parts are listed below:

Material	Young's modulus	Poinson ratio
Stem	207. GPa	0.3
Cement	2.07 GPa	0.23
Compact Bone	14.0 GPa	0.3

Several assumptions were made to simplify this work, without sacrificing much information. A prototype femur model is simplified from the cadaver femur model of Ref. 89 as the piecewise linear conical solid shown in Fig. 5.14. For simplicity, structural and loading symmetry are assumed. Therefore, only half of the model is constructed. The finite element model consists of 16 elements for the metal stem (Fig. 5.15), 28 elements for the cement (Fig. 5.16), and 36 elements for the bone (Fig. 5.17). The model has 525 nodes and 1335 active degrees-of-freedom. The model is assumed to be fixed in the distal end of the bone. Referring to the studies of Refs. 85 and 87, a 4000 N vertical force is applied at the tip of the stem. This force is roughly equivalent to the gate force generated by a 70 Kg person.

Sixteen design parameters are selected. The first eight parameters are the radius of the stem at different locations, as shown in Fig. 5.18, while the last eight parameters are the radius of the bone-cement interface. Cement thickness at different locations is determined by subtracting the radius of stem from the radius of the bone-cement interface. Each design parameter is perturbed by 5%, to obtain the associated design velocity field. To allow a local shape change, perturbation of each design parameter will influence only the neighboring two layers of elements. For example, perturbation of r_3 will lead to a shape change in only 12 surrounding elements and perturbation of r_{11} will lead to shape change in 16 elements. There are four groups of stress functionals on which shape design sensitivity analysis is carried out. For simplicity, shape design sensitivity

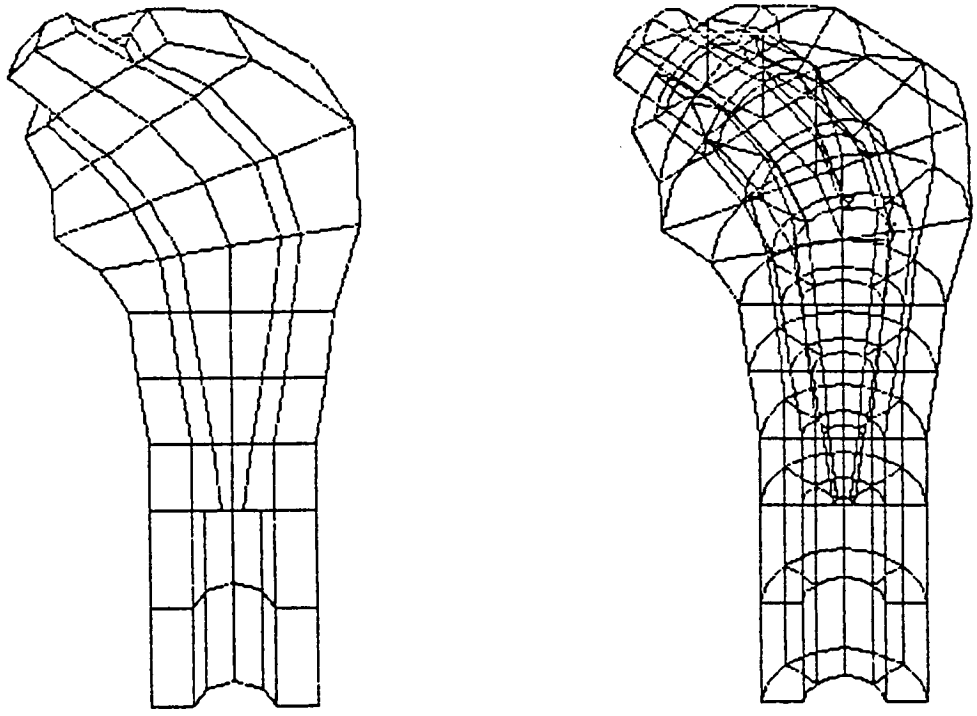

(a) Hidden lines removed (b) With hidden lines

Figure 5.14 Finite element model of hip joint reconstruction

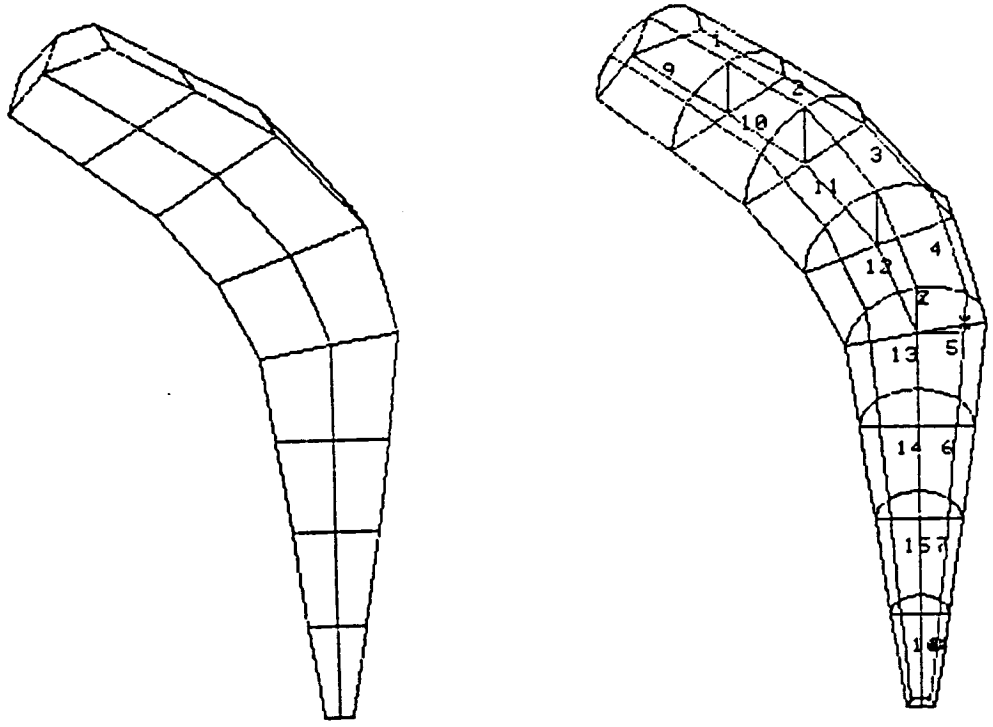

(a) Hidden lines removed (b) With hidden lines

Figure 5.15 Finite element model of stem

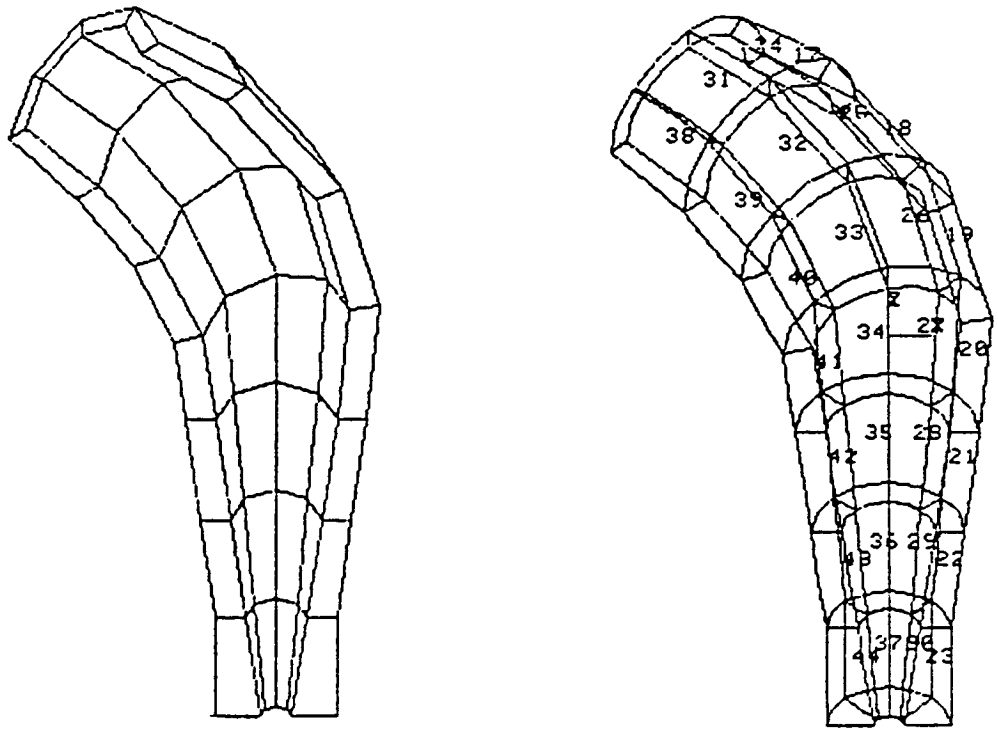

(a) Hidden lines removed (b) With hidden lines

Figure 5.16 Finite element model of cement

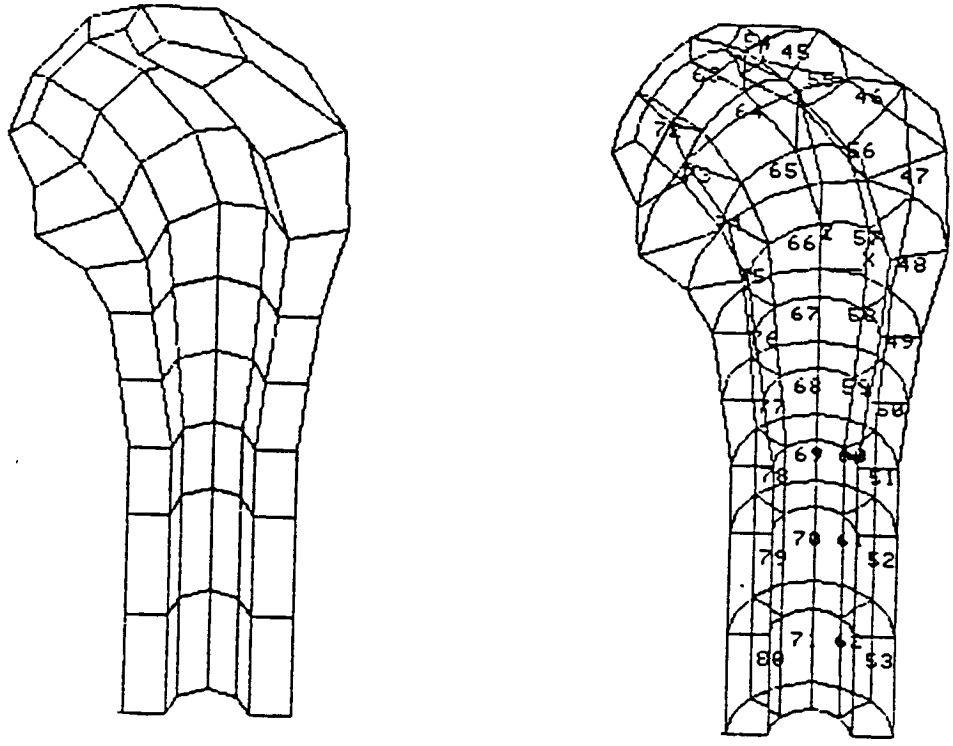

(a) Hidden lines removed (b) With hidden lines

Figure 5.17 Finite element model of bone

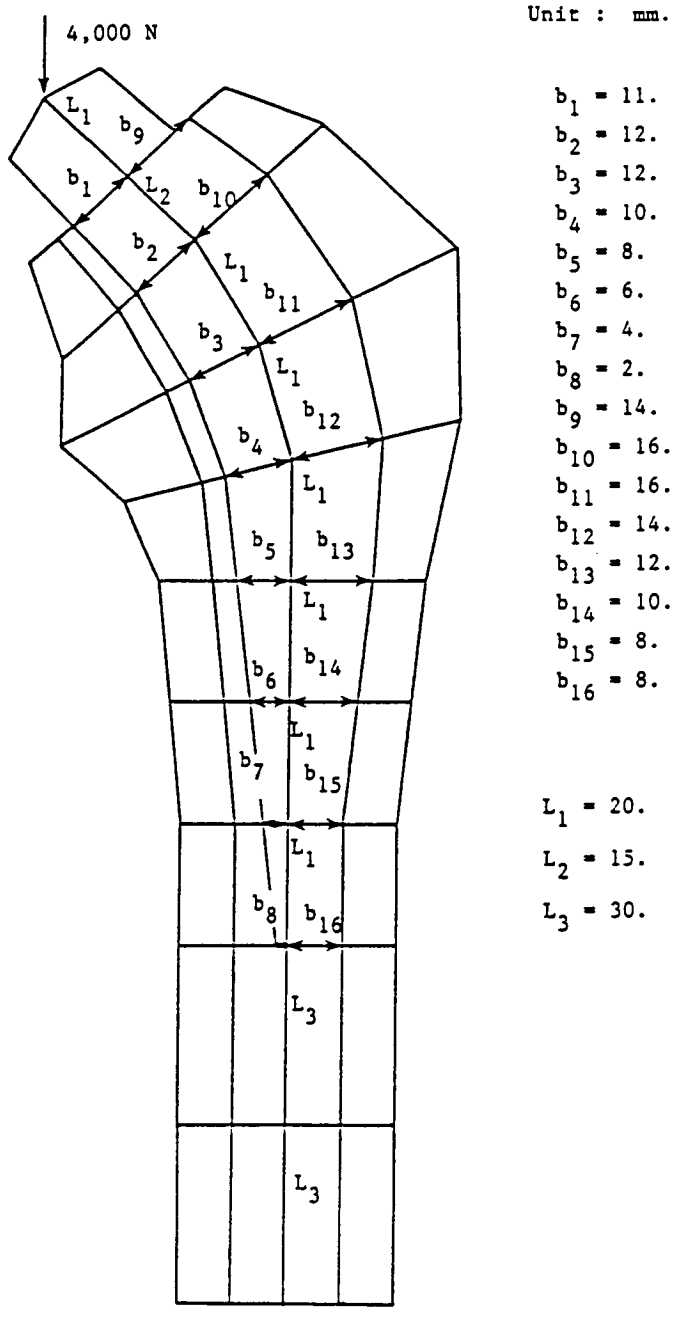

Figure 5.18 Shape design parameters of hip joint

results are reported for perturbation of three (out of 16) design parameters in each group. Results are presented in Tables 5.18-5.29. The central finite difference method is applied to evaluate accuracy of the constraint gradient.

Group 1: Stem principal stress at stem-cement interface (Tables 5.18-5.20).

Group 2: Cement strain energy density at stem-cement interface (Tables 5.21-5.23).

Group 3: Cement strain energy density at bone-cement interface (Tables 5.24-5.26).

Group 4: Bone principal stress at bone-cement interface (Tables 5.27-5.29).

5.3.2 Results and Discussion

Equation 2.2.45 is used to evaluate pointwise shape design sensitivity of principal stress and strain energy density. Since geometry of this prototype model is different from any real femoral model, the stress state obtained in this analysis may be used only for comparison purposes. The grading system used in previous sections for accuracy of sensitivity analysis is used here. Results are shown in Table 5.30.

Remarkable agreement is achieved between constraint gradients obtained from the material derivative and central finite difference. Less accurate results only appear in Table 5.26. In this particular

case, different perturbations of design are tested, but all lead to similar results. This pitfall may be attributed to the locally nonlinear nature of this interface problem and the small sensitivity values reported in Table 5.3.9.

Table 5.1 SDSA result of cap ($\delta b_1 = 0.01\ b_1$)

Element No.	$\psi^1(b)$	$\psi^2(b+\delta b)$	$\Delta\psi$	ψ'	$\psi'/\Delta\psi$ %
1	9829.4564	9828.5147	-0.9417	-1.0018	106.38
2	9631.2028	9628.0146	-3.1882	-3.3138	103.94
4	10620.3320	10608.8240	-11.5080	-11.8711	103.16
5	11444.4800	11434.0660	-10.4140	-10.7471	103.20
7	13584.5710	13571.7170	-12.8540	-13.2538	103.11
8	13641.4950	13628.8460	-12.6490	-13.0425	103.11
10	17933.5910	17925.6160	-7.9750	-8.2273	103.16
11	18498.6300	18490.9490	-7.6810	-7.9352	103.31
13	21202.2630	21201.5970	-0.6660	-0.7012	105.29
14	34270.5140	34269.2430	-1.2710	-1.3343	104.98
16	8367.4820	8371.7067	4.2247	4.3239	102.35
18	9686.1116	9676.9415	-9.1701	-9.4531	103.09
20	12670.2480	12662.7390	-7.5090	-7.7352	103.01
22	16248.4050	16245.1790	-3.2260	-3.3429	103.62
24	30901.3690	30904.1690	2.8000	2.8219	100.78
26	7311.4083	7318.5419	7.1336	7.3411	102.91
27	6857.7422	6866.6746	8.9324	9.2034	103.03
29	7917.4211	7914.0475	-3.3736	-3.4779	103.09
30	7234.2502	7231.6073	-2.6429	-2.7216	102.98
32	9528.8157	9523.9627	-4.8530	-4.9934	102.89
33	8521.5076	8516.3478	-5.1598	-5.3093	102.90
35	13328.4650	13325.3210	-3.1440	-3.2598	103.68
36	12091.2310	12086.3290	-4.9020	-5.1166	104.38
38	24661.4990	24667.9040	6.4050	6.5416	102.13
39	44231.0680	44236.8710	5.8030	5.7784	99.58
41	7349.5330	7356.6628	7.1298	7.3567	103.18
42	6920.5279	6929.3109	8.7830	9.0593	103.15
44	5998.6512	6000.6752	2.0240	2.0604	101.80
45	5762.5105	5763.5140	1.0035	1.0099	100.64
47	7016.8980	7013.2086	-3.6894	-3.8037	103.10
48	6822.9614	6818.7951	-4.1663	-4.2942	103.07
50	9706.9951	9701.8648	-5.1303	-5.2626	102.58
51	9639.7495	9634.9357	-4.8138	-4.9829	103.51
53	13634.1000	13643.2470	9.1470	9.4251	103.04
54	19874.8650	19883.4050	8.5400	8.7644	102.63
56	6080.3933	6065.7735	-14.6198	-15.0314	102.82
57	6121.4120	6106.7258	-14.6862	-15.1005	102.82
59	5832.8322	5813.2385	-19.5937	-19.9210	101.67
60	6266.5615	6248.8605	-17.7010	-18.0088	101.74
62	7041.7283	7052.1501	10.4218	10.7068	102.73
63	8230.6127	8244.8428	14.2301	14.6050	102.63
65	4816.1908	4797.6675	-18.5233	-18.9947	102.55
66	4787.5653	4771.0819	-16.4834	-16.9027	102.54
68	3537.2024	3509.5537	-27.6487	-28.6517	103.63
69	3692.9881	3667.0216	-25.9665	-26.8463	103.39
71	6541.8233	6536.2666	-5.5567	-5.3987	97.16
72	6643.3182	6641.4923	-1.8259	-1.5290	83.74
74	3872.7605	3873.9019	1.1414	1.1218	98.28
75	3820.6962	3823.0448	2.3486	2.3588	100.43
77	3918.9608	3936.1207	17.1599	16.7092	97.37
78	3932.8001	3946.4754	13.6753	13.2409	96.82
80	6240.3854	6161.1448	-79.2406	-79.4547	100.27
81	6158.4620	6072.4872	-85.9748	-86.2675	100.34

Table 5.2 SDSA result of cap ($\delta b_2 = 0.01\ b_2$)

Element No.	$\psi^1(b)$	$\psi^2(b+\delta b)$	$\Delta\psi$	ψ'	$\psi'/\Delta\psi$ %
1	9829.4561	9827.5820	-1.8742	-1.9203	102.46
2	9631.2031	9626.9561	-4.2469	-4.3210	101.74
4	10620.3320	10607.5225	-12.8100	-12.9861	101.37
5	11444.4805	11432.5967	-11.8830	-12.0486	101.39
7	13584.5713	13569.7412	-14.8300	-15.0273	101.33
8	13641.4951	13626.8564	-14.6390	-14.8348	101.34
10	17933.5918	17922.7813	-10.8100	-10.9519	101.31
11	18498.6309	18488.5039	-10.1260	-10.2604	101.33
13	21202.2637	21200.1563	-2.1070	-2.1312	101.15
14	34270.5156	34267.6211	-2.8910	-2.9270	101.25
16	8367.4824	8371.6221	4.1401	4.1692	100.70
18	9686.1113	9676.4238	-9.6876	-9.8197	101.36
20	12670.2480	12661.2373	-9.0110	-9.1269	101.29
22	16248.4053	16240.7373	-7.6680	-7.7643	101.26
24	30901.3691	30899.0566	-2.3130	-2.3259	100.56
26	7311.4082	7319.2188	7.8103	7.9015	101.17
27	6857.7422	6867.4507	9.7087	9.8343	101.29
29	7917.4209	7914.5054	-2.9156	-2.9584	101.47
30	7234.2500	7232.3486	-1.9015	-1.9270	101.34
32	9528.8154	9523.8018	-5.0142	-5.0787	101.29
33	8521.5078	8517.0449	-4.4629	-4.5210	101.30
35	13328.4648	13320.3066	-8.1580	-8.2630	101.29
36	12091.2314	12081.9531	-9.2780	-9.4238	101.57
38	24661.4980	24662.7266	1.2270	1.2593	102.63
39	44231.0664	44227.4102	-3.6570	-3.7067	101.36
41	7349.5332	7357.8228	8.2897	8.4018	101.35
42	6920.5278	6930.4922	9.9641	10.0993	101.36
44	5998.6514	6001.3735	2.7225	2.7301	100.28
45	5762.5107	5764.3105	1.7999	1.7957	99.77
47	7016.8979	7013.7998	-3.0984	-3.1479	101.60
48	6822.9614	6819.5337	-3.4275	-3.4809	101.56
50	9706.9951	9698.6182	-8.3767	-8.4854	101.30
51	9639.7490	9632.9951	-6.7542	-6.8676	101.68
53	13634.0996	13642.1826	8.0830	8.1758	101.15
54	19874.8652	19886.6172	11.7530	11.8758	101.04
56	6080.3931	6067.9648	-12.4286	-12.5846	101.25
57	6121.4121	6109.1602	-12.2519	-12.4059	101.26
59	5832.8320	5810.8921	-21.9401	-22.1048	100.75
60	6266.5615	6248.0376	-18.5240	-18.6539	100.70
62	7041.7285	7037.5947	-4.1334	-4.1586	100.61
63	8230.6123	8226.6572	-3.9552	-3.9200	99.11
65	4816.1909	4804.4438	-11.7468	-11.8391	100.79
66	4787.5654	4777.2231	-10.3422	-10.4232	100.78
68	3537.2024	3529.2163	-7.9860	-8.2503	103.31
69	3692.9880	3684.0610	-8.9271	-9.1526	102.53
71	6541.8232	6511.0430	-30.7802	-30.7081	99.77
72	6643.3184	6605.9126	-37.4054	-37.3561	99.87
74	3872.7605	3871.6660	-1.0945	-1.1390	104.07
75	3820.6963	3820.5486	-0.1476	-0.1835	124.35
77	3918.9607	3913.3545	-5.6062	-5.8643	104.60
78	3932.8000	3926.5962	-6.2040	-6.4450	103.88
80	6240.3853	6205.8198	-34.5655	-34.5274	99.89
81	6158.4619	6123.2358	-35.2264	-35.1633	99.82

Table 5.3 SDSA result of cap ($\delta b_3 = 0.01\ b_3$)

Element No.	$\psi^1(b)$	$\psi^2(b+\delta b)$	$\Delta\psi$	ψ'	$\psi'/\Delta\psi$ %
1	9829.4561	9825.5273	-3.9292	-4.0076	102.00
2	9631.2031	9624.5986	-6.6039	-6.7090	101.59
4	10620.3320	10604.3408	-15.9910	-16.1877	101.23
5	11444.4805	11428.9648	-15.5150	-15.7111	101.26
7	13584.5713	13564.7061	-19.8650	-20.1043	101.20
8	13641.4951	13621.5488	-19.9460	-20.1870	101.21
10	17933.5918	17914.9961	-18.5950	-18.8183	101.20
11	18498.6309	18482.3672	-16.2620	-16.4566	101.20
13	21202.2637	21197.3320	-4.9310	-4.9862	101.12
14	34270.5156	34264.9531	-5.5610	-5.6229	101.11
16	8367.4824	8371.5762	4.0944	4.1080	100.33
18	9686.1113	9675.1709	-10.9408	-11.0693	101.17
20	12670.2480	12657.9805	-12.2680	-12.4082	101.14
22	16248.4053	16231.7275	-16.6770	-16.8699	101.16
24	30901.3691	30891.0859	-10.2840	-10.3932	101.06
26	7311.4082	7320.8901	9.4816	9.5783	101.02
27	6857.7422	6869.3979	11.6559	11.7886	101.14
29	7917.4209	7915.5781	-1.8432	-1.8627	101.06
30	7234.2500	7234.0503	-0.1999	-0.1951	97.60
32	9528.8154	9524.2793	-4.5362	-4.5813	100.99
33	8521.5078	8519.2793	-2.2284	-2.2479	100.87
35	13328.4648	13313.4756	-14.9890	-15.1629	101.16
36	12091.2314	12078.0068	-13.2240	-13.4191	101.48
38	24661.4980	24655.7090	-5.7900	-5.8771	101.50
39	44231.0664	44216.4844	-14.5820	-14.6867	100.72
41	7349.5332	7360.5088	10.9759	11.1105	101.23
42	6920.5278	6933.3154	12.7876	12.9437	101.22
44	5998.6514	6002.9941	4.3431	4.3626	100.45
45	5762.5107	5766.1030	3.5926	3.6052	100.35
47	7016.8979	7015.6587	-1.2395	-1.2541	101.18
48	6822.9614	6821.6592	-1.3021	-1.3206	101.42
50	9706.9951	9698.9512	-8.0441	-8.1429	101.23
51	9639.7490	9635.4424	-4.3074	-4.3936	102.00
53	13634.0996	13639.1523	5.0520	5.0038	99.05
54	19874.8652	19890.2988	15.4340	15.6328	101.29
56	6080.3931	6072.7539	-7.6394	-7.7092	100.91
57	6121.4121	6113.9985	-7.4135	-7.4844	100.96
59	5832.8320	5821.2344	-11.5977	-11.6574	100.51
60	6266.5615	6258.7642	-7.7975	-7.7942	99.96
62	7041.7285	7013.7329	-27.9954	-28.0377	100.15
63	8230.6123	8198.7266	-31.8861	-31.7483	99.57
65	4816.1909	4813.8467	-2.3441	-2.3284	99.33
66	4787.5654	4785.6367	-1.9285	-1.9140	99.25
68	3537.2024	3539.0366	1.8343	1.6791	91.54
69	3692.9880	3693.5674	0.5792	0.4403	76.02
71	6541.8232	6513.9009	-27.9225	-27.8763	99.83
72	6643.3184	6607.5918	-35.7266	-35.7195	99.98
74	3872.7605	3867.7478	-5.0126	-5.0961	101.67
75	3820.6963	3816.2607	-4.4354	-4.5159	101.81
77	3918.9607	3895.5271	-23.4338	-23.7037	101.15
78	3932.8000	3910.9468	-21.8533	-22.0988	101.12
80	6240.3853	6241.1948	0.8092	1.0177	125.77
81	6158.4619	6161.7666	3.3047	3.5143	106.34

Table 5.4 SDSA result of cap ($\delta b_4 = 0.01\ b_4$)

Element No.	$\psi^1(b)$	$\psi^2(b+\delta b)$	$\Delta\psi$	ψ'	$\psi'/\Delta\psi$ %
1	9829.4561	9810.4717	-18.9851	-19.4508	102.45
2	9631.2031	9610.7295	-20.4731	-21.0685	102.91
4	10620.3320	10587.9111	-32.4210	-33.3971	103.01
5	11444.4805	11407.4258	-37.0540	-37.9746	102.48
7	13584.5713	13559.0742	-25.4970	-26.6974	104.71
8	13641.4951	13619.3652	-22.1300	-23.4074	105.77
10	17933.5918	17918.0254	-15.5650	-16.7295	107.48
11	18498.6309	18419.2637	-79.3670	-81.7017	102.94
13	21202.2637	21150.9668	-51.2960	-51.9958	101.36
14	34270.5156	34156.6523	-113.8600	-114.5121	100.57
16	8367.4824	8375.4043	7.9224	7.9947	100.91
18	9686.1113	9675.7295	-10.3823	-10.8857	104.85
20	12670.2480	12660.3047	-9.9430	-10.4947	105.55
22	16248.4053	16184.9961	-63.4090	-65.4988	103.30
24	30901.3691	30752.9316	-148.4370	-150.1576	101.16
26	7311.4082	7336.8804	25.4722	26.0116	102.12
27	6857.7422	6888.4829	30.7407	31.4542	102.32
29	7917.4209	7926.6357	9.2148	9.2795	100.70
30	7234.2500	7248.9258	14.6758	14.9177	101.65
32	9528.8154	9532.2305	3.4143	3.1926	93.51
33	8521.5078	8534.4688	12.9608	12.8673	99.28
35	13328.4648	13269.6406	-58.8240	-60.4650	102.79
36	12091.2314	11981.8135	-109.4180	-112.4852	102.80
38	24661.4980	24540.0820	-121.4170	-122.7929	101.13
39	44231.0664	43895.4648	-335.6030	-338.8092	100.96
41	7349.5332	7383.2383	33.7054	34.4662	102.26
42	6920.5278	6958.1396	37.6118	38.4753	102.30
44	5998.6514	6016.1729	17.5218	17.6665	100.83
45	5762.5107	5780.8560	18.3455	18.5229	100.97
47	7016.8979	7023.3779	6.4799	6.3809	98.47
48	6822.9614	6831.4014	8.4401	8.2318	97.53
50	9706.9951	9695.8291	-11.1656	-11.3823	101.94
51	9639.7490	9582.1875	-57.5616	-58.8557	102.25
53	13634.0996	13605.0771	-29.0230	-28.3287	97.61
54	19874.8652	19792.4883	-82.3770	-81.2261	98.60
56	6080.3931	6078.3975	-1.9959	-2.0529	102.86
57	6121.4121	6118.0645	-3.3476	-3.5283	105.40
59	5832.8320	5890.1143	57.2822	57.5277	100.43
60	6266.5615	6299.0898	32.5284	32.8157	100.88
62	7041.7285	7040.2134	-1.5150	-1.9730	130.23
63	8230.6123	8232.1367	1.5245	1.5572	102.15
65	4816.1909	4833.2881	17.0975	17.1449	100.28
66	4787.5654	4802.5879	15.0226	15.0032	99.87
68	3537.2024	3524.7373	-12.4651	-14.1661	113.65
69	3692.9880	3681.6091	-11.3789	-12.7450	112.01
71	6541.8232	6555.9077	14.0842	15.1211	107.36
72	6643.3184	6667.5093	24.1911	25.1206	103.84
74	3872.7605	3848.7979	-23.9627	-24.6826	103.00
75	3820.6963	3796.8833	-23.8130	-24.5173	102.96
77	3918.9607	3855.9199	-63.0408	-63.6786	101.01
78	3932.8000	3874.9827	-57.8174	-58.3854	100.98
80	6240.3853	6289.5522	49.1670	50.0093	101.71
81	6158.4619	6211.9331	53.4710	54.2004	101.36

Table 5.5 SDSA result of cap ($\delta b_5 = 0.01\ b_5$)

Element No.	$\psi^1(b)$	$\psi^2(b+\delta b)$	$\Delta\psi$	ψ'	$\psi'/\Delta\psi$ %
1	9829.4561	9802.9561	-26.5004	-27.0010	101.89
2	9631.2031	9595.9111	-35.2916	-35.8374	101.55
4	10620.3320	10546.0557	-74.2760	-74.8574	100.78
5	11444.4805	11367.7676	-76.7120	-77.1947	100.63
7	13584.5713	13510.9492	-73.6220	-74.2111	100.80
8	13641.4951	13570.5430	-70.9520	-71.5026	100.78
10	17933.5918	17879.8633	-53.7270	-54.0194	100.54
11	18498.6309	18389.1309	-109.4990	-110.8678	101.25
13	21202.2637	21148.3887	-53.8740	-54.1483	100.51
14	34270.5156	34156.6602	-113.8550	-114.2009	100.30
16	8367.4824	8388.7510	21.2690	20.8644	98.10
18	9686.1113	9645.8008	-40.3106	-40.7077	100.99
20	12670.2480	12631.4023	-38.8460	-39.0897	100.63
22	16248.4053	16162.7207	-85.6840	-86.8264	101.33
24	30901.3691	30764.2402	-137.1280	-137.8016	100.49
26	7311.4082	7362.9214	51.5132	51.6057	100.18
27	6857.7422	6920.4775	62.7355	63.2072	100.75
29	7917.4209	7919.1987	1.7778	1.6553	93.11
30	7234.2500	7245.0146	10.7644	10.8633	100.92
32	9528.8154	9518.2754	-10.5404	-10.8552	102.99
33	8521.5078	8522.6904	1.1824	0.9209	77.88
35	13328.4648	13252.8418	-75.6230	-76.5759	101.26
36	12091.2314	11975.1992	-116.0320	-118.1623	101.84
38	24661.4980	24560.5371	-100.9610	-101.1912	100.23
39	44231.0664	43939.9414	-291.1280	-292.6463	100.52
41	7349.5332	7411.3936	61.8607	62.3042	100.72
42	6920.5278	6991.7363	71.2084	71.7986	100.83
44	5998.6514	6026.8384	28.1871	27.4530	97.40
45	5762.5107	5788.8179	26.3074	25.5871	97.26
47	7016.8979	7016.3887	-0.5095	-1.1456	224.85
48	6822.9614	6823.3560	0.3944	-0.2967	-75.24
50	9706.9951	9678.2988	-28.6966	-28.9315	100.82
51	9639.7490	9577.1484	-62.6006	-63.6297	101.64
53	13634.0996	13622.2588	-11.8410	-11.2963	95.40
54	19874.8652	19829.2480	-45.6160	-44.8920	98.41
56	6080.3931	6043.3350	-37.0584	-37.8702	102.19
57	6121.4121	6083.5522	-37.8599	-38.7097	102.24
59	5832.8320	5834.4556	1.6236	1.4159	87.21
60	6266.5615	6254.2261	-12.3355	-12.6039	102.18
62	7041.7285	7010.2183	-31.5098	-31.9934	101.53
63	8230.6123	8199.9434	-30.6690	-31.1236	101.48
65	4816.1909	4800.9663	-15.2245	-15.3757	100.99
66	4787.5654	4773.9321	-13.6332	-13.8333	101.47
68	3537.2024	3491.1245	-46.0778	-46.9806	101.96
69	3692.9880	3647.6543	-45.3339	-46.1900	101.89
71	6541.8232	6485.1753	-56.6482	-57.1210	100.83
72	6643.3184	6585.5400	-57.7782	-58.2778	100.86
74	3872.7605	3842.9790	-29.7814	-30.1544	101.25
75	3820.6963	3793.8799	-26.8164	-27.1935	101.41
77	3918.9607	3837.8706	-81.0903	-81.7043	100.76
78	3932.8000	3854.9622	-77.8380	-78.4221	100.75
80	6240.3853	6181.7236	-58.6616	-59.4112	101.28
81	6158.4619	6100.1362	-58.3259	-59.0764	101.29

Table 5.6 SDSA result of cap ($\delta b_6 = 0.01\ b_6$)

Element No.	$\psi^1(b)$	$\psi^2(b+\delta b)$	$\Delta\psi$	ψ'	$\psi'/\Delta\psi$ %
1	9829.4561	9645.1406	-184.3160	-185.0050	100.37
2	9631.2031	9448.7637	-182.4395	-182.9045	100.25
4	10620.3320	10370.8418	-249.4900	-252.2224	101.10
5	11444.4805	11167.7920	-276.6880	-280.2100	101.27
7	13584.5713	13112.6143	-471.9570	-483.5931	102.47
8	13641.4951	13108.0293	-533.4660	-549.7704	103.06
10	17933.5918	17045.9434	-887.6470	-935.5160	105.39
11	18498.6309	17520.9824	-977.6480	-1031.8282	105.54
13	21202.2637	20207.2773	-994.9850	-1051.7924	105.71
14	34270.5156	32365.0469	-1905.4670	-2042.3608	107.18
16	8367.4824	8144.6450	-222.8369	-228.5900	102.58
18	9686.1113	9363.5166	-322.5947	-326.8106	101.31
20	12670.2480	12284.7090	-385.5390	-399.8413	103.71
22	16248.4053	16003.2422	-245.1630	-272.3967	111.11
24	30901.3691	30646.2754	-255.0930	-263.7081	103.38
26	7311.4082	7112.8638	-198.5444	-207.4228	104.47
27	6857.7422	6664.1855	-193.5567	-201.8134	104.27
29	7917.4209	7681.1914	-236.2299	-244.1408	103.35
30	7234.2500	7025.5811	-208.6691	-215.6370	103.34
32	9528.8154	9334.0938	-194.7215	-203.9963	104.76
33	8521.5078	8364.0615	-157.4465	-164.1051	104.23
35	13328.4648	13296.3096	-32.1550	-39.2244	121.99
36	12091.2314	11993.4346	-97.7960	-106.1838	108.58
38	24661.4980	24587.9063	-73.5920	-76.9323	104.54
39	44231.0664	44197.7734	-33.2950	-38.7578	116.41
41	7349.5332	7126.4272	-223.1058	-234.1455	104.95
42	6920.5278	6710.7593	-209.7684	-220.3471	105.04
44	5998.6514	5889.0366	-109.6146	-114.6983	104.64
45	5762.5107	5652.7495	-109.7611	-114.4531	104.27
47	7016.8979	6971.7676	-45.1306	-48.8590	108.26
48	6822.9614	6784.2798	-38.6814	-41.3258	106.84
50	9706.9951	9737.3701	30.3747	29.6068	97.47
51	9639.7490	9622.7080	-17.0413	-19.3617	113.62
53	13634.0996	13557.6035	-76.4960	-80.1318	104.75
54	19874.8652	19808.9277	-65.9380	-70.2234	106.50
56	6080.3931	6092.9956	12.6023	11.4889	91.16
57	6121.4121	6135.0459	13.6338	13.0032	95.37
59	5832.8320	5877.4746	44.6423	46.1051	103.28
60	6266.5615	6292.0049	25.4433	26.2115	103.02
62	7041.7285	6926.6460	-115.0823	-119.1297	103.52
63	8230.6123	8148.9111	-81.7017	-84.3816	103.28
65	4816.1909	4847.5229	31.3322	31.6223	100.93
66	4787.5654	4822.7505	35.1850	35.7694	101.66
68	3537.2024	3529.2158	-7.9867	-7.2879	91.25
69	3692.9880	3685.4299	-7.5582	-6.8735	90.94
71	6541.8232	6422.3330	-119.4903	-123.0419	102.97
72	6643.3184	6532.9399	-110.3782	-113.4852	102.81
74	3872.7605	3894.5361	21.7756	22.1621	101.77
75	3820.6963	3844.7844	24.0882	24.5273	101.82
77	3918.9607	3875.0320	-43.9289	-44.2824	100.80
78	3932.8000	3890.7434	-42.0568	-42.3491	100.69
80	6240.3853	6135.0898	-105.2954	-108.3117	102.86
81	6158.4619	6055.4053	-103.0568	-105.9788	102.84

Table 5.7 Grading system for accuracy of SDSA results

Grade	Measure of accuracy (%)			Remark
A	95 - 100	or	105 - 100	Excellent
B	90 - 95	or	110 - 105	good
C	80 - 90	or	120 - 110	fair
D	60 - 80	or	140 - 120	poor
F	60 below	or	140 above	fail

Table 5.8 Accuracy of cap SDSA results

Design/ Parameter	Grade A	B	C	D	F
1	50	2	1		
2	52			1	
3	50	1		2	
4	47	3	2	1	
5	48	1	1	1	2
6	44	7	2		
Average %	91.51	4.4	1.89	1.57	.63

Table 5.9 SDSA result of dam (δb_1 = 1.)

Element No.	$\psi^1(b)$	$\psi^2(b+\delta b)$	$\Delta\psi$	ψ'	$\psi'/\Delta\psi$ %
1	3284.0591	3320.0749	36.0158	35.6276	98.92
2	3222.6718	3251.5279	28.8561	28.7459	99.62
3	3072.1229	3092.0488	19.9259	20.0038	100.39
4	2833.7039	2846.8793	13.1754	13.3049	100.98
5	2522.0753	2531.0695	8.9942	9.1139	101.33
6	2237.8580	2244.3653	6.5073	6.5990	101.41
7	1391.9795	1402.4054	10.4259	10.9661	105.18
8	1385.6221	1392.1607	6.5386	6.8183	104.28
9	1437.7149	1446.1003	8.3854	8.5148	101.54
10	1630.0650	1642.8852	12.8202	12.8787	100.46
11	2217.7237	2234.8147	17.0910	17.1546	100.37
12	3868.5193	3888.6801	20.1608	20.2647	100.52
13	849.1099	847.8412	-1.2687	-0.8195	64.59
14	896.5193	896.0454	-0.4739	-0.2845	60.03
15	1110.0775	1115.9381	5.8606	5.9530	101.58
16	1568.0970	1580.5570	12.4600	12.5344	100.60
17	2480.5522	2498.2000	17.6478	17.7286	100.46
18	4491.5432	4512.1864	20.6432	20.7636	100.58
19	408.2423	412.3365	4.0942	4.1724	101.91
20	367.1587	369.4237	2.2650	2.3107	102.02
21	605.7484	608.8671	3.1188	3.1852	102.13
22	1179.8964	1190.5477	10.6513	10.7096	100.55
23	2181.3805	2196.7481	15.3676	15.4456	100.51
24	4019.3998	4035.9958	16.5960	16.6916	100.58
25	315.6617	320.6403	4.9786	5.0102	100.64
26	227.6064	229.7064	2.1000	2.1203	100.97
27	162.4746	164.2285	1.7540	1.7871	101.89
28	791.1302	800.5816	9.4513	9.4912	100.42
29	1829.2332	1842.1167	12.8835	12.9302	100.36
30	3007.7604	3018.8957	11.1353	11.1821	100.42
31	432.2839	438.5233	6.2393	6.2369	99.96
32	299.2437	302.1908	2.9471	2.9534	100.21
33	193.7593	195.1672	1.4079	1.4401	102.28
34	762.8365	772.5178	9.6813	9.6989	100.18
35	1691.5086	1701.7312	10.2226	10.2390	100.16
36	2023.5946	2029.8289	6.2343	6.2449	100.17

Table 5.10 SDSA result of dam (δb_6 = 1.)

Element No.	$\psi^1(b)$	$\psi^2(b+\delta b)$	$\Delta\psi$	ψ'	$\psi'/\Delta\psi$ %
1	3284.0591	3312.9618	28.9027	28.0431	97.03
2	3222.6718	3246.0932	23.4214	22.6306	96.62
3	3072.1229	3092.4405	20.3176	19.4847	95.90
4	2833.7039	2855.1223	21.4148	20.5306	95.85
5	2522.0753	2545.9829	23.9076	23.0857	96.56
6	2237.8580	2256.2434	18.3854	17.7859	96.74
7	1391.9795	1473.2713	81.2918	78.1019	96.08
8	1385.6221	1447.4259	61.8038	58.7149	95.00
9	1437.7149	1490.2216	52.5067	48.6731	92.70
10	1630.0650	1689.4299	59.3649	54.6097	91.99
11	2217.7237	2306.5277	88.8040	84.4494	95.10
12	3868.5193	3970.1118	101.5925	99.7862	98.22
13	849.1099	928.4739	79.3639	76.9862	97.00
14	896.5193	980.3655	83.8463	81.8211	97.58
15	1110.0775	1192.9019	82.8244	79.5474	96.04
16	1568.0970	1658.2041	90.1071	85.1996	94.55
17	2480.5522	2594.9092	114.3570	108.7781	95.12
18	4491.5432	4607.8203	116.2771	113.5485	97.65
19	408.2423	444.3692	36.1269	35.9491	99.51
20	367.1587	414.0684	46.9097	46.5383	99.21
21	605.7484	668.1493	62.4009	61.3056	98.24
22	1179.8964	1285.1092	105.2128	100.8139	95.82
23	2181.3805	2307.8314	126.4509	121.5719	96.14
24	4019.3998	4124.5170	105.1172	102.5892	97.60
25	315.6617	332.5270	16.8653	17.0255	100.95
26	227.6064	251.6585	24.0520	24.3484	101.23
27	162.4746	188.6715	26.1969	26.4448	100.95
28	791.1302	884.3773	93.2471	89.7895	96.29
29	1829.2332	1942.4777	113.2445	109.6133	96.79
30	3007.7604	3085.3240	77.5636	75.6940	97.59
31	432.2839	451.1231	18.8392	18.2221	96.72
32	299.2437	322.9086	23.6648	23.2052	98.06
33	193.7593	219.3403	25.5810	25.1103	98.16
34	762.8365	849.1600	86.3236	83.1939	96.37
35	1691.5086	1778.1588	86.6502	83.9812	96.92
36	2023.5946	2065.9436	42.3490	41.2850	97.49

Table 5.11 SDSA result of dam (δb_8 = 1.)

Element No.	$\psi^1(b)$	$\psi^2(b+\delta b)$	$\Delta\psi$	ψ'	$\psi'/\Delta\psi$ %
1	3284.0591	3368.4606	84.4013	82.1666	97.35
2	3222.6718	3305.7711	83.0993	80.9006	97.35
3	3072.1229	3151.2767	79.1538	77.0658	97.36
4	2833.7039	2905.0773	71.3734	69.4902	97.36
5	2522.0753	2579.5546	57.4793	56.0116	97.45
6	2237.8580	2276.4412	38.5832	38.0073	98.51
7	1391.9795	1458.2192	66.2397	64.4983	97.37
8	1385.6221	1452.8173	67.1952	65.4650	97.43
9	1437.7149	1508.7035	70.9886	69.2362	97.53
10	1630.0650	1709.0774	79.0124	76.9683	97.41
11	2217.7237	2299.3133	81.5896	78.7987	96.58
12	3868.5193	3934.0171	65.4978	64.2006	98.02
13	849.1099	891.4919	42.3819	41.2894	97.42
14	896.5193	938.3750	41.8557	40.8448	97.58
15	1110.0775	1154.3651	44.2876	43.5476	98.33
16	1568.0970	1629.1954	61.0984	60.4206	98.89
17	2480.5522	2571.0300	90.4778	87.6175	96.84
18	4491.5432	4566.7587	75.2155	73.9283	98.29
19	408.2423	418.5146	10.2723	10.2500	99.78
20	367.1587	379.0717	11.9130	11.8541	99.51
21	605.7484	617.6857	11.9374	11.9054	99.73
22	1179.8964	1192.2191	12.3227	13.1478	106.70
23	2181.3805	2229.2297	47.8492	47.6531	99.58
24	4019.3998	4106.0654	86.6656	85.3704	98.51
25	315.6617	316.1967	0.5350	0.7631	142.63
26	227.6064	231.3131	3.7067	3.7950	102.38
27	162.4746	168.0447	5.5701	-2.6494	-47.51
28	791.1302	775.6976	-15.4326	-14.6287	94.79
29	1829.2332	1843.2662	14.0330	14.9975	106.87
30	3007.7604	3094.5563	86.7959	85.1310	98.08
31	432.2839	430.2093	-2.0747	-1.8160	87.53
32	299.2437	302.5506	3.3069	3.3256	100.57
33	193.7593	205.0245	11.2652	10.8163	96.02
34	762.8365	745.4213	-17.4151	-16.7573	96.22
35	1691.5086	1710.5108	19.0022	19.2676	101.40
36	2023.5946	2099.8357	76.2411	73.9607	97.01

Table 5.12 SDSA result of dam (δb_{13} = 1.)

Element No.	$\psi^1(b)$	$\psi^2(b+\delta b)$	$\Delta\psi$	ψ'	$\psi'/\Delta\psi$ %
1	3284.0591	3302.7846	18.7255	18.7017	99.87
2	3222.6718	3241.0465	18.3747	18.3490	99.86
3	3072.1229	3089.6849	17.5620	17.5341	99.84
4	2833.7039	2850.0040	16.3001	16.2666	99.79
5	2522.0753	2536.6047	14.5294	14.4982	99.78
6	2237.8580	2249.9478	12.0898	12.0565	99.72
7	1391.9795	1413.1024	21.1229	20.9071	98.98
8	1385.6221	1406.2787	20.6566	20.4545	99.02
9	1437.7149	1457.2281	19.5132	19.3301	99.06
10	1630.0650	1648.1300	18.0650	17.8890	99.03
11	2217.7237	2234.9786	17.2549	17.1019	99.11
12	3868.5193	3886.0853	17.5660	17.4167	99.15
13	849.1099	873.7872	24.6772	24.1049	97.68
14	896.5193	920.7519	24.2327	23.7180	97.88
15	1110.0775	1132.8935	22.8160	22.3780	98.08
16	1568.0970	1588.5071	20.4101	20.0515	98.24
17	2480.5522	2498.1146	17.5624	17.2490	98.22
18	4491.5432	4505.8741	14.3309	13.9972	97.67
19	408.2423	434.4618	26.2195	25.2247	96.21
20	367.1587	389.7231	22.5644	21.7523	96.40
21	605.7484	629.0860	23.3376	22.5478	96.62
22	1179.8964	1198.0929	18.1965	17.6426	96.96
23	2181.3805	2192.5041	11.1236	10.6904	96.11
24	4019.3998	4021.7719	2.3721	1.8901	79.68
25	315.6617	342.8319	27.1703	25.2873	93.07
26	227.6064	247.6939	20.0875	18.6834	93.01
27	162.4746	178.8706	16.3960	15.4120	94.00
28	791.1302	802.7410	11.6108	11.0444	95.12
29	1829.2332	1829.9917	0.7585	0.3253	42.89
30	3007.7604	2997.1849	-10.5755	-11.0729	104.70
31	432.2839	445.8758	13.5919	10.9440	80.52
32	299.2437	306.6395	7.3958	5.5755	75.39
33	193.7593	200.9759	7.2166	6.4887	89.91
34	762.8365	763.4738	0.6373	0.2521	39.56
35	1691.5086	1680.6830	-10.8256	-11.2073	103.53
36	2023.5946	2007.8868	-15.7078	-16.0825	102.39

Table 5.13 SDSA result of dam (δb_{17} = 1.)

Element No.	$\psi^1(b)$	$\psi^2(b+\delta b)$	$\Delta\psi$	ψ'	$\psi'/\Delta\psi$ %
1	3284.0591	3334.3333	50.2742	52.7840	104.99
2	3222.6718	3228.7751	6.1033	7.1940	117.87
3	3072.1229	3063.6641	-8.4588	-7.9612	94.12
4	2833.7039	1818.7867	-14.9172	-14.6364	98.12
5	2522.0753	2504.7272	-17.3481	-17.1898	99.09
6	2237.8580	2221.2152	-16.6428	-16.5708	99.57
7	1391.9795	1454.3840	62.4045	62.5737	100.27
8	1385.6221	1394.7846	9.1625	8.9156	97.31
9	1437.7149	1414.4755	-23.2394	-23.3552	100.50
10	1630.0650	1601.2571	-28.8079	-28.7928	99.95
11	2217.7237	2192.6886	-25.0351	-24.9570	99.69
12	3868.5193	3843.0828	-25.4365	-25.3299	99.58
13	849.1099	892.8145	43.7046	43.4565	99.43
14	896.5193	906.0073	9.4881	9.3537	98.58
15	1110.0775	1095.5022	-14.5753	-14.6561	100.55
16	1568.0970	1544.7465	-23.3505	-23.3685	100.08
17	2480.5522	2456.1186	-24.4336	-24.4172	99.93
18	4491.5432	4466.7743	-24.7689	-24.7409	99.89
19	408.2423	421.5974	13.3551	13.1792	98.68
20	367.1587	370.8441	3.6854	3.6497	99.03
21	605.7484	598.0754	-7.6730	-7.7377	100.84
22	1179.8964	1163.5275	-16.3689	-16.4132	100.27
23	2181.3805	2163.4864	-17.8941	-17.9051	100.06
24	4019.3998	4003.1438	-16.2560	-16.2346	99.87
25	315.6617	318.7416	3.0799	2.9784	96.71
26	227.6064	228.0388	0.4324	0.4101	94.85
27	162.4746	157.7432	-4.7314	-4.7700	100.81
28	791.1302	779.7913	-11.3389	-11.3648	100.23
29	1829.2332	1817.7857	-11.4475	-11.4200	99.76
30	3007.7604	2999.5662	-8.1942	-8.1557	99.53
31	432.2839	430.3953	-1.8886	-1.9175	101.53
32	299.2437	297.4850	-1.7587	-1.7678	100.52
33	193.7593	190.2163	-3.5430	-3.5593	100.46
34	762.8365	755.2437	-7.5927	-7.5804	99.84
35	1691.5086	1685.5902	-5.9184	-5.8917	99.55
36	2023.5946	2021.1511	-2.4435	-2.4265	99.30

Table 5.14 SDSA result of dam (δb_{23} = 1.)

Element No.	$\psi^1(b)$	$\psi^2(b+\delta b)$	$\Delta\psi$	ψ'	$\psi'/\Delta\psi$ %
1	3284.0591	3135.5695	-148.4896	-154.3618	103.95
2	3222.6718	3084.7292	-137.9426	-143.1733	103.79
3	3072.1229	2957.6821	-114.4408	-118.3429	103.41
4	2833.7039	2751.9984	-81.7055	-84.0441	102.86
5	2522.0753	2480.1518	-41.9235	-42.4492	101.25
6	2237.8580	2257.4500	19.5920	20.6115	105.20
7	1391.9795	1247.4827	-144.4968	-150.9704	104.48
8	1385.6221	1255.7599	-129.8622	-135.6612	104.47
9	1437.7149	1313.8211	-123.8938	-127.8412	103.19
10	1630.0650	1470.1988	-159.8662	-162.9114	101.90
11	2217.7237	2016.1471	-201.5766	-204.6921	101.50
12	3868.5193	3857.0477	-11.4716	-6.1475	53.59
13	849.1099	737.7980	-111.7119	-116.8805	104.63
14	896.5193	826.7174	-69.8018	-73.9387	105.93
15	1110.0775	1079.0946	-30.9829	-31.2537	100.87
16	1568.0970	1483.3017	-84.7953	-82.3836	97.16
17	2480.5522	2247.7291	-232.8231	-236.3811	101.53
18	4491.5432	4398.0024	-93.5408	-90.9669	97.25
19	408.2423	348.7635	-59.4788	-61.4816	103.37
20	367.1587	331.6168	-35.5419	-37.3715	105.15
21	605.7484	639.1100	33.3616	34.3902	103.08
22	1179.8964	1179.7407	-0.1557	4.2108	-2704.43
23	2181.3805	2018.9984	-162.3921	-164.5883	101.35
24	4019.3998	3880.9064	-138.4934	-140.5792	101.51
25	315.6617	283.2211	-32.4406	-33.4773	103.20
26	227.6064	208.3753	-19.2311	-20.2386	105.24
27	162.4746	202.7493	40.2747	40.6934	101.04
28	791.1302	807.0017	15.8714	18.0843	113.94
29	1829.2332	1731.7105	-97.5227	-99.9636	102.50
30	3007.7604	2889.7431	-118.0173	-121.8453	103.24
31	432.2839	413.7474	-18.5365	-19.0805	102.93
32	299.2437	282.1978	-17.0460	-17.8278	104.59
33	193.7593	184.6920	-9.0673	-9.8171	108.27
34	762.8365	736.5400	-26.2965	-26.7623	101.77
35	1691.5086	1609.1664	-82.3422	-85.5487	103.89
36	2023.5946	1953.8409	-69.7537	-72.6383	104.14

Table 5.15 SDSA result of dam (δb_{29} = 1.)

Element No.	$\psi^1(b)$	$\psi^2(b+\delta b)$	$\Delta\psi$	ψ'	$\psi'/\Delta\psi$ %
1	3284.0591	3269.8326	-14.2265	-14.1722	99.62
2	3222.6718	3208.6419	-14.0299	-13.9638	99.53
3	3072.1229	3058.5746	-13.5483	-13.4983	99.63
4	2833.7039	2820.9856	-12.7183	-12.6773	99.68
5	2522.0753	2510.5641	-11.5112	-11.4534	99.50
6	2237.8580	2228.1186	-9.7394	-9.7024	99.62
7	1391.9795	1373.2102	-18.7694	-18.6196	99.20
8	1385.6221	1366.9320	-18.6910	-18.5544	99.27
9	1437.7149	1419.2563	-18.4586	-18.3213	99.26
10	1630.0650	1611.8206	-18.2444	-18.1244	99.34
11	2217.7237	2198.9012	-18.8225	-18.7205	99.46
12	3868.5193	3847.8469	-20.6724	-20.5930	99.62
13	849.1099	820.9589	-28.1511	-27.8771	99.03
14	896.5193	867.5844	-28.9349	-28.7314	99.30
15	1110.0775	1081.5093	-28.5682	-28.4323	99.52
16	1568.0970	1540.4713	-27.6257	-27.5366	99.68
17	2480.5522	2453.6955	-26.8567	-26.7663	99.66
18	4491.5432	4464.7821	-26.7611	-26.7084	99.80
19	408.2423	373.1913	-35.0510	-34.6987	98.99
20	367.1587	333.9398	-33.2189	-33.1427	99.77
21	605.7484	566.6782	-39.0701	-39.2005	100.33
22	1179.8964	1143.0712	-36.8252	-38.8642	100.11
23	2181.3805	2150.1219	-31.2586	-31.2804	100.07
24	4019.3998	3995.5021	-23.8977	-24.0101	100.47
25	315.6617	278.3871	-37.2745	-37.2202	99.85
26	227.6064	195.9260	-31.6804	-32.3596	102.14
27	162.4746	128.3625	-34.1121	-38.2132	112.02
28	791.1302	748.5170	-42.6132	-42.9114	100.70
29	1829.2332	1798.8807	-30.3525	-30.4285	100.25
30	3007.7604	2992.6649	-15.0955	-15.3229	101.51
31	432.2839	416.5079	-15.7760	-15.4646	98.03
32	299.2437	291.9762	-7.2675	-8.6271	118.71
33	193.7593	171.8215	-21.9378	-23.6933	108.00
34	762.8365	720.2342	-42.6023	-42.9434	100.80
35	1691.5086	1670.3612	-21.1474	-21.2784	100.62
36	2023.5946	2017.8059	-5.7887	-6.0069	103.77

Table 5.16 SDSA result of dam (δb_{32} = 1.)

Element No.	$\psi^1(b)$	$\psi^2(b+\delta b)$	$\Delta\psi$	ψ'	$\psi'/\Delta\psi$ %
1	3284.0591	3275.4513	-8.6078	-8.6959	101.02
2	3222.6718	3214.1717	-8.5001	-8.5890	101.05
3	3072.1229	3063.8995	-8.2234	-8.3109	101.06
4	2833.7039	2825.9505	-7.7534	-7.8472	101.21
5	2522.0753	2514.9888	-7.0865	-7.1723	101.21
6	2237.8580	2231.7423	-6.1157	-6.1845	101.12
7	1391.9795	1380.5792	-11.4003	-11.5101	100.96
8	1385.6221	1374.1520	-11.4701	-11.5792	100.95
9	1437.7149	1426.0568	-11.6581	-11.7557	100.84
10	1630.0650	1617.9310	-12.1340	-12.2317	100.81
11	2217.7237	2204.2290	-13.4947	-13.6161	100.90
12	3868.5193	3851.5565	-16.9628	-17.0944	100.78
13	849.1099	835.5471	-13.5629	-13.6890	100.93
14	896.5193	882.5012	-14.0181	-14.1468	100.92
15	1110.0775	1095.0504	-15.0271	-15.1760	100.99
16	1568.0970	1551.6555	-16.4415	-16.5949	100.93
17	2480.5522	2461.2607	-19.2915	-19.4332	100.73
18	4491.5432	4460.6189	-30.9243	-31.1457	100.72
19	408.2423	397.1405	-11.1018	-11.1493	100.43
20	367.1587	355.2093	-11.9494	-12.0129	100.53
21	605.7484	590.7295	-15.0189	-15.2004	101.21
22	1179.8964	1165.3049	-14.5915	-14.8192	101.56
23	2181.3805	2166.8058	-14.5747	-14.7992	101.54
24	4019.3998	3980.6537	-38.7461	-39.1072	100.93
25	315.6617	306.7175	-8.9442	-8.9755	100.35
26	227.6064	217.4732	-10.1332	-10.1940	100.60
27	162.4746	155.4734	-7.0012	-7.2312	103.28
28	791.1302	793.9535	2.8233	2.4766	87.72
29	1829.2332	1837.5341	8.3009	8.2133	98.95
30	3007.7604	2980.0079	-27.7525	-27.9210	100.61
31	432.2839	427.6688	-4.6151	-4.6173	100.05
32	299.2437	294.1162	-5.1275	-5.1692	100.81
33	193.7593	196.6867	2.9275	2.6656	91.06
34	762.8365	797.2865	34.4500	34.4914	100.12
35	1691.5086	1730.3873	38.8787	39.8362	102.46
36	2023.5946	2022.8917	-0.7029	0.5933	-84.41

Table 5.17 Accuracy of dam SDSA results

Design/ Parameter	Grade A	B	C	D	F
1	33	1		2	
2	34	2			
3	31	2	1		2
4	31	1	1	1	2
5	34	1	1		
6	32	1	1		2
7	33	1	2		
8	33	1	1		1
Average %	90.63	3.47	2.43	1.04	2.43

Table 5.18 SDSA result of stem principal stress at stem-cement interface ($\delta b_1 = 0.05b_1$)

Element No.	$\psi^1(b-\delta b)$	$\psi^2(b+\delta b)$	$\Delta\psi$	ψ'	$\psi'/\Delta\psi$ %
1	76.900543	56.460739	-18.581640	-18.464475	99.37
2	82.513052	71.708536	-9.822287	-9.813846	99.91
3	58.618491	57.257835	-1.236960	-1.230819	99.50
4	77.667893	76.302438	-1.241323	-1.238894	99.80
5	151.866080	151.558090	-0.279991	-0.279657	99.88
6	234.502410	234.586710	0.076637	0.076255	99.51
7	288.618990	288.704590	0.077818	0.077583	99.70
8	149.935880	149.946440	0.009600	0.009577	99.76
9	22.994747	18.834729	-3.781835	-3.760668	99.44
10	6.502503	6.097777	-0.367932	-0.350528	95.27
11	4.146709	3.847933	-0.271614	-0.272375	100.28
12	6.199352	6.325688	0.114851	0.114270	99.49
13	15.908887	15.899525	-0.008511	-0.008521	100.11
14	23.783558	23.770659	-0.011727	-0.011681	99.61
15	30.590008	30.581954	-0.007322	-0.007299	99.68
16	40.949227	40.947751	-0.001342	-0.001331	99.17

Unit: MPa

$\Delta\psi = (\psi^2 - \psi^1)/2 \cdot \delta b$

Table 5.19 SDSA result of stem principal stress at stem-cement interface ($\delta b_5 = 0.05b_5$)

Element No.	$\psi^1(b-\delta b)$	$\psi^2(b+\delta b)$	$\Delta\psi$	ψ'	$\psi'/\Delta\psi$ %
1	65.766446	65.748964	-0.021853	-0.021895	100.19
2	77.015386	77.247456	0.290088	0.290202	100.04
3	57.489100	58.533230	1.305163	1.305159	100.00
4	73.944425	79.967627	7.529003	7.530086	100.01
5	156.946100	146.276790	-13.336638	-13.393827	100.43
6	233.407340	234.789800	1.728075	1.705936	98.72
7	285.578180	291.585090	7.508638	7.514403	100.08
8	150.215720	149.706140	-0.636975	-0.637301	100.05
9	20.763746	20.758184	-0.006953	-0.006943	99.86
10	6.257279	6.221053	-0.045283	-0.045298	100.03
11	4.077925	3.917879	-0.200058	-0.199643	99.79
12	5.762586	6.736014	1.216785	1.218482	100.14
13	16.901243	15.065383	-2.294825	-2.286102	99.62
14	23.852331	23.712592	-0.174674	-0.174696	100.01
15	30.291377	30.874121	0.728430	0.730542	100.29
16	40.939714	40.951781	0.015084	0.014666	97.23

Unit: MPa

Table 5.20 SDSA result of stem principal stress at stem-cement interface ($\delta b_8 = 0.05b_8$)

Element No.	$\psi^1(b-\delta b)$	$\psi^2(b+\delta b)$	$\Delta\psi$	ψ'	$\psi'/\Delta\psi$ %
1	65.757583	65.758276	0.003465	0.003463	99.95
2	77.135088	77.133116	-0.009860	-0.009862	100.02
3	58.032913	58.027792	-0.025605	-0.025607	100.01
4	77.014860	76.993474	-0.106930	-0.106937	100.01
5	151.738610	151.694650	-0.219800	-0.219769	99.99
6	234.598240	234.482250	-0.579950	-0.579742	99.96
7	286.370770	290.965450	22.973400	22.979219	100.03
8	150.829660	148.795670	-10.169950	-10.196406	100.26
9	20.760696	20.761167	0.002355	0.002355	99.98
10	6.238502	6.239281	0.003892	0.003892	100.01
11	3.993641	3.994909	0.006344	0.006344	100.00
12	6.255428	6.259910	0.022412	0.022407	99.98
13	15.896799	15.912264	0.077325	0.077327	100.00
14	23.770586	23.784222	0.068180	0.068098	99.88
15	30.499641	30.676514	0.884365	0.883237	99.87
16	40.216686	41.617492	7.004030	7.004596	100.01

Unit: MPa

Table 5.21 SDSA result of cement strain energy density at stem-cement interface ($\delta b_1 = 0.05\ b_1$)

Element No.	$\psi^1(b-\delta b)$	$\psi^2(b+\delta b)$	$\Delta\psi$	ψ'	$\psi'/\Delta\psi$ %
17	0.00501710	0.00434328	-0.00061256	-0.00061107	99.76
18	0.00211951	0.00197332	-0.00013290	-0.00013267	99.83
19	0.00233601	0.00224633	-0.00008153	-0.00008139	99.83
20	0.00349835	0.00351514	0.00001527	0.00001515	99.24
21	0.00525030	0.00528217	0.00002897	0.00002886	99.64
22	0.00261951	0.00262687	0.00000668	0.00000666	99.66
23	0.01980252	0.01979047	-0.00001095	-0.00001091	99.63
38	0.00675875	0.00602432	-0.00066767	-0.00066629	99.79
39	0.00350612	0.00318289	-0.00029384	-0.00029304	99.73
40	0.00289551	0.00276485	-0.00011878	-0.00011861	99.85
41	0.00424991	0.00423869	-0.00001021	-0.00001021	100.07
42	0.01239189	0.01236603	-0.00002351	-0.00002343	99.68
43	0.02868796	0.02865501	-0.00002996	-0.00002984	99.62
44	0.03414549	0.03412462	-0.00001897	-0.00001891	99.64

Unit: MJ/m^3

Table 5.22 SDSA result of cement strain energy density at stem-cement interface ($\delta b_5 = 0.05b_5$)

Element No.	$\psi^1(b-\delta b)$	$\psi^2(b+\delta b)$	$\Delta\psi$	ψ'	$\psi'/\Delta\psi$ %
17	0.00472474	0.00466059	-0.00008019	-0.00008093	100.93
18	0.00206189	0.00203854	-0.00002918	-0.00002919	100.03
19	0.00255625	0.00206578	-0.00061309	-0.00061184	99.80
20	0.00357983	0.00346835	-0.00013935	-0.00013818	99.16
21	0.00438117	0.00621061	0.00228680	0.00229353	100.29
22	0.00257028	0.00268748	0.00014649	0.00014779	100.89
23	0.01975664	0.01983003	0.00009173	0.00009166	99.92
38	0.00649566	0.00632877	-0.00020862	-0.00020853	99.96
39	0.00343158	0.00327833	-0.00019156	-0.00019169	100.07
40	0.00314662	0.00255333	-0.00074162	-0.00074045	99.84
41	0.00414777	0.00437858	0.00028850	0.00028905	100.19
42	0.01093986	0.01383089	0.00361379	0.00362191	100.22
43	0.02857753	0.02876526	0.00023466	0.00023552	100.36
44	0.03422610	0.03404059	-0.00023189	-0.00023231	100.18

Unit: MJ/m^3

Table 5.23 SDSA result of cement strain energy density at stem-cement interface ($\delta b_8 = 0.05b_8$)

Element No.	$\psi^1(b-\delta b)$	$\psi^2(b+\delta b)$	$\Delta\psi$	ψ'	$\psi'/\Delta\psi$ %
17	0.00468941	0.00469315	0.00001873	0.00001841	98.27
18	0.00204680	0.00205041	0.00001801	0.00001799	99.86
19	0.00228910	0.00229627	0.00003584	0.00003596	100.34
20	0.00349722	0.00351484	0.00008813	0.00008804	99.91
21	0.00525102	0.00528050	0.00014738	0.00014734	99.97
22	0.00263303	0.00261495	-0.00009037	-0.00009047	100.11
23	0.02014298	0.01945739	-0.00342796	-0.00343035	100.07
38	0.00641032	0.00640710	-0.00001610	-0.00001608	99.89
39	0.00335310	0.00334940	-0.00001849	-0.00001866	100.94
40	0.00283419	0.00283010	-0.00002046	-0.00002029	99.20
41	0.00425130	0.00423715	-0.00007078	-0.00007096	100.24
42	0.01241152	0.01234765	-0.00031935	-0.00031938	100.01
43	0.02914190	0.02820509	-0.00468403	-0.00468479	100.02
44	0.03299114	0.03532570	0.01167283	0.01167284	100.00

Unit: MJ/m^3

Table 5.24 SDSA result of cement strain energy density at bone-cement interface ($\delta n_9 = 0.05b_9$)

Element No.	$\psi^1(b-\delta b)$	$\psi^2(b+\delta b)$	$\Delta\psi$	ψ'	$\psi'/\Delta\psi$ %
17	0.00249100	0.00286470	0.00026692	0.00026504	99.29
18	0.00129556	0.00134685	0.00003664	0.00003615	98.66
19	0.00134053	0.00137318	0.00002332	0.00002303	98.76
20	0.00297331	0.00296529	-0.00000573	-0.00000567	98.96
21	0.00653732	0.00652785	-0.00000677	-0.00000670	98.97
22	0.00619827	0.00619612	-0.00000154	-0.00000153	99.17
23	0.01230117	0.01230232	0.00000082	0.00000081	98.85
38	0.00504569	0.00584745	0.00057268	0.00056921	99.39
39	0.00212749	0.00223640	0.00007780	0.00007669	98.58
40	0.00200848	0.00207706	0.00004899	0.00004865	99.32
41	0.00361570	0.00361663	0.00000066	0.00000068	103.17
42	0.01097118	0.01097665	0.00000391	0.00000389	99.59
43	0.01663493	0.01664066	0.00000409	0.00000405	99.11
44	0.02245261	0.02245597	0.00000240	0.00000238	99.20

Unit: MJ/m^3

Table 5.25 SDSA result of cement strain energy density at bone-cement interface $(\delta b_{13} = 0.05 b_{13})$

Element No.	$\psi^1(b-\delta b)$	$\psi^2(b+\delta b)$	$\Delta\psi$	ψ'	$\psi'/\Delta\psi$ %
17	0.00269022	0.00269710	0.00000574	0.00000575	100.11
18	0.00133079	0.00131805	-0.00001062	-0.00001061	99.95
19	0.00137036	0.00134392	-0.00002204	-0.00002221	100.79
20	0.00317454	0.00290071	-0.00022819	-0.00021990	96.37
21	0.00617504	0.00694455	0.00064125	0.00063969	99.76
22	0.00620436	0.00619064	-0.00001143	-0.00001143	99.98
23	0.01228661	0.01231715	0.00002546	0.00002545	99.98
38	0.00547893	0.00546737	-0.00000963	-0.00000946	98.27
39	0.00218966	0.00218430	-0.00000447	-0.00000438	97.92
40	0.00208308	0.00199452	-0.00007380	-0.00007375	99.93
41	0.00408091	0.00337671	-0.00058683	-0.00057272	97.60
42	0.01031683	0.01170512	0.00115691	0.00115518	99.85
43	0.01661703	0.01665964	0.00003551	0.00003513	98.93
44	0.02244699	0.02246155	0.00001213	0.00001216	100.17

Unit: MJ/m^3

Table 5.26 SDSA result of cement strain energy density at bone-cement interface ($\delta b_{16} = 0.05 b_{16}$)

Element No.	$\psi^1(b-\delta b)$	$\psi^2(b+\delta b)$	$\Delta\psi$	ψ'	$\psi'/\Delta\psi$ %
17	0.00269489	0.00269197	-0.00000365	-0.00000379	103.68
18	0.00132634	0.00132239	-0.00000494	-0.00000501	101.55
19	0.00136036	0.00135721	-0.00000394	-0.00000538	136.60
20	0.00298132	0.00295640	-0.00003115	-0.00003109	99.82
21	0.00652988	0.00653925	0.00001172	0.00001146	97.85
22	0.00642815	0.00596540	-0.00057845	-0.00057960	100.20
23	0.01164718	0.01318523	0.00192257	0.00192358	100.05
38	0.00547119	0.00547687	0.00000710	0.00000785	110.49
39	0.00218591	0.00218959	0.00000460	0.00000527	114.46
40	0.00204024	0.00205013	0.00001236	0.00001201	97.20
41	0.00361341	0.00361749	0.00000510	0.00000538	105.44
42	0.01090816	0.01104407	0.00016989	0.00016935	99.68
43	0.01703955	0.01618361	-0.00106993	-0.00107044	100.05
44	0.02156807	0.02362472	0.00257081	0.00257243	100.06

Unit: MJ/m^3

Table 5.27 SDSA result of bone principal stress at bone-cement interface ($\delta b_9 = 0.05b_9$)

Element No.	$\psi^1(b-\delta b)$	$\psi^2(b+\delta b)$	$\Delta\psi$	ψ'	$\psi'/\Delta\psi$ %
45	5.771703	5.260187	-0.365368	-0.361362	98.90
46	3.437655	3.497112	0.042469	0.042221	99.42
47	6.875564	6.887976	0.008866	0.008797	99.22
48	18.168351	18.162787	-0.003974	-0.003914	98.49
49	29.978807	29.983238	0.003165	0.003132	98.96
50	34.550406	34.552019	0.001152	0.001142	99.13
51	36.989277	36.989106	-0.000122	-0.000122	99.72
72	3.664535	3.711235	0.033357	0.032820	98.39
73	3.941822	3.983808	0.029990	0.029660	98.90
74	5.521963	5.563932	0.029978	0.029663	98.94
75	4.577002	4.593381	0.011700	0.011616	99.29
76	11.514850	11.511817	-0.002166	-0.002145	98.99
77	13.022213	13.022624	0.000294	0.000291	99.09
78	17.572059	17.572424	0.000261	0.000259	99.14

Unit: MPa

Table 5.28 SDSA result of bone principal stress at bone-cement interface $(\delta b_{13} = 0.05 b_{13})$

Element No.	$\psi^1(b-\delta b)$	$\psi^2(b+\delta b)$	$\Delta\psi$	ψ'	$\psi'/\Delta\psi$ %
45	5.493359	5.496115	0.002296	0.002320	101.02
46	3.462200	3.478236	0.013363	0.013394	100.23
47	6.973965	6.781051	-0.160762	-0.161116	100.22
48	16.783281	19.638211	2.379108	2.377839	99.95
49	30.228846	29.631530	-0.497763	-0.494234	99.29
50	34.525239	34.580757	0.046265	0.046103	99.65
51	36.986492	36.991465	0.004144	0.004223	101.91
72	3.688663	3.685393	-0.002724	-0.002703	99.21
73	3.966744	3.961500	-0.004370	-0.004402	100.75
74	5.568287	5.515670	-0.043847	-0.043884	100.08
75	4.154287	5.073113	0.765688	0.764854	99.89
76	11.507936	11.532850	0.020762	0.020498	98.73
77	13.024097	13.021860	-0.001864	-0.001914	102.68
78	17.580469	17.563570	-0.014083	-0.014096	100.10

Unit: MPa

Table 5.29 SDSA result of bone principal stress at bone-cement interface $(\delta b_{16} = 0.05 b_{16})$

Element No.	$\psi^1(b-\delta b)$	$\psi^2(b+\delta b)$	$\Delta\psi$	ψ'	$\psi'/\Delta\psi$ %
45	5.496148	5.493129	-0.003774	-0.003771	99.92
46	3.471087	3.468513	-0.003218	-0.003217	99.96
47	6.884771	6.879792	-0.006224	-0.006216	99.87
48	18.172716	18.158368	-0.017935	-0.017926	99.95
49	30.015334	29.946908	-0.085533	-0.085418	99.87
50	34.794152	34.307064	-0.608860	-0.609594	100.12
51	34.152319	39.960259	7.259925	7.255245	99.94
72	3.687167	3.688075	0.001135	0.001134	99.91
73	3.964230	3.965543	0.001641	0.001639	99.90
74	5.542266	5.547429	0.006455	0.006446	99.86
75	4.590863	4.579241	-0.014527	-0.014491	99.75
76	11.477098	11.553421	0.095404	0.095253	99.84
77	13.167909	12.857647	-0.387828	-0.387498	99.92
78	16.591005	18.630912	2.549884	2.546602	99.87

Unit: MPa

Table 5.30 Accuracy of hip joint SDSA results

Design/ Parameter	Grade A	B	C	D	F
1	14				
5	14				
8	14				
1	14				
5	14				
8	14				
9	14				
13	14				
16	11	1	1	1	
9	14				
13	14				
16	14				
Average %	98.2	0.6	0.6	0.6	0.0

CHAPTER 6

SHAPE DESIGN OPTIMIZATION

6.1 Engine Bearing Cap

Shape optimal design of anengine bearing cap [6,39] is investigated using the method proposed. The finite element model used for the engine bearing cap is shown in Fig. 6.1. Half of the model is used for analysis and design, due to structural symmetry in the thickness direction. The thickness of the bearing cap is assumed to be uniform, with magnitude 23.825 mm. The cap is clamped to the bulkhead by two bolts. Each bolt applies a compressive load of 65,725 N [6] in the cap. This bolt load is distributed on the area under bolt head. A profile of oil film pressure between the journal and bearing cap [6,39] is shown in Fig. 6.2. The resultant force of the oil film pressure in the x_2-direction is 24,840 N [39], which corresponds to a maximum oil film pressure of 3,648 psi (or 26.16 MPa). For a cast iron bearing cap, Young's modulus and Poison's ratio are 100. GPa and 0.3, respectively. The cap finite element model consists of 116 20-node isoparametric solid elements, 927 nodes, and 2204 active degrees-of-freedom.

The bottom of the cap is assumed to be fixed on a rigid bulkhead. This assumption is justified by the finite element analysis that no x_2-direction tensile stress is developed in the bottom flat surfaces. The

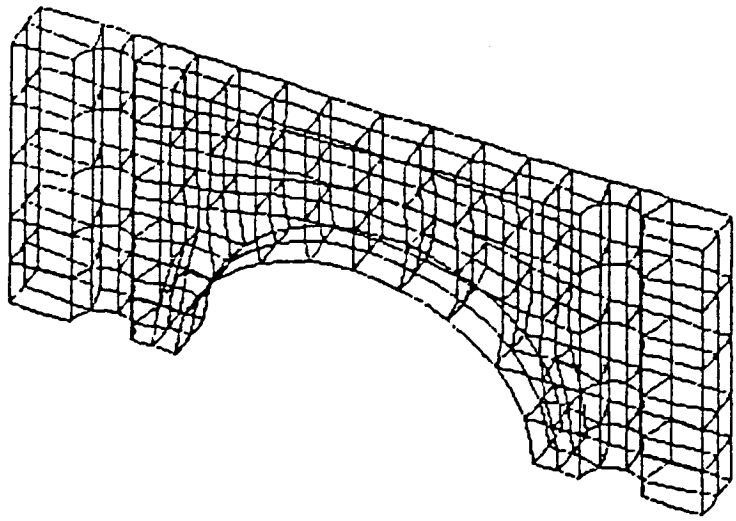

(a) With hidden lines

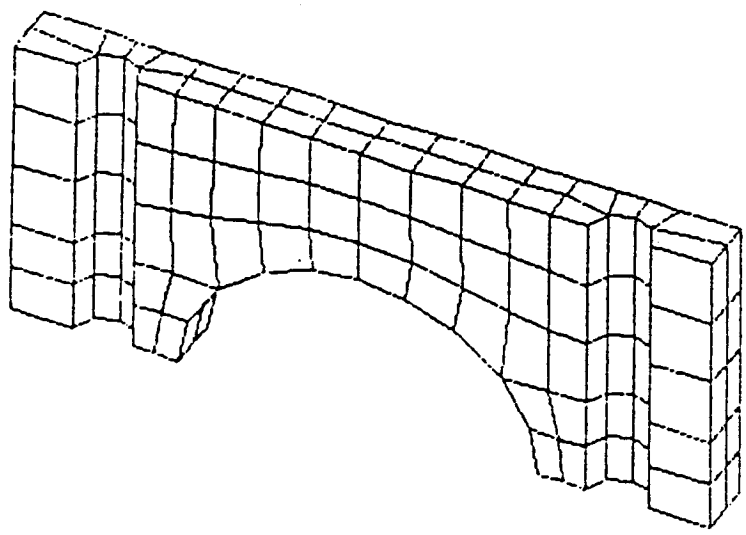

(b) Hidden lines removed

Figure 6.1 Engine bearing cap finite element model

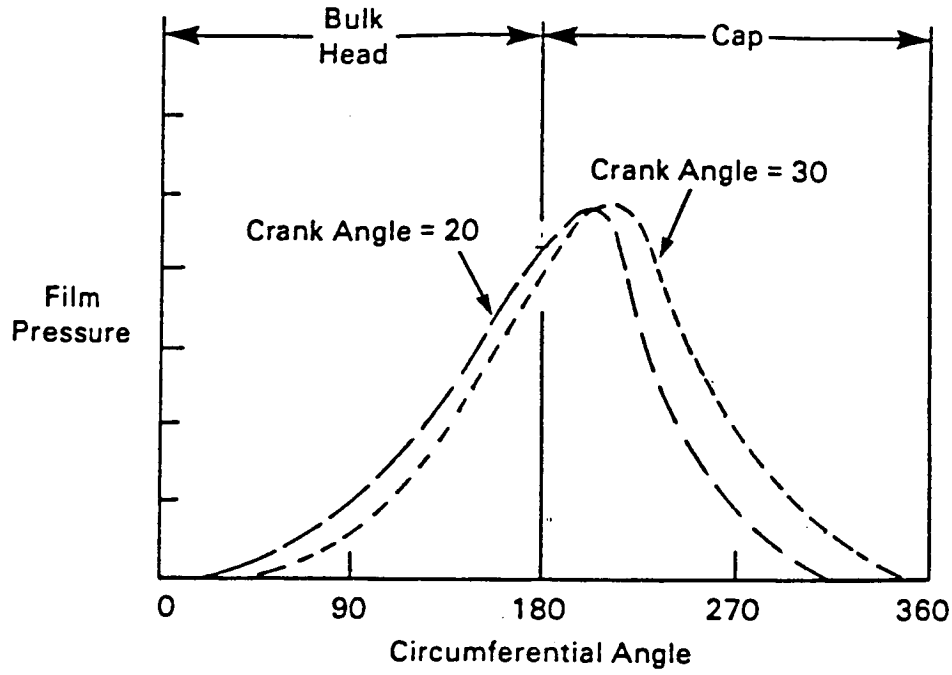

Figure 6.2 Bearing cap pressure profile

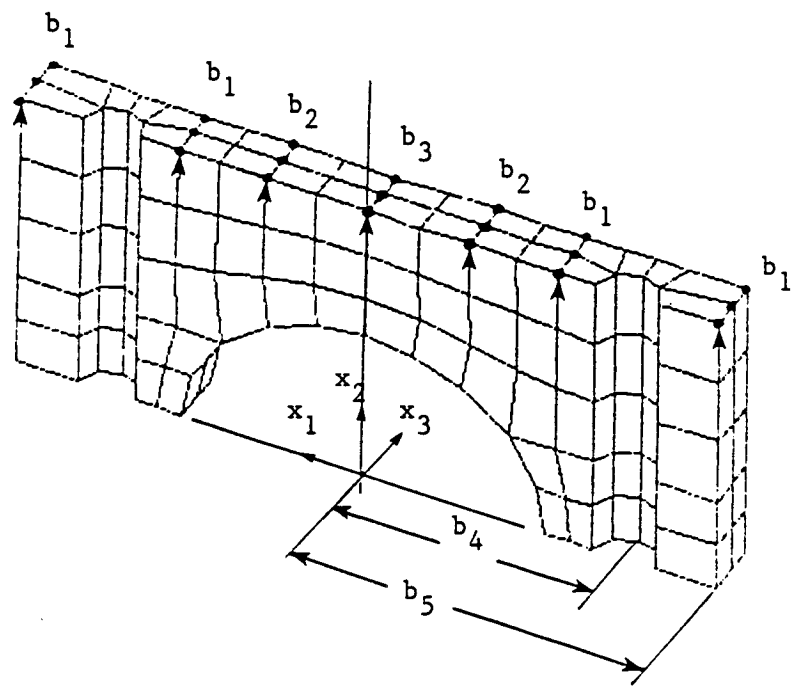

Figure 6.3 Shape design parameter of bearing cap

cap remains in firm contact with the journal, even under the highest oil film pressure load. All other nodes are free to move, except that nodes in the plane of symmetry are constrained in the x_3-direction.

The top surface of the cap is parameterized by a singly-curvatured Bezier surface, with 3 control points, as shown in Fig. 6.3. The x_2-coordinates of these control points are selected as the first three design parameters, with first and second control points moving simultaneously, to obtain a symmetric design, which is considered to be more conservative than a non-symmetric one. The distance of the center line of the clamping bolt from the center line of cap is chosen as the fourth design parameter, while the distance of the cap edge from the center line of cap is defined as the fifth design parameter.

The boundary displacement method is used to generate five sets of design velocity fields, corresponding to the five shape design parameters. For the first three sets of velocity fields, boundary velocities are determined by perturbing the x_2-coordinates of each control point a unit magnitude in Eq. 3.2.17. The associated domain velocity fields are obtained by solving Eq. 4.1.3 for each set. A boundary layer of 20 (out of 116) elements is constructed for design parameter 4 (Fig. 6.4) and a boundary layer of 10 elements along the edge of the cap is defined for design parameter 5 (Fig. 6.5). The values of initial design parameters are listed in Table 6.1.

6.1.1 Optimization Procedure

The design problem is to minimize total volume of the cap, while the maximum cap bearing surface displacement in the radial direction is

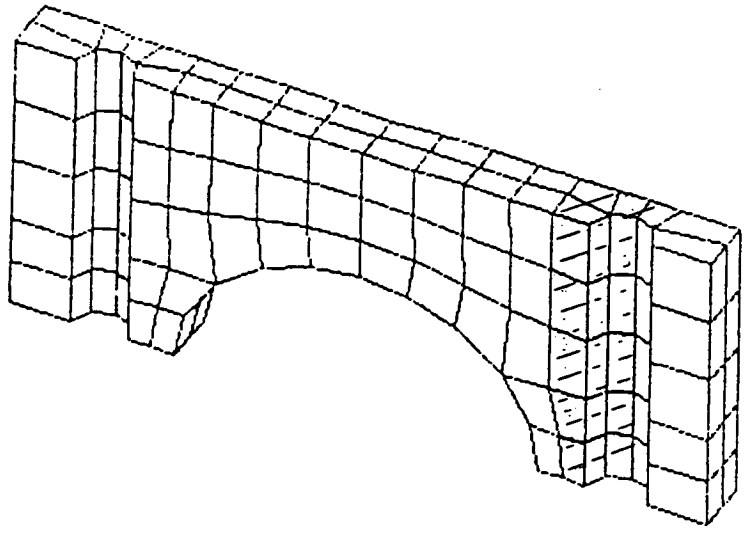

Figure 6.4 Boundary layer for design parameter 4

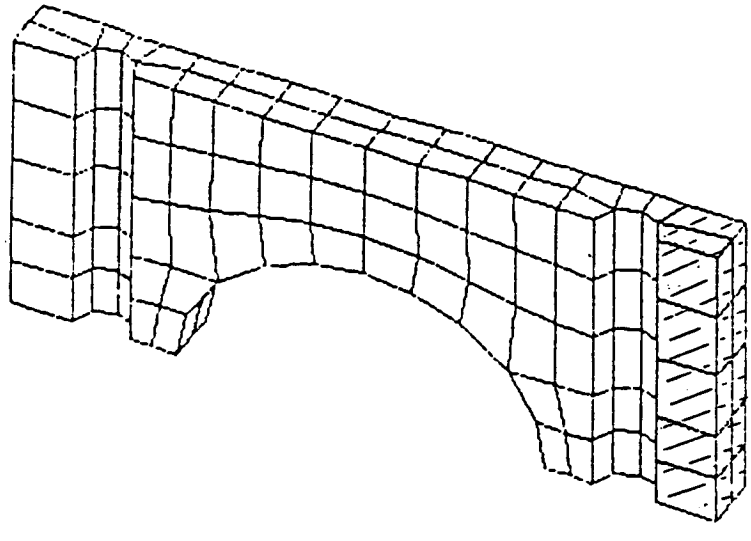

Figure 6.5 Boundary layer for design parameter 5

maintained less than 0.0165 mm and the failure criterion for brittle material [39] is satisfied. The displacement constraint is established based on the requirement that the allowable clearance between the journal bearing and cap must be maintained within the range of 0.0012 in. -0.0025 in. The mean clearance is 0.00185 in. and the allowable deviation is 0.00065 in. (or 0.0165 mm). That is, the cap must not deform over 0.0165 mm in the radial direction at the bearing surface for proper lubrication.

The material failure criterion is expressed as

$$\frac{1}{2}\left[(\sigma_1-\sigma_2)^2 + (\sigma_2-\sigma_3)^2 + (\sigma_3-\sigma_1)^2\right] < \frac{X_T X_C}{S} \tag{6.1.1}$$

where S is the factor of safety, which takes into account the effect of fatigue and prestressing of the part; X_T is the ultimate tensile strength; X_C is the ultimate compressive strength; and σ_1, σ_2, and σ_3 are three principal stresses. Values used are S = 2., X_T = 206.7 MPa, and X_C = 751. MPa. This constraint is applied at each Gaussian point of each element, except those points near nodes where the clamped bolt loads are applied, since stresses are not accurate due to the approximation of bolt load as a concentrated load.

The LINRM program [99,100,101] is used for iterative optimization.

6.1.2 Results and Discussion

It is important that the optimum shape satisfy the displacement constraint for both static state (only the bolt load is acting) and

working state (both the bolt load and oil film pressure are acting). The cap, subjected to clamped bolt load, is analyzed with and without oil film pressure, to study the effect of bolt load and bolt load-oil film pressure interaction. In Fig. 6.6, the solid line represents cap deformation due to pure bolt load, while the dashed line represents the undeformed shape. In this case, the maximum radial displacement is 0.0251 mm. Similarly, Fig. 6.7 shows cap deformation due to bolt load and oil film pressure, and the maximum radial displacement is 0.0266 mm. Figure 6.7 illustrates that the cap swings to one side, due to non-symmetric oil film pressure. This side-swing displacement leads to some difficulties in the shape optimization process. After 5 design interations, the initial shape (Fig. 6.1) evolves to the shape shown in Fig. 6.8. The maximum cap displacement constraint becomes 0.01796 mm and the cap total volume becomes 94,071 mm^3. At this point, the optimization process seems to be trapped at a local minimum, since the design change step becomes very small. Further design change only causes radial displacements to oscillate. The cost and constraint history are shown in Table 6.2.

A new initial design of the cap is constructed, as shown in Fig. 6.9. The new design parameters are listed in Table 6.3. The total volume of this new design is 58,175 mm^3. with a maximum displacement of 0.0257 mm. The maximum radial displacement due to bolt load is 0.0191 mm. After 12 design iterations, an optimal shape is reached, as shown in Fig. 6.10. All constraints and solution convergence criteria are satisfied. The cost and constraint history are given in Table 6.4. The

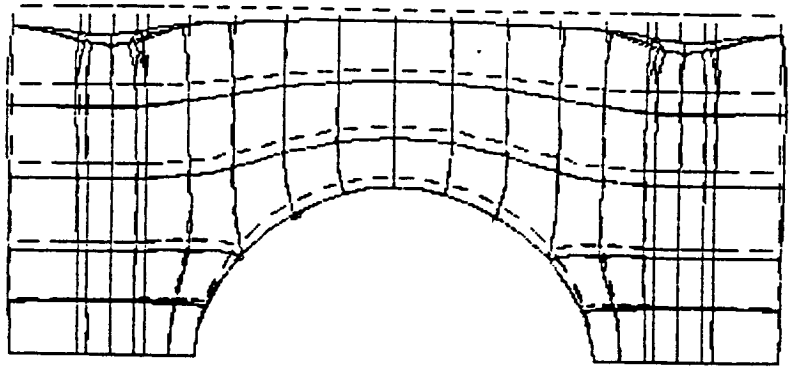

Figure 6.6 Cap deformation due to bolt load only (initial design)

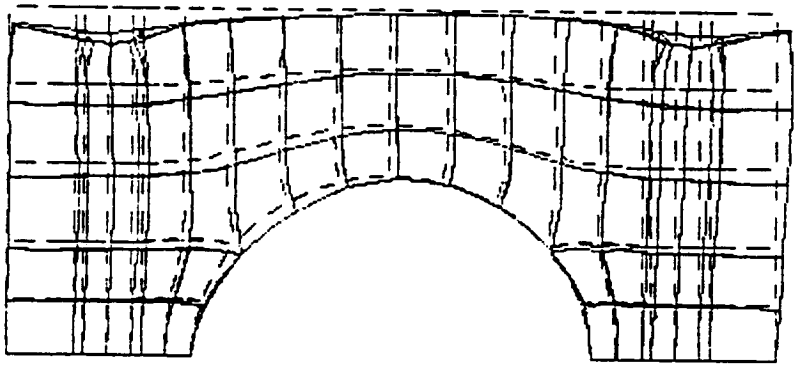

Figure 6.7 Cap deformation due to bolt load and oil film pressure (initial design)

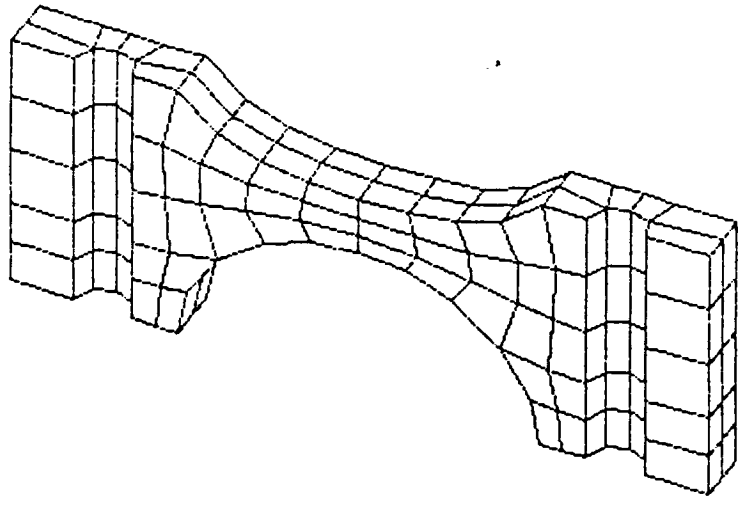

(a) Hidden lines removed

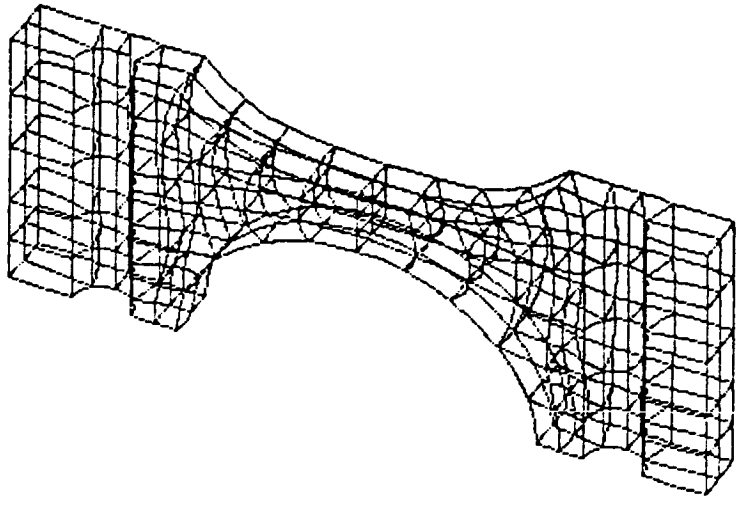

(b) With hidden lines

Figure 6.8 Design shape of a local minimum

Table 6.1 Shape design parameters of cap design 1

Parameter No.	Initial Design	Final Design	Lower Bound	Upper Bound
1	73.	74.64	30.	76.2
2	73.	62.15	30.	120.0
3	73.	31.46	30.	150.0
4	53.975	57.14	47.	57.15
5	73.025	77.29	65.405	78.105

Unit: mm

Table 6.2 Optimization history of cap design 1

Iteration No.	Cost (Total Volume) mm^3	Maximum Constraint (Radial Displacement) mm	No. of Constraint Violations
0	90,782.5	0.02656	6
1	79,850.0	0.02255	6
2	84,460.0	0.01982	3
3	88,624.0	0.01939	3
4	93,927.0	0.01799	3
5	94,023.0	0.01796	3

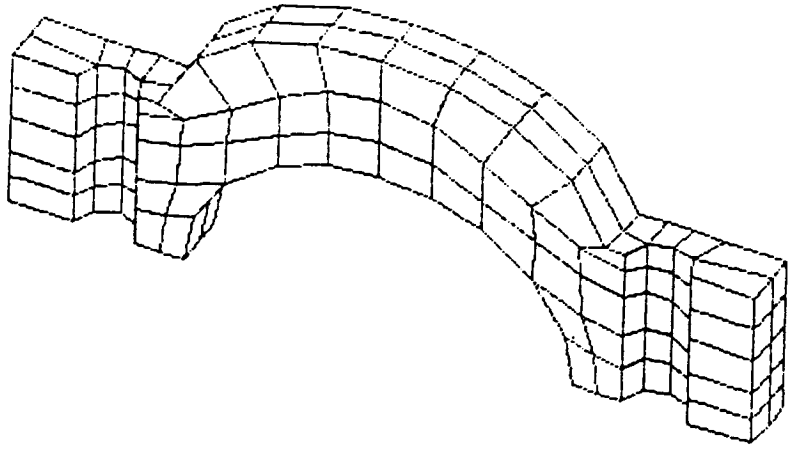

(a) Hidden lines removed

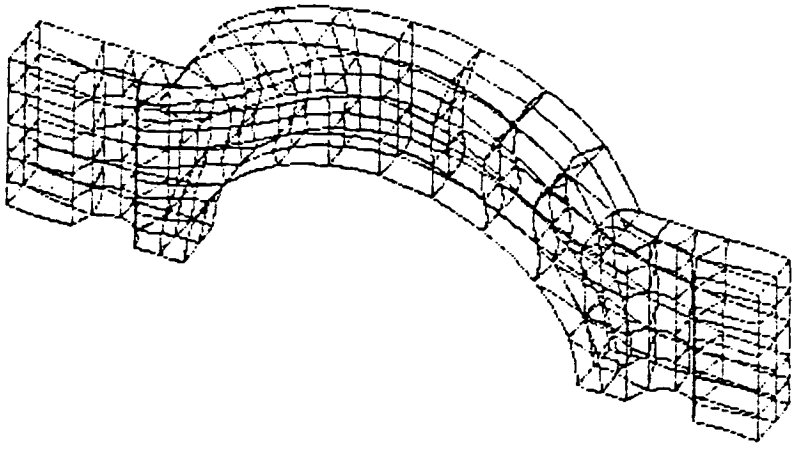

(b) With hidden lines

Figure 6.9 Initial shape of modified cap

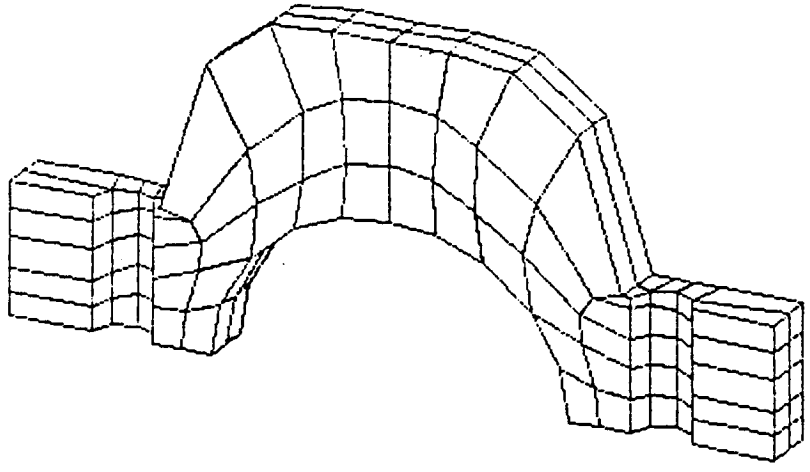

(a) Hidden lines removed

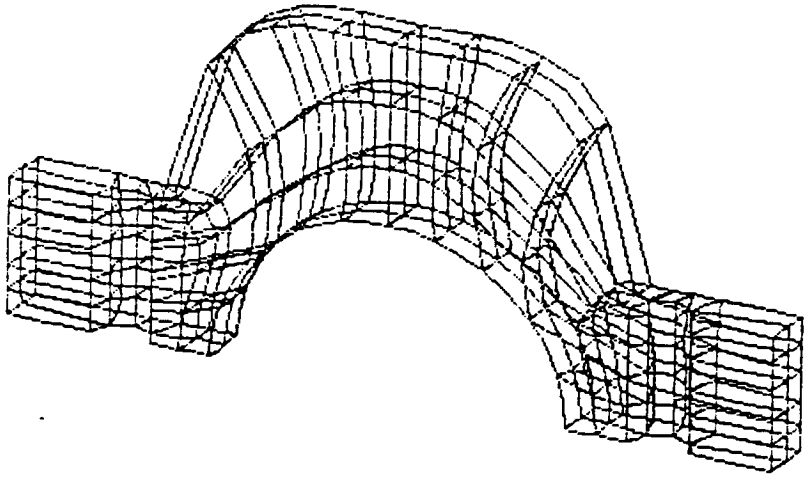

(b) With hidden lines

Figure 6.10 An optimum shape of cap (symmetric design)

Table 6.3 Shape design parameters of cap design 2

Parameter No.	Initial Design	Final Design	Lower Bound	Upper Bound
1	38.	30.90	30.	76.2
2	73.	136.41	30.	150.0
3	73.	20.0	20.	150.0
4	53.975	57.15	47.	57.15
5	73.025	78.10	65.405	78.105

Unit: mm

Table 6.4 Optimization history of cap design 2

Iteration No.	Cost (Total Volume) mm^3	Maximum Constraint (Radial Displacement) mm	No. of Constraint Violations
0	58,175.	0.02572	4
1	66,547.	0.01969	3
2	70,274.	0.01747	3
3	70,596.	0.01724	3
4	71,398.	0.01739	4
5	74,702.	0.01697	2
6	74,994.	0.01687	2
7	74,727.	0.01677	2
8	75,751.	0.01676	2
9	76,638.	0.01663	2
10	77,094.	0.01657	2
11	77,327.	0.01653	2
12	77,557.	0.01649	0

total volume of this shape is 77,557 mm^3. This optimum shape is quite different from the one determined when iteration failed. It is also different from the optimum shape obtained in Ref. 39. However, it appears similar to the shape obtained by Imam [6].

The reasons behind these two totally different shapes are explained as follows. Design 1, which failed, tends to distribute more material around the bolt hole, to increase structural stiffness and prevent displacement due to sideway swing. It removes material from the cap middle portion, so that deformation due to oil film pressure offsets deformation due to the bolt clamping load. The successfully optimized design 2 tends to reduce length of the clamping bolt and consequently the bolt clamping deformation. It increases material and structural stiffness in the middle portion of the cap, to reduce deformation due to oil film pressure. In engineering practice, it is desirable to have minimum cap deformation due to bolt load, such that good lubrication is possible when an engine starts to run. It is also desirable to have a stiff cap, to minimize deformation due to oil film pressure, such that consistent lubrication can be maintained when an engine is running with varying oil film pressure. Therefore, the optimal shape obtained in this work does make engineering sense.

The optimum cap is tested with bolt load to check the bolt clamping effect. It is found that the maximum cap radial displacement, due to bolt load, is 0.0129 mm (less than the critical value 0.0165 mm). This behavior suggests that bolt load need not be considered as a separate load for design optimization.

In another study, a non-symmetric design is tested, with a bolt axial force of 53,400 N and the oil film pressure load of Fig. 6.2 (the maximum pressure is 25.16 MPa.). After 7 iterations, the initial shape (Fig. 6.1) changes to a non-symmetric shape, as shown Fig. 6.11. The total volume is 76,290 mm^3 and the maximum radial deformation is 0.0124 mm (less than 0.0005 in.). This non-symmetric design is a compromise between Figs. 6.8 and 6.10. On one side of the cap, more material is clustered, to increase local structural stiffness and prevent sideway deformation. On the other side, material is removed to make deformations due to bolt load and oil film pressure balance.

It seems that a more restrictive cap distortion constraint can be achieved only through a non-symmetric design. However, from a conservative design point of view, a non-symmetric design may not be a favorable choice. To gain further insight into the influence of oil film pressure, numerical analysis is conducted to test cap deformation, with the peak oil film pressure at different crank angles. It is found that the cap deforms much less sideways when the peak oil film pressure occurs at a larger crank angle. This suggests that a bulkhead design with the cap mount tilted to gain a larger crank angle may be a more effective way to reduce cap distortion and cap total volume.

The computational cost is estimated in terms of CPU time of a VAX11-780 computer. The main analysis takes 1215. sec., while each adjoint analysis takes 126. sec. Shape design sensitivity analysis consumes 24. sec. per constraint per design parameter. In the optimization process of design 2, with 5 design parameters, there are 12 reanalyses and 33 adjoint analyses. The cost is estimated as

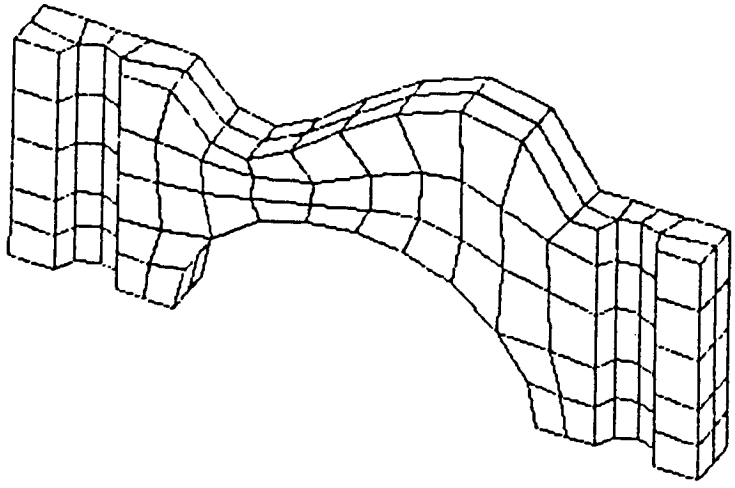

(a) Hidden lines removed

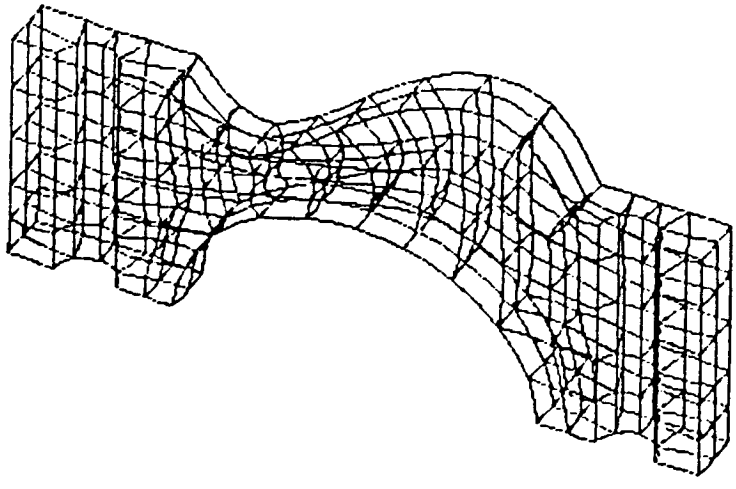

(b) With hidden lines

Figure 6.11 An optimum shape of cap (non-symmetric design)

$$\text{Total time} = 1215. \times 12 + 126. \times 33 + 24. \times 33 \times 5$$
$$= 22{,}700. \text{ sec.}$$

The cost of the interactive procedure and design velocity field generation is estimated as roughly 6,000 sec. Therefore, the overall cost is 28,700 CPU sec. or 8. CPU hours.

6.2 Doubly-Curved Arch Dam

The physical definition of an arch dam has been described in Chapter 5, where the arch dam was modeled by 32 design parameters, which are x_2-coordinate of 32 control points that form 2 Bezier surfaces (Fig. 5.9). Accuracy of shape design sensitivity analysis results was tested for eight design parameters.

As shown in Fig. 5.10, the initial shape of the dam is similar to that of a gravity dam, a very simple straight model, and sensitivity analysis was based on this simple model. In carrying out the optimization study, it was found that the initial shape of a gravity dam evolves to a shape with a local minimum, a gravity dam with a fillet in the fixed portion. It did not evolve to a doubly-curved arch dam after several design iterations, while the cost and constraint violations are reducing. Therefore, this gravity dam is not used as an initial design shape. Rather, the optimum shape obtained by Wassermann [7] is used as an initial design, with analysis done using 20-node quadratic isoparametric elements. A comparison of analysis results of the Wassermann's optimal design, using an 8-node model, and the 20-node model used in this work is given in Table 6.5.

Table 6.5 Comparison of 8-node and 20-node models (Wassermann's optimal design)

	8-node (Wassermann's)	20-node (this work)
Total elements	36	36
Total nodes	98	315
Active d.o.f.	216	726
Maximum tensile stress	2.0 MPa	3.9 MPa
design parameters	21	32

Table 6.6 Shape design parameters of arch dam

No.	Initial Design	Final Design
1	115.00	108.45
2	115.00	99.51
3	111.00	109.71
4	103.00	98.70
5	128.50	142.14
6	128.50	137.20
7	108.00	122.08
8	72.00	68.49
9	132.50	125.93
10	132.50	127.60
11	101.00	116.82
12	54.50	73.18
13	119.00	97.90
14	119.00	108.22
15	83.00	84.75
16	10.00	12.00
17	141.00	155.49
18	141.00	153.53
19	138.00	154.24
20	130.00	151.76
21	146.00	132.26
22	146.00	141.43
23	130.00	125.68
24	95.00	77.00
25	155.50	139.35
26	155.50	147.33
27	119.00	107.28
28	74.50	59.15
29	129.00	115.64
30	129.00	112.92
31	93.00	90.43
32	20.00	18.01

Unit: meter

Notice that the highest tensile stress reported using the 20-node isoparametric finite element model is almost twice that obtained using an 8-node isoparametric finite element model. Apparently, this difference is due to the difference in finite elements used. Furthermore, principal stress as are evaluated at Gaussian points located in the water pressured surface in this work, while the stress state presented by Wassermann is in the interior of the arch dam. From an energy point of view in the finite element method, the stiffness of a structure that is represented by a larger number of degrees of freedom will be 'softer'. Meanwhile, it is observed that the dam behaves like a beam, according to stress distribution over entire dam. That is, the maximum (compressive or tensile) stress appears on the surface. This explains the higher stress state obtained with the 20-node model. Based on this observation, principal stress in the water pressure surface (upstream) and free surface (downstream) will be used as stress constraints. When Wassermann's optimal design is modeled by 20-node finite elements, more than 100 Gaussian points have principal stress higher than 2000 KPa. In order to accelerate the optimization process, this initial design is uniformly thickened by 6 meters. This initial shape is shown in Fig. 6.12 and the corresponding 32 design parameters are listed in Table 6.6.

6.2.1 Optimization Procedure

The optimization problem is to minimize total volume of the arch dam, subject to thickness and principal stress constraints. The thickness constraint is expressed as

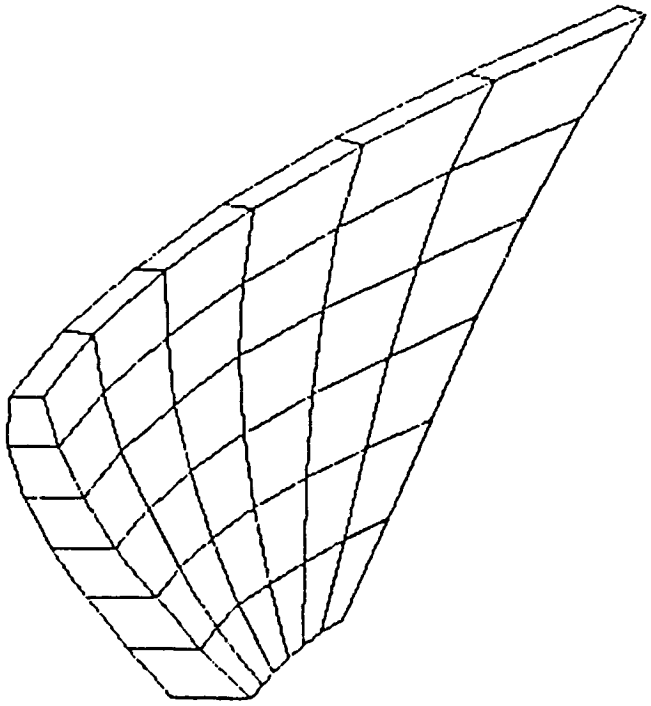

(a) Hidden lines removed

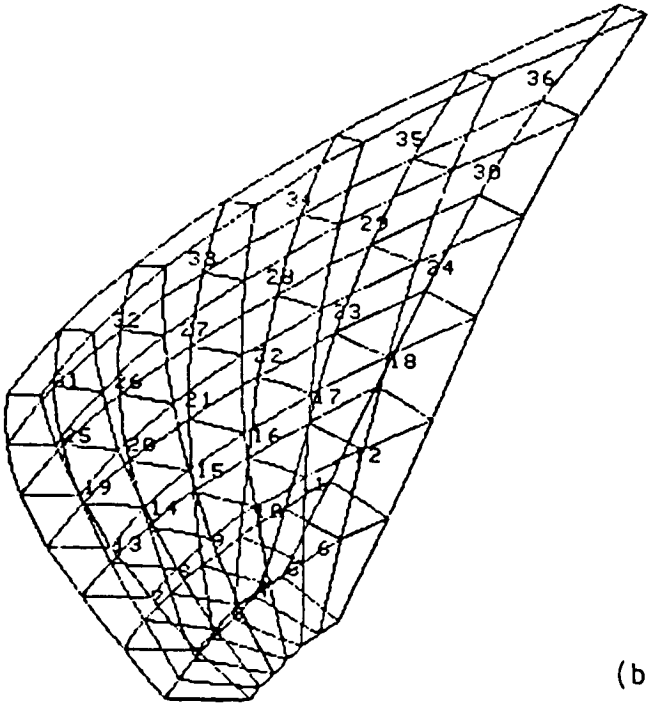

(b) With hidden lines

Figure 6.12 Initial shape of arch dam

$$\psi(T_i) = 1. - T_i/T_{min} \tag{6.2.1}$$

Four thickness constraints imposed at the top of the dam. The minimum thickness (T_{min}) is 6. The stress constraint is expressed as

$$\psi(\sigma_i) = \sigma_i/S_T - 1. < 0, \quad \text{for tensile stress}$$

$$\psi(\sigma_i) = 1. - \sigma_i/S_C < 0, \quad \text{for compressive stress}$$

Where σ_i is the i-th principal stress; S_T is the concrete tensile yielding stress, with the value of 2. MPa; and S_C is concrete compressive yielding stress, with the value of -10. MPa. There are a total of 1944 stress constraints.

The mathematical programming method applied in this study is LINRM, which is constructed based on Pshenichny's linearization method [99,100,101]. In applying LINRM for arch dam surface optimization, several strategies are used as follows:

(1) Normalization. The cost function is normalized by the cost gradient norm. That is

$$F = f/\|df\|$$

$$\|df\| = \sum_{n=1}^{N} (df_n \cdot df_n)$$

where F is the normalized cost, f is the original cost, df is the gradient of cost, and N is the number of design parameters. Constraint functionals are normalized to bring all different constraints to a similar level, by the constraint gradient norm,

$$\hat{\psi}_i = \psi_i / \|dg_i\|,$$

$$\|dg_i\| = \sum_{n=1}^{N} (dg_{i,n} \cdot dg_{i,n})$$

where $\hat{\psi}_i$ is the normalized constraint and $dg_{i,n}$ is the gradient of i-th constraint with respect to n-th design parameter.

(2) Shifting. A shifting factor may be introduced to increase or reduce the normalized cost during optimization. A higher shifting factor may be used in the early stages, to accelerate cost reduction. A smaller shifting factor may be used when approaching an optimum. It was noted that a large shifting factor will accelerate cost reduction in the beginning, but cause cost or constraint fluctuation in near an optimum. On the other hand, if the shifting factor is too small, it will take many steps to reach an optimum.

(3) Flexible design parameter upper and lower bounds. For the arch dam, two Bezier surfaces are defined to parametrize faces of the dam. It is possible that the design upper bound of one surface may interfere with the lower bound of another surface and lead to a poor design. To avoid this potential problem, it is necessary to check all design bounds after each design iteration. If any interference is found, the associated design bounds must be changed, to avoid such an interference. It may take several trials to obtain a reasonable result. The design bounds must be defined in a manner that will provide necessary control over the shape change, but also leave enough space for natural shape growth.

6.2.2 Results and Discussion

After 18 design iterations, all constraint violations are eliminated and cost reduction becomes small. Therefore, the final design obtained in the 18-th iteration is considered as the optimum, shown in Fig. 6.13. The final cost (total volume of the dam) is reduced from the original value of 253,566 m^3 to 182,583 m^3, which is 8.5 % lower than Wassermann's 199,610 m^3. The maximum tensile stress is reduced from the original value of 3.084 MPa to 1.981 MPa. The design optimization history is reported in Table 6.7 and Fig. 6.20. Final design parameters are listed in Table 6.5.

As can be seen from Fig. 6.13, the difference between this optimum shape and Wassermann's optimum shape is mainly in the bottom portion. The optimum shape obtained in this work tends to 'grow' fillets in corners, particulary in the dam bottom area, which is much thicker than that of Wassermann's design. This thickened shape seems to be more natural for the base of a cantilever structure. In fact, this shape also appears in Ref. 30, 37 for a gravity dam, and in Ref. 39 for a three dimensional cantilever beam. In the crown cross-section, the region slightly above the middle is thinner than the top. This phenomenon is also observed in Refs. 30 and 37. In the optimal shape, it is found that high tensile stress appears in both upstream and downstream surfaces. In Figs. 6.14-6.19, six element layers are depicted, to see if any peculiar shape may occur. It is found that other than the bottom portion, the layer cross sections retain basically the same pattern as obtained by Wassermann. Wassermann's optimal shape

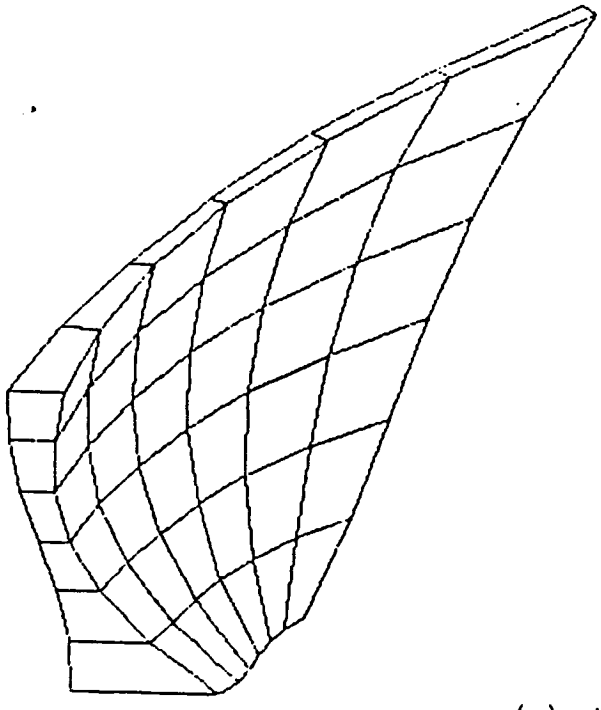

(a) Hidden lines removed

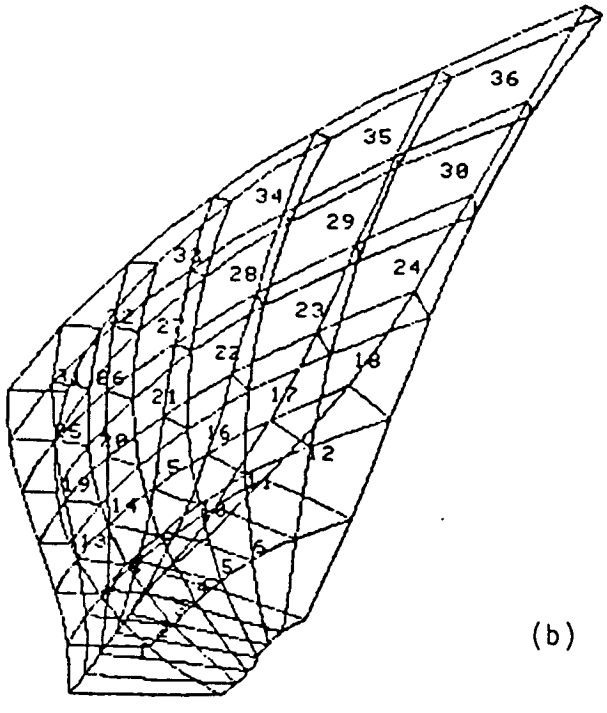

(b) With hidden lines

Figure 6.13 Optimal shape of arch dam

Table 6.7. Optimization history of arch dam

Iteration	Cost (Total Volume) m^3	Maximum Constraint (Principal stress) KPa	No. of Constraint Violations
0	253,566.	3,084.	15
1	252,735.	2,943.	15
2	255,810.	2,502.	12
3	260,570.	2,264.	10
4	254,431.	2,130.	7
5	245,377.	2,085.	11
6	237,699.	2,019.	6
7	226,867.	1,998.	0
8	220,059.	2,118.	7
9	208,468.	2,005.	4
10	198,295.	2,322.	9
11	188,809.	2,193.	7
12	181,148.	2,347.	23
13	180,183.	2,135.	18
14	184,003.	2,123.	5
15	183,593.	2,036.	8
16	182,430.	2,052.	7
17	182,583.	1,981.	0

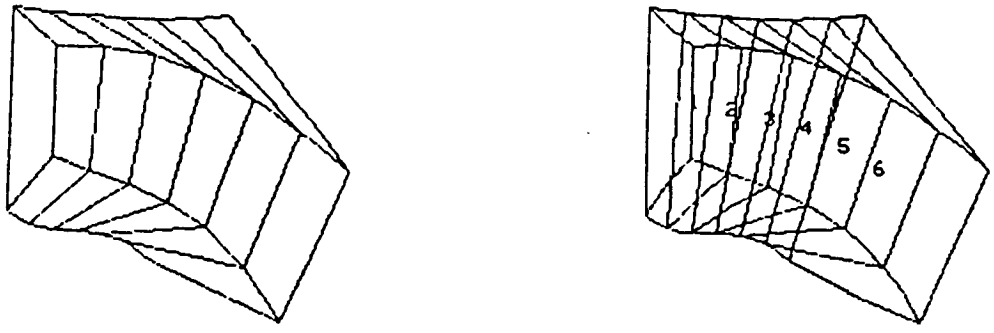

(a) Hidden lines removed (b) With hidden lines

Figure 6.14 Optimum arch dam element layer 1

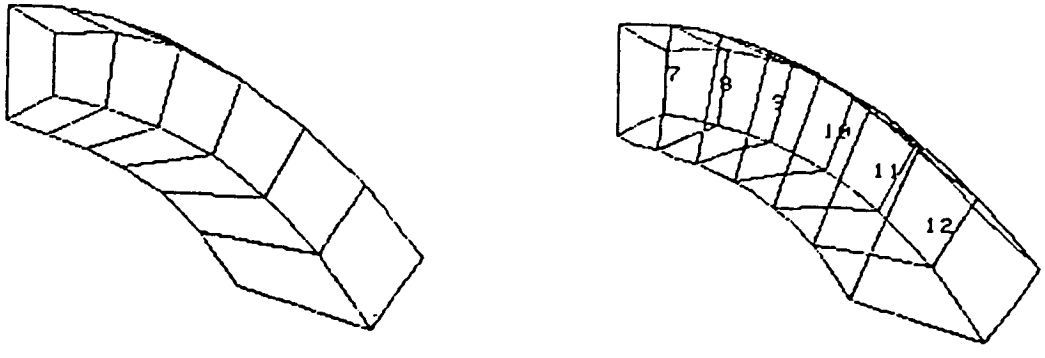

(a) Hidden lines removed (b) With hidden lines

Figure 6.15 Optimal arch dam element layer 2

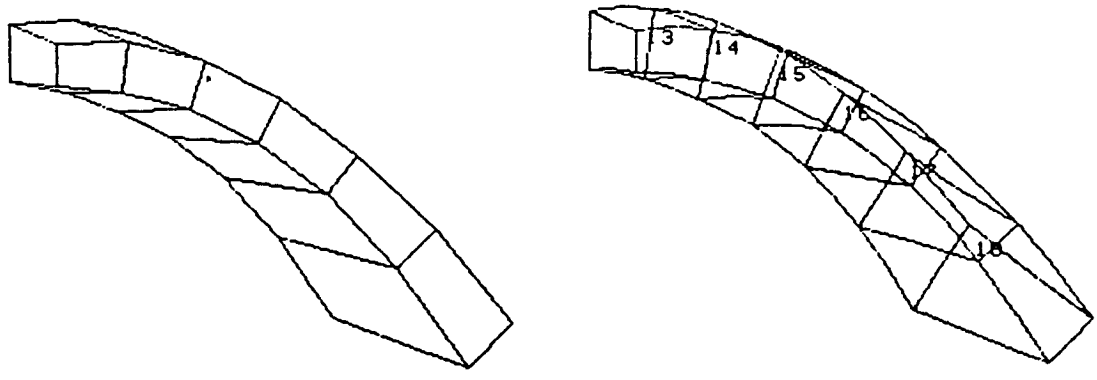

(a) Hidden lines removed (b) With hidden lines

Figure 6.16 Optimum arch dam element layer 3

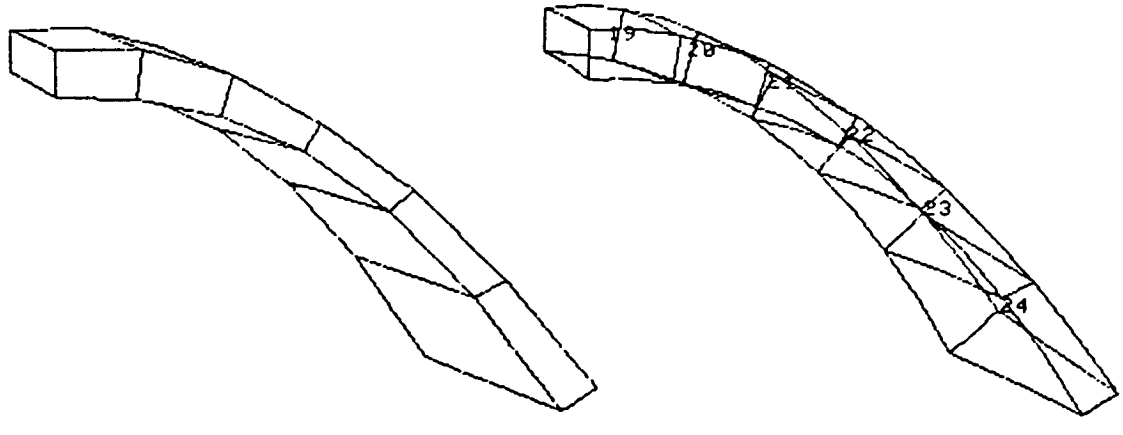

(a) Hidden lines removed (b) With hidden lines

Figure 6.17 Optimum arch dam element layer 4

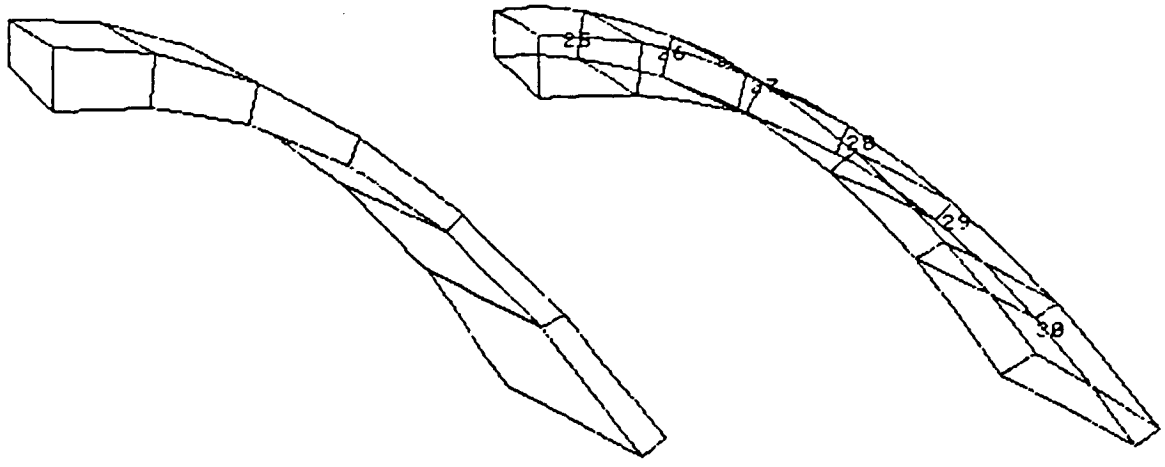

(a) Hidden lines removed (b) With hidden lines

Figure 6.18 Optimum arch dam element layer 5

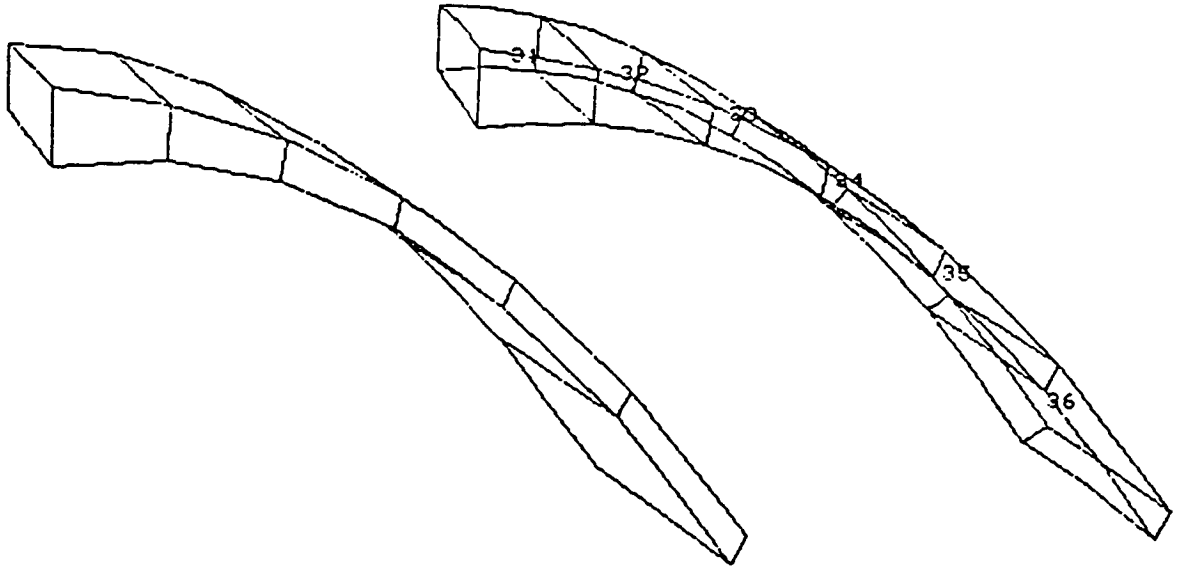

(a) Hidden lines removed (b) With hidden lines

Figure 6.19 Optimum arch dam element layer 6

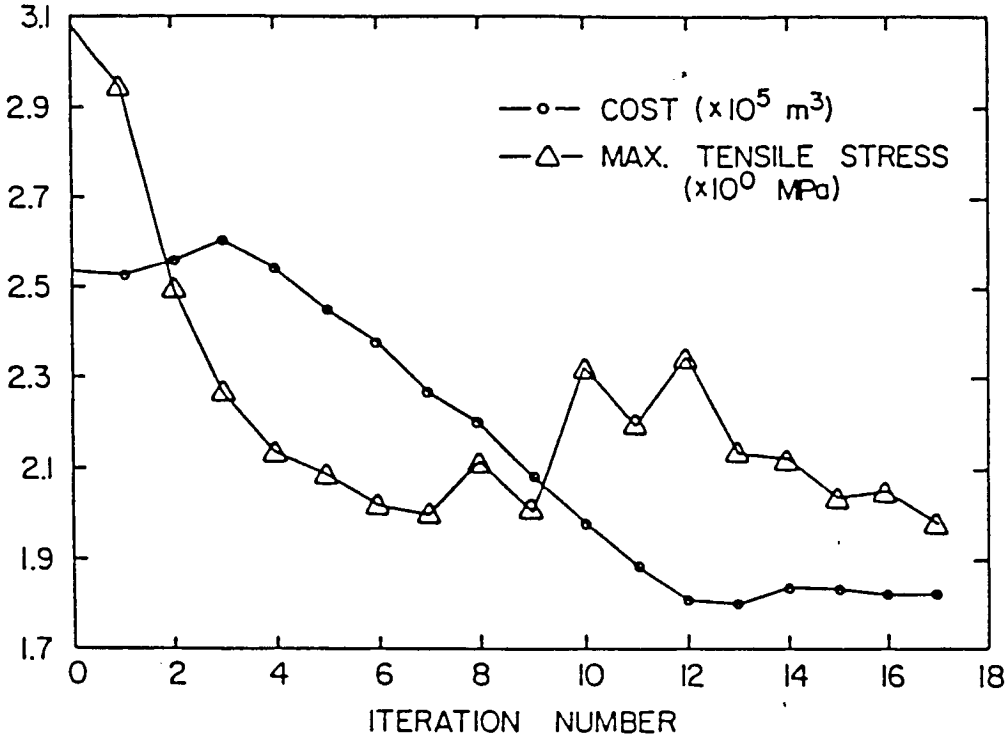

Figure 6.20 Arch dam optimization cost-constraint history

is highly infeasible, based on the 20-nodes finite element analysis. However, after 18 iterations of geometric rearrangement, the optimum shape obtained in this work is 8.5 % lighter than Wassermann's shape.

Computational cost is estimated in terms of CPU time on a VAX11-780 computer. The main analysis consumes 400. sec, each adjoint analysis consumes 50. sec., and shape design sensitivity analysis takes 10. sec. per constraint per design parameter. There are a total of 18 reanalyses and 169 adjoint analyses in the arch dam optimization process, with 32 design parameters. Computer cost is estimated as

$$\begin{aligned} \text{Total time} &= 400. \times 18 + 50. \times 169 + 10. \times 169 \times 32 \\ &= 69{,}730. \text{ (CPU seconds)} \end{aligned}$$

The interactive procedure and velocity generation take roughly 9,000 sec. Therefore, the final cost is 78,730 sec., or 21.87 CPU hours.

Shape design sensitivity is further tested for the final shape. It is found that the quality of sensitivity analysis remains at the same level as that of the initial shape.

CHAPTER 7

CONCLUSIONS

Automatic regridding using the boundary displacement method and three dimensional design parametrization, coupled with the unified theory of shape design sensitivity analysis by the adjoint variable method is proved feasible and efficient for general three dimensional elastic solids. Numerical implementation of this sensitivity analysis method in the existing ANSYS code makes it easy to perform shape design sensitivity analysis. Versatility of this method is demonstrated by three examples from different engineering disciplines. Pointwise stress sensitivity is found to be a special case of domain averaged stress sensitivity.

A boundary displacement method is presented as a design velocity field generator for automatic regridding, as well as a mesh generator. This method provides automatic regridding, with grid orthogonality preserved, as shown in the fillet problem of Chapter 4. The boundary layer method, coupled with the boundary displacement method, is shown to be a straight forward and efficient procedure for shape design sensitivity analysis. Shape design sensitivity results agree well with finite difference estimates. The constraint gradient computed by the central difference method converges to that computed by the material derivative.

Shape design parametrizations for two and three dimensional problems are presented and tested with Bezier curves and surfaces. The relationship between design perturbation and domain design velocity field is also established. The doubly-curved arch dam of Section 6.2 demonstrates the procedure for general surface shape design optimization, with varying design upper and lower bounds. The engine bearing cap problem of Section 6.1 shows that different initial designs may lead to different final designs (local minima). The optimal design must thus be judged based on engineering practice.

For future study, this unified theory can be extended to many other continuum shape design problems, such as thermoelasticity for engine block design, electromagnetic field design [102], aerofoil design [102], etc. New developments must also scrutinize the regularity and differentiablity of problems, to ensure existence of design sensitivity, as it was done in Ref. 35.

REFERENCES

1. Zienkiewicz, O.C. and Cambell J.S., "Shape optimization and Sequential Linear Programming", Optimum Structural Design (Ed. R.H. Gallagher and O.C. Zienkwicz) Wiley, New York, 1973, pp. 109-126.

2. Ramakrishnan C.V. and Francavilla A., "Structural Shape Optimization using Penalty Functions", Journal of Structural Mechanics, Vol. 3, No. 4, 1975, pp.403-432.

3. Francavilla A., Ramakrishnan C.V., and Zienkiewicz O.C., "Optimization of Shape to Minize Stress Concentration", Journal of Strain Analysis, Vol. 10,1975, pp. 63-70.

4. Schnack E., "An Optimization Procedure for Stress Concentration by the Finite Element Technique", International Journal for Numerical Methods in Engineering, Vol. 14, 1979, pp. 115-124.

5. Oda J., "On a Technique to Obtain Optimum Strength Shape by the Finite Element Method", Bull. International Journal of Mechanical Engineering, Vol. 20, No.140, 1977, pp.160-167.

6. Imam M.H., "Three-Dimensional Shape Optimization", International Journal for Numerical methods in Engineering, Vol. 18, 1982, pp. 661-673.

7. Wassermann K., "Three-Dimensional Shape Optimization of Arch Dams with Prescribed Shape Functions", Journal of Structural Mechanics, Vol. 11, No. 4, 1983/1984, pp. 465-489.

8. Braibant V., and Fleury C., "Shape Optimal Design Using B-Spline", Computer Methods in Applied Mechanics and Engineering, 44 1984, pp. 247-267.

9. Wang S.Y., Sun Y.B., and Gallagher R.H., "Sensitivity Analysis in Shape Optimization of Continum Structures", Computers and Structures, Vol. 20, No.5, 1985, pp. 855-867.

10. Tvergaard V. "On the Optimum Shape of Fillet in a Flat Bar with Restrictions", Optimization in Structural Design (Ed. A. Sawczuk and Z. Mroz), Springer-Verlag, New York, 1975, pp. 181-195.

11. Kristensen E.S., and Madsen N.F., "On the Optimum Shape of Fillets in PLates Subjected to Multiple In-Plane Loading Cases", International Journal for Numerical Methods in Engineering, Vol. 10, 1976, pp.1007-1019.

12. Bhavikatti S.S., and Ramakrishnan C.V., "Optimum Shape Design of Shoulder Fillets in Tension Bars and T-Heads", International Journal of Mechanical Science, Vol. 21, 1979, pp. 29-39.

13. Kunar R.R., and Chan A.S.L., "A Method for the Configurational Optimization of Structures", Computer Methods in Applied Mechanics and Engineering, Vol. 7, 1976, pp. 331-350.

14. Dems K., and Mroz Z., "Multiparameter Structural Shape Optimization by the Finite Element Method", International Journal for Numerical Methods in Engineering, Vol.13, 1978, pp. 247-263.

15. Dems K., "Multiparameter Shape Optimization of Elastic Bars in Torsion", International Journal for Numerical Methods in Engineering, Vol. 15, 1980, pp. 1517-1539.

16. Seguchi Y., and Tada Y., "Shape Determination Problems of Structures by Inverse Variational Principle, the Finite Element Formulation", Applied Computational Methods in Engineering, Symposium 1977.

17. Oda J., and Yamazaki K., "A Procedure to obtain a Fully Stressed Shape of Elastic Continuum", International Journal for Numerical Methods in Engineering, Vol.15, 1980, pp.1095-1105.

18. Dems K., and Mroz Z., "Variational Approach by Means of Adjoint Systems to Structural Optimization and Sensitivity Analysis -I", International Journal of Solids and Structures, Vol. 19, No. 8, 1983, pp. 677-692.

19. Dems K., and Mroz Z., "Variational Approach by Means of Adjoint Systems to Structural Optimization and Sensitivity Analysis -II", International Journal of Solids and Structures, Vol. 20, No. 6, 1984, pp. 527-552.

20. Chun Y.W., and Haug E.J., "Two Dimensional Shape Optimal Design", International Journal for Numerical Methods in Engineering, Vol. 13, 1978, pp. 311-336.

21. Chun Y.W., and Haug E.J., "Shape Optimal Design of an Elastic Body of Revolution", Preprint No. 3516, ASCE Annual Meeting, Boston, April 1979.

22. Rousselet B., and Haug E.J., "Design Sensitivity Analysis in Structural Mechanics III: Shape Variation", Optimization of Distributed Parameter Structures (Ed. E.J. Haug and J. Cea) Sijthoff & Noordhoff, Alphen aan den Rijn, Netherlands, 1980.

23. Haug E.J., "A Gradient Projection Method for Structural Optimization", Optimization of Distributed Parameter Structures, (Ed. E.J. Haug and J. Cea) Sijthoff & Noordhoff, Alphen aan den Rijn, Netherlands, 1980.

24. Cea J., "Solution of a Model Problem by Variational Methods and Examples of Problems of Shape Optimal Design" Optimization of Distributed Parameter Structures, (Ed. E.J. Haug and J. Cea) Sijthoff & Noordhoff, Alphen aan den Rijn, Netherlands, 1980.

25. Cea J., "Definition of Boundaries for Shape Design", Optimization of Distributed Parameter Structures, (Ed. E.J. Haug and J. Cea) Sijthoff & Noordhoff, Alphen aan den Rijn, Netherlands, 1980.

26. Zolesio J.P., "The Material Derivative (or Speed) Method for Shape Optimization", Optimization of Distributed Parameter Structures (Ed. E.J. Haug and J. Cea) Sijthoff & Noordhoff, Alphen aan den Rijn, Netherlands, 1980.

27. Zolesio J.P., "Speed Method in Several Examples" Optimization of Distributed Parameter Structures, (Ed. E.J. Haug and J. Cea) Sijthoff & Noordhoff, Alphen aan den Rijn, Netherlands, 1980.

28. Rousselet B., "Implementation of Shape Optimal Design Algorithm", Optimization of Distributed Parameter Structures, (Ed. E.J. Haug and J. Cea), Sijthoff & Noordhoff, Alphen aan den Rijn, Netherlands, 1980.

29. Yoo Y.M., Haug E.J., and Choi K.K., "Shape Optimal Design of An Engine Connecting Rod", ASME Journal of Mechanisms, Transmissions and Automation in Design, Vol. 106, No.3, 1984, pp. 415-419.

30. Yoo Y.M., Haug E.J., and Choi K.K., "Shape Optimal Design of Elastic Structured Components", Technical Report No. 82-8, Center for Computer Aided Design, University of Iowa, Iowa City, IA, 1982.

31. Lam H.L., Choi K.K., and Haug E.J., "A Sparse Matrix Finite Element Technique for Iterative Structural Optimization", Computers and Structures, Vol. 16, No. 1-4, 1983, pp.289-295.

32. Hou J.W., and Benedict R.L., "Shape Optimal Design and Free Boundary Value Problems", Technical Report No. 83-9, Center for Computer Aided Design, The University of Iowa, Iowa City, May 1983.

33. Choi K.K., and Haug E.J., "Shape Design Sensitivity Analysis of Elastic Structures", Journal of Structural Mechanics, Vol.11 No. 2, 1983, pp. 231-269.

34. Choi K.K., "Shape Design Sensitivity of Displacement and Stress Constraint", Journal of Structural Mechanics, Vol. 13, No. 1 1985, pp. 27-41.

35. Haug E.J., Choi K.K., and Komkov K., Design Sensitivity Analysis of Structural System, 1986, Academic Press, Inc. New York.

36. Lee H.G., Choi K.K., and Haug E.J., "Shape Optimal Design of Built- up Structures", Technical Report No. 84-12, Center for Computer Aided Design, University of Iowa, Iowa City, IA.

37. Yang R.J., and Choi K.K., "Accuracy of Finite Element Based Design Sensitivity Analysis", Journal of Structural Mechanics, Vol. 13, No. 2, 1985, pp. 223-239.

38. Yang R.J., Choi K.K., and Haug E.J., " Numerical Considerations in Structural Component Shape Optimization", ASME Journal of Mechanics, Transmissions and Automation in Design, Vol. 107 No. 3, 1986, pp. 334-339.

39. Yang R.J., and Botkin M.E., " A Modular Approach for Three-Dimensional Shape Optimization of Structures", General Motor Research Labaratories, Research publication, GMR-5216. Warren, Michgan, March 11, 1986.

40. Choi K.K., and Seong H.G., "A Domain Method for Shape Design Sensitivity Analysis", Computer Methods in Applied Mechanics and Engineering, Vol. 57, No. 1, August 1986, pp. 1-15.

41. Choi K.K., and Seong H.G., "Boundary-Layer Approach to Shape Design Sensitivity Analysis", Journal of Structural Mechanics, To appear.

42. Choi K.K., Santos L.T., and Frederick M.C., "Implementation of Design Sensitivity Analysis with Existing Finite Element Codes", ASME Journal of Mechanics, Transmissions, and Automation in Design, 85-DET-77.

43. Dopker B, and Choi K.K., "Arch Design Sensitivity Analysis", Technical Report 86-5, Center for Computer Aided Design, University of Iowa, Iowa City, Iowa, 1986.

44. Haug E.J., "A Review of Distributed Parameter Structural Optimization Literature", Optimization of Distributed Parameter Structures, (Ed. E.J. Haug and J. Cea) Sijthoff & Noordhoff, Alphen aan den Rijn, Netherlands, 1980.

45. Haftka R.T., and Grandhi R.V., "Structural Shape Optimization-A Survey", Computer Methods in Applied Mechanics and Engineering, No. 57, 1986, pp. 91-106.

46. Sokolnikoff, I.S., Mathematical Theory of Elasticity, McGraw-Hill Book Co., New York, 1956.

47. Reinschmidt K.F., and Narayanan R., "The Optimum Shape of Cooling Towers", Commputers & Structures, Vol. 5, 1975, pp. 321-325.

48. Bhavikatti S.S., and Ramakrishnan C.V., "Optimum Shape Design of Pressure Vessel and Nozzle Junction", Nuclear Engineering and Design, No. 49, 1978, pp. 255-262.

49. Queau J.P., and Trompette P.H., "Two Dimensional Shape Optimal Design by Finite Element Methods", International Journal of Numerical Methods in Engineering, Vol.15, 1980, pp.1603-1612.

50. Tai T.C., Kidwell G.H.J., and Vanderplatts G.N., "Numerical Optimization of Circulation Control Airfoils", AIAA, Vol. 19, No. 2, 1982, pp. 145-150.

51. Barnhill R.E., and Boehm W., Surfaces in Computer Aided Geometric Design, North-Holland Publishing Comapny, Amsterdam, 1983.

52. Mortenson M.E., Geometric Modeling, John Wiley & Sons, New York, 1985.

53. Altuzarra T., Knopf-Lenoir C., Sayetat C., and Touzot G., "Interactive Optimum Design System", Proc. Tucson Symposium, Tucson, AZ, 1981.

54. Bezier P., "Mathematical and Practical Possibilities of UNISURF", in Computer-Aided Geometric Design, Barnhill R.E., Riesenfeld, eds., Academic, New York, 1974.

55. Newman W.M., and Sproull R.F., Principles of Interactive Computer Graphics, Second Edition, McGraw-Hill Inc., 1979.

56. Schoenberg I.J., On Spline Functions, with Supplement by Greville T.N.E., 'Inequalities' (Shisha O. editor), Academic Press (1967), pp. 255-291.

57. Cullen C.G., Matrices and Linear Transformation, Addison Wesley Publishing Company, Second Edition, London, 1972,

58. Zienkiewicz O.C., and Phillips D.V., "An Automatic Mesh Generation Scheme for Plane and Curved Surfaces by 'Isoparametric' Coordinates", International Journal for Numerical Methods in Engineering, Vol. 3, 1971, pp. 519-528.

59. Buell W.R., and Bush B.A., "Mesh Generation-A Survey", Transactions of the ASME, February 1973, pp.332-338.

60. Thacker W.C., "A Brief Review of Techniques for Generating Irregular Computational Grids", International Journal for Numerical Methods in Engineering, Vol.15, 1980, pp.1335-1341.

61. Haber R., Shephard M.S., Abel J.F., Gallagher R.H., and Greenberg D.P., "A General Two-Dimensional Graphical Finite Element Preprocessor Utilizing Discrete Transfinite Mappings", International Journal for Numerical Methods in Engineering, Vol. 17, 1981, pp. 1015-1044.

62. Thompson J.F., Warsi Z.U.A., and Mastin C.W., Review Article. "Boundary-Fitted Coordinate Systems for Numerical Solution of Partial Differential Equations - A Review", Journal of Computational Physics, Vol. 47, 1982, pp.1-108.

63. Cavendish J.C., Field D.A., and Frey W.H., "An Approach to Automatic Three-Dimensional Finite Element Mesh-Generation", International Journal for Numerical Methods in Engineering, Vol. 21, 1985, pp. 329-347.

64. Kikuchi N., Chung K.Y., Torigaki T., and Taylor J.E., "Adaptive Finite Element Methods for Shape Optimization of Linearly Elastic Structures", Computer Methods in Applied Mechanics and Engineering, No. 57, 1986, pp. 67-89.

65. Huggler A.H., and Weidmann E. , "Design Criteria of Total Hip Replacements Fixed with Bone Cement", in Advances in Artificial Hip and Knee Joint Technology, eds. Schaldah M., Hohmann D., Thull R., Hein F., Springer-Verlag, Berln, 1976,

66. Ugural A.C., and Fenster S.K., Advanced Strength and Applied Elasticity, Elsevier North Holland, 1981.

67. Choi K.K., and Twu S.L., Research Note, Center for Computer Aided Design, University of Iowa, Iowa City, IA, Sep. 1986.

68. United States Department of the Interior, Bureau of Reclamation, "Design of Arch Dams", Design Manual for Concrete Arch Dams, Denver, Colorado, 1977.

69. Vitiello E., "Shape Optimization Using Mathematical Programming and Modeling Techniques", in AGARD CP, Vol.123, 1973.

70. Rajan M.K.S., "Shell Theory Approach for Optimization of Arch Dam Shapes", Ph.D. Thesis, University of California, Berkeley, 1968.

71. Mohr G.A., "Design of Shell Shape using Finite Elements", Computers & Structures, Vol. 10, 1979.

72. Sharpe R., "The Optimum Design of Arch Dams", Institution of Civil Engineers, Paper 720 S, 1969.

73. Zienkiewicz O.C., The Finite Element Method, 3rd Edition, McGraw-Hill Book Company Ltd., London, 1977.

74. Hinton E., Rock T., and Zienkiewicz O.C., "A Note on Mass Lumping and Related Processes in the Finite Element Method", Earth Quake Engineering and Structural Dynamics, Vol.4, 1976, pp.245-249

75. Fried I., and Malkus D.S., "Finite Element Mass Matrix Lumping by Numerical Integration with No Convergence Rate Loss", International Journal of Solids Structures, Vol. 11, 1975 pp. 461-466.

76. Clough R.W., "Analysis of Structure Vibrations and Response", Recent Advances in Matrix Method of Structure Analysis and Design, (eds. R.H. Gallagher, Y. Yamada, J.T. Oden) First U.S.-Japan Seminar, Alabama Press, 1971, pp.25-45.

77. Kohnke P.C., ANSYS-Engineering Analysis System Theoretical Manual, Houston, 1983.

78. Vichnin H.H., and Batterman S.C., "Stress Analysis and Failure Prediction in the Proximal Femur Before and After Total Hip Replacement", Journal of Biomechanical Engineering, Vol.108 February 1986, pp.33-41.

79. Conventry M.B., "An Historic Perspective and the Present Status of Total Hip Arthroplasty", The Hip-Clinical studies and Basic Research, Proceeding of the 1st Western Pacific Area Conference on the Hip, Tokyo, Japan, October, 1983, Excerpta Medica, Amesterdam, New York, Oxford, 1984.

80. Barton J.R., "On the Treatment of Ankylosis by the Formation of Artificial Joints", North American Medical Journal, No.3, 1827, p. 279.

81. Smyth E.H.J., "The Mechanical Problem of the Artificial Hip", Journal of Bone and Joint Surgery, Vol.40-b, No. 4, 1958, pp. 778-798.

82. Brekelmans W.A.M., Poort H.W., and Slooff T.J.J.H., "A New Method to Analysis the Mechanical Behavior of Skeletal Parts", Acta Orthopaedics Scandinavia, Vol.43, 1972, pp. 301-317.

83. Huiskes R., and Chao E.Y.S., "A Survey of Finite Element Analysis in Orthopaedic Biomechanics: The First Decade", Journal of Biomechanics, Vol. 16, No.6, 1983, pp.385-409.

84. Gallagher R.H., Simon B.R., Johnson P.C., and Gross J.F., Finite Elements in Biomechanics, Wiley, 1982.

85. Crowningshield R.D., Brand R.A., Johnston R.C., and Milroy J.C., "The Effect of Femoral Stem Cross-Sectional Geometry on Cement Stresses in Total Hip Reconstruction", Clinical Orthopaedics, Vol. 146, 1980, pp. 71-77.

86. Sih G.C., Moyer E.T., and Berman A.T., "Analytical Modeling of Bone-Cement Interface and Failure Prediction", Engineering Fracture Mechanics, Vol. 14, No. 4, 1981, pp. 779-787.

87. Kwak B.M., Lim O.K., Kim Y.Y., and Rim K., "An Investigation of the Effect of Cement Thickness on an Implant by Finite Element Stress Analysis", International Orthopaedics, 1979, pp. 315-319.

88. Crowninshield R.D., Brand R.A., Johnston R.C., and Pedersen D.R., "An Analysis of Collar Function and the Use of Titanium in Feromal Prostheses", Clinical Orthopaedics, July-August 1981, Vol. 158., pp. 270-277.

89. Crowningshield R.D., and Wilson M.A., "A Design Analysis of Bone Cements used in Total Hip Reconstruction", A Report to Howmedica, Inc., Biomechanics Laboratory, University of Iowa, Iowa City, November 1982.

90. Sih G.C., Matic P., and Berman A.T., "Failure Prediction of the Total Hip Prothesis System", Journal of Biomechanics, Vol. 14 No.12, 1981, pp. 833-841.

91. Sih G.C., and MacDonald B., "Fracture Mechanics Applied to Engineering Problems-Strain Energy Density Fracture Criterion", Engineering Fracture Mechanics, Vol. 6, 1974, pp. 361-386.

92. Yang R.J., Choi K.K., Crowninshield R.D., and Brand R.A., "Design Sensitivity Analysis: A New Method for Implant Design and a Comparison with Parametric Finite Element Analysis", Journal of Biomechanics, Vol. 17, No. 11, 1984, pp. 849-854.

93. Crowningshield R.D., Brand R.A., Johnston R.C., and Milroy J.C., "An Analysis of Femoral Component Stem Design in Total Hip Arthroplasty", The Journal of Bone and Joint Surgery, Vol. 62-A, No. 1, January 1980, pp. 68-78.

94. Lindahl O., and Lindgren G.H., "Cortical Bone in Man-II. Variation in Tensile Strength with Age and Sex", Acta Orthopaedics Scandinavia, Vol. 38, 1967, pp. 141-147.

95. Lindahl O., and Lindgren G.H., "Cortical Bone in Man-III. Variation in Compressive Strength with Age and Sex", Acta Orthopaedics Scandinavia, Vol.39, 1968, pp. 129-135.

96. Tsai S.W., and Wu E.M., "A General Theory of Strength for Anisotropic Materials", Journal of Composite Materials, Vol. 5, pp. 58-80, 1971.

97. Crowningshield R.D., Johnston R.C., Andrews J.G., and Brand R.A., "A Biomechanical Investigation of the Human Hip", Journal of Biomechanics, Vol. 11, 1978, pp. 75-85.

98. Johnston R.C., Brand R.A., and Crowningshield R.D., "Reconstruction of the Hip: A Mathematical Approach to Determine Optimum Geometric Relationships", The Journal of Bone and Joint Surgery, Vol. 61-A, No. 5, July 1979, pp. 639-652. pp. 361-373.

99. Choi K.K., Haug E.J., Hou J.W., and Sohoni V.N., " Pshenichy's Linearization Method for Mechanical System Optimization", Transactions of the ASME, Journal of Mechanical Design, 82-det-98, 1982.

100. Pshenichny B.N., and Danilin Y.M., Numerical Methods in Extremal Problems, MIR Publishers, Moscow, 1978.

101. Pshenichny B.N., "Algorithms for the General Problem of Mathematical Programming", Kiberneika, No.5, 1970, pp.120-125.

102. Pironneau O., Optimal Shape Design for Elliptic Systems, Springer-Verlag, New York, 1984.